ALMA MATER STUDIORUM

UNIVERSITÀ DI BOLOGNA

DEIS – Department of Electronics, Computer Science, and Systems

Computational Analyses on the Structure-Function Relation in Ion Channels

Simone Furini

Thesis submitted for the degree of Ph.D. in Bioengineering (ING-INF/06)

Supervisor

Prof. Guido Avanzolini

PhD Director

Prof. Angelo Cappello

Co-Supervisor

Prof. Silvio Cavalcanti

Reviewers

Prof. Gianni Gnudi

Prof. Carmen Domene

Prof. Malgorzata Kotulska

Summary

Ion channels are protein molecules, embedded in the lipid bilayer of the cell membranes. They act as powerful sensing elements switching chemical-physical stimuli into ion-fluxes. At a glance, ion channels are water-filled pores, which can open and close in response to different stimuli (*gating*), and one once open select the permeating ion species (*selectivity*). They play a crucial role in several physiological functions, like nerve transmission, muscular contraction, and secretion. Besides, ion channels can be used in technological applications for different purpose (sensing of organic molecules, DNA sequencing). As a result, there is remarkable interest in understanding the molecular determinants of the channel functioning.

Nowadays, both the functional and the structural characteristics of ion channels can be experimentally solved. The purpose of this thesis was to investigate the structure-function relation in ion channels, by computational techniques. Most of the analyses focused on the mechanisms of ion conduction, and the numerical methodologies to compute the channel conductance. The standard techniques for atomistic simulation of complex molecular systems (Molecular Dynamics) cannot be routinely used to calculate ion fluxes in membrane channels, because of the high computational resources needed. The main step forward of the PhD research activity was the development of a computational algorithm for the calculation of ion fluxes in protein channels. The algorithm - based on the electrodiffusion theory - is computational inexpensive, and was used for an extensive analysis on the molecular determinants of the channel conductance.

The first record of ion-fluxes through a single protein channel dates back to 1976, and since then measuring the single channel conductance has become a standard experimental procedure. Chapter 1 introduces ion channels, and the experimental techniques used to measure the channel currents. The abundance of functional data (channel currents) does not match with an equal abundance of structural data. The bacterial potassium channel KcsA was the first selective ion channels to be experimentally solved (1998), and after KcsA the structures of four different potassium channels were revealed. These experimental data inspired a new era in ion channel modeling. Once the atomic structures of channels are known, it is possible to define mathematical models based on physical descriptions of the molecular systems. These physically based models can provide an atomic description of ion channel functioning, and predict the effect of structural changes. Chapter 2 introduces the computation methods used throughout the thesis to model ion channels functioning at the atomic level.

In Chapter 3 and Chapter 4 the ion conduction through potassium channels is analyzed, by an approach based on the Poisson-Nernst-Planck electrodiffusion theory. In the electrodiffusion theory ion conduction is modeled by the drift-diffusion equations, thus describing the ion distributions by continuum functions. The numerical solver of the Poisson-Nernst-Planck equations was tested in the KcsA potassium channel (Chapter 3), and then used to analyze how the atomic structure of the intracellular vestibule of potassium channels affects the conductance (Chapter 4). As a major result, a correlation between the channel conductance and the potassium concentration in the intracellular vestibule emerged. The atomic structure of the channel modulates the potassium concentration in the vestibule, thus its conductance. This mechanism explains the phenotype of the BK potassium channels, a sub-family of potassium channels with high single channel conductance.

The functional role of the intracellular vestibule is also the subject of Chapter 5, where the affinity of the potassium channels hEag1 (involved in tumour-cell proliferation) and hErg (important in the cardiac cycle) for several pharmaceutical drugs was compared. Both experimental measurements and molecular modeling were used in order to identify differences in the blocking mechanism of the two channels, which could be exploited in the synthesis of selective blockers. The experimental data pointed out the different role of residue mutations in the blockage of hEag1 and hErg, and the molecular modeling provided a possible explanation based on different binding sites in the intracellular vestibule.

Modeling ion channels at the molecular levels relates the functioning of a channel to its atomic structure (Chapters 3-5), and can also be useful to predict the structure of ion channels (Chapter 6-7). In Chapter 6 the structure of the KcsA potassium channel depleted from potassium ions is analyzed by molecular dynamics simulations. Recently, a surprisingly high osmotic permeability of the KcsA channel was experimentally measured. All the available crystallographic structure of KcsA refers to a channel occupied by potassium ions. To conduct water molecules potassium ions must be expelled from KcsA. The structure of the potassium-depleted KcsA channel and the mechanism of water permeation are still unknown, and have been investigated by numerical simulations. Molecular dynamics of KcsA identified a possible atomic structure of the potassium-depleted KcsA channel, and a mechanism for water permeation. The depletion from potassium ions is an extreme situation for potassium channels, unlikely in physiological conditions. However, the simulation of such an extreme condition could help to identify the structural conformations, so the functional states, accessible to potassium ion channels.

The last chapter of the thesis deals with the atomic structure of the α-Hemolysin channel. α-Hemolysin is the major determinant of the *Staphylococcus Aureus* toxicity, and is also the prototype channel for a possible usage in technological applications. The atomic structure of α-Hemolysin was revealed by X-Ray crystallography, but several experimental evidences suggest the presence of an alternative atomic structure. This alternative structure was predicted, combining experimental measurements of single channel currents and numerical simulations.

This thesis is organized in two parts, in the first part an overview on ion channels and on the numerical methods adopted throughout the thesis is provided, while the second part describes the research projects tackled in the course of the PhD programme. The aim of the research activity was to relate the functional characteristics of ion channels to their atomic structure. In presenting the different research projects, the role of numerical simulations to analyze the structure-function relation in ion channels is highlighted.

INDEX

PART I

Introduction

Chapter 1

Structure and Function of Ion Channels

A specialized class of membrane proteins, named ion channels, governs the ion fluxes through the cell membranes. These protein channels can open and close in response to chemical-physical stimuli, and once open select the most permeating ion species. As a consequence of these characteristics ion channels are powerful sensors, which play a crucial role in several physiological functions (nerve transmission, muscular contraction, secretion), and may also be exploited in technological applications This chapter briefly introduces ion channels, and the experimental techniques used to measure the channel currents.

1.1 Ionic Fluxes Through the Cell Membrane

Every cell exists as a separate entity thanks to a lipid envelope, named cell membrane (Alberts, 2008). This lipid membrane separates the inside of the cell (cytoplasm) from the extracellular compartment. It retains the vital components of the cells, and at the same time it prevents the trafficking of hydrophilic solutes. The cell membrane includes specific structures to move molecules in and out from the cytoplasm. Most of these structures are protein molecules embedded in the lipid bilayer of the membrane (integral membrane protein). Transporters and ion channels are the membrane proteins responsible for ion trafficking.

Transporters move ions across the membrane, regardless of the direction of the electrochemical gradients (Friedlander, 1993). As an example, the N_a^+/K^+ pump moves three sodium ions outward and two potassium ions inward per cycle, hydrolyzing at the same time an ATP molecule (Glynn, 1985). Since ion movements through transporters are not coupled to the electrochemical gradients, the transport mechanism requires energy, which in the case of the N_a^+/K^+ pump is supplied by the hydrolysis of ATP. A bunch of transport proteins have been identified since the late fifties, moving different ion species and governed by different physical stimuli (N_a^+/K^+ pump; Ca^{2+} pump; Na^+/Ca^{2+} exchanger; Cl^-/HCO_3^- exchanger). As a result of the transporter' activity the ionic concentrations in the intracellular and extracellular compartments are different (Table 1-1).

The differences in ionic concentrations, thus the electrochemical gradients through the cell membrane, provide the driving forces for ion movements across ion channels (Hille, 2001). At a first glance, an ion channel is a water-filled pore, which allows ion fluxes in the direction of the electrochemical gradients. However, channels are not simple pores. They can open and close in response to chemical-physical stimuli (gating), and they have the important propriety of selective permeability. Channels are usually named

after the most permeable ion species (i.e. potassium channels, sodium channels, calcium channels, and chloride channels), or the stimulus governing the gating (i.e. voltage-gated, ligand-gated, and mechanosensitive).

	$[Na^+]$ mM	$[K^+]$ mM	$[Ca^{2+}]$ mM	$[Cl^-]$ mM
Intracellular	12	155	~0	4.2
Extracellular	145	4	1.5	123

Table 1-1 Ionic concentrations in the cytoplasm and in the extracellular compartment (Hille, 2001).

The ability to open and close and the selective permeability, make ion channels powerful sensors that play crucial roles in several physiological functions (cell excitability, secretion). The first evidence of the physiological role of ion channels dates back to the Hodgkin and Huxley studies on nervous transmission (Hodgkin, 1952). The information in the nervous system is coded by electrical pulses (action potentials), which move along the nerve axon. The action potential propagates thanks to voltage gated sodium and potassium channels. When an action potential reaches the nerve terminal, it evokes the release of neurotransmitters, which in turn cause other channels in adjacent cells to open. The role of ion channels in nerve transmission is a classical example, used to highlight the physiological functions of ion channels. In the most general terms, ion channels are the physical substrates of the sensory system of the cell.

1.2 Potassium Channels

A family of selective ion channels exists for each ion of the Ringer's solution (Na^+, K^+, Ca^{2+}, Cl^-). Among these four families of ion channels, the channels selectively permeable to potassium ions are the ones showing the

greatest variability (Hille, 2001). Potassium channels differ mainly in the gating characteristics, while the selectivity function is remarkably conserved in the whole family. The permeability sequence is $Tl^+ > K^+ > Rb^+ > NH_4^+$, and the permeability to Na^+ is usually too low to be measured. The conservation of the selectivity function suggests a structural conservation in the pore region of potassium channels. The analysis of the aminoacid sequences in different potassium channels supports this hypothesis. The aminoacid sequence TVGYG is widely conserved among potassium channels, and thus it was suggested as the protein segment forming the pore region responsible for the selectivity function (MacKinnon, 1998).

The hypothesis of a conserved pore has been confirmed by the crystallographic structures of several potassium channels. The first potassium channel to be experimentally solved was the KcsA potassium channel from the bacterium *Streptomyces Lividans* (Doyle, 1998). This channel is made of four subunits, symmetrically arranged around the channel axis (Figure 1-1). Each subunit consists of three α-helix structures - the outer helix, the pore helix and the inner helix – placed as shown in Figure 1-2. Different names are used in the literature for the outer helixes and the inner helixes, depending on the channel sub-family (M1,M2 in ligand gated channels; S5, S6 in voltage-gated channels). The conduction pathway on the extracellular side is lined by the carbonyl oxygens of the aminoacid sequence TVGYG; one sequence from each subunit (Figure 1-2). This region, named selectivity filter (SF), is 16 Å long with a mean radius of 1.4 Å. The selectivity filter has five binding sites for potassium ions, named S0 (extracellular side) to S4 (intracellular side). Below the selectivity filter the channel opens into a wide chamber, connected to the intracellular compartment by a hydrophobic pore. Both the chamber and the hydrophobic pore are lined by the four inner helices.

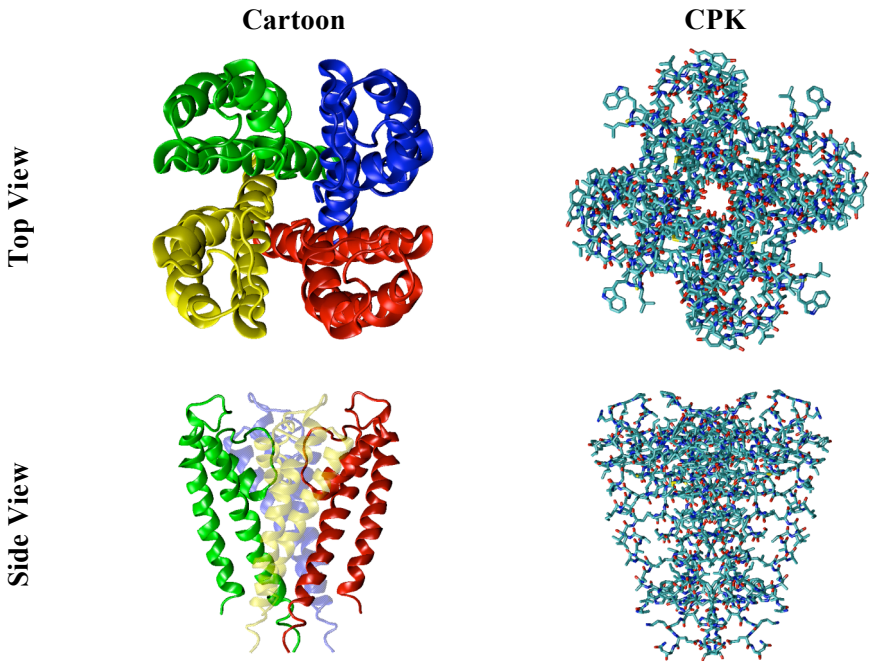

Figure 1-1 KcsA channel
Extracellular and side views of the KcsA channel, in the cartoon and CPK modality. In the cartoon modality different colors are used for the four subunits. Molecular representations were produced by the software VMD (Humphrey, 1996).

The two hallmarks of potassium channels are: i) the rate of conduction (10^8 ions/s) close to the diffusion limit and ii) the high selectivity (K^+ is at least 10^4 times more permeant than Na^+) (Hille, 2001). High fluxes need conduction mechanisms without energetic barriers, while selectivity needs a close interaction between ions and channel. Knowledge of the KcsA atomic structure has disclosed the mechanisms underlying these complex functionalities. The selectivity of the binding sites S0-S4 for K^+ over Na^+ was proved by molecular dynamics simulations (see section 2.1 for an introduction to molecular dynamics) (Allen, 1999; Aqvist, 2000). In physiological conditions the SF is occupied by two potassium ions on average, separated by a water molecule (Berneche, 2003; Morais-Cabral, 2001). The configuration with ions in S1 and S3 can rapidly switch to that

with ions in S2 and S4 because of the low energetic barrier, ~2Kcal/mol (Berneche, 2001). Conduction takes place when a third ion enters the SF from one side, causing the concerted motion of all the ions in the filter, and finally pushing an ion out from the opposite side. In agreement with the high throughput rate of potassium channels, no significant energetic barrier hampers any of the steps of the transport mechanism of potassium. To explain the lower conductance of rubidium, an ion slightly bigger than potassium, it is enough to introduce an energetic barrier between the configurations with two ions in the SF (S1-S3 and S2-S4) (Morais-Cabral, 2001).

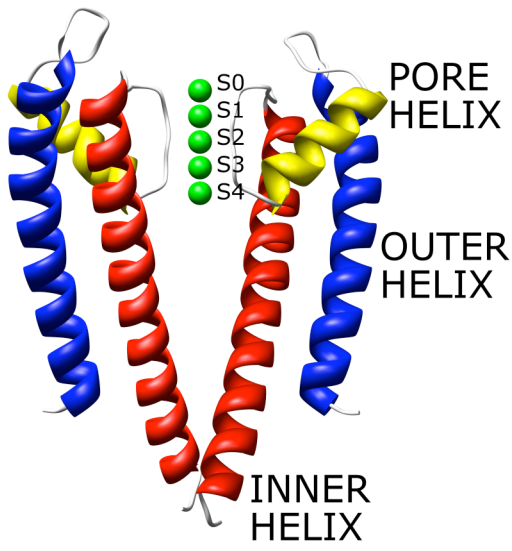

Figure 1-2 KcsA channel
Side view of the KcsA channel. For clarity, only two subunits are shown. Five potassium ions are included in the selectivity filter at the binding sites S0-S4, numbering starts from the top (extracellular side).

A pore structure similar to KcsA has been observed in the potassium channels MthK (Jiang, 2002a), KvAP (Jiang, 2003), Kv1.2 (Long, 2005) and KirBac1.1 (Kuo, 2003). MthK is a Ca^{2+} gated potassium channel (from the *Methanobacterium Thermoautotrophicum*); KvAP (from the bacterium *Aeropyrum Pernix*) and Kv1.2 (from *Rattus Norvegicus*) are voltage-gated channels; while KirBac1.1 (from the bacterium *Burkholderia*

Pseudomalleiare) is an inward rectifier channel, whose gating stimuli are still not well understood. The conservation of the pore structure in these distantly related potassium channels supports the hypothesis of a common architecture of the pore in the whole potassium channel family. The accepted view is that four "building-blocks" – each made of an inner-helix, an outer-helix, and a pore helix – arrange around the central pore, forming the permeation pathway of potassium channels. Usually each block is a separate protein chain. However, some potassium channels (named K_{2P}) are made of only two protein chains, each providing two "building blocks" to the pore region.

The KcsA channel is an extremely simple potassium channel, with just two transmembrane segments per subunit (the outer helix and the inner helix). The voltage-gated channels have six transmembrane segments per subunit. The four additional transmembrane segments are responsible for the voltage sensing, thanks to the presence of electrically charged residues. Other potassium channels have large cytoplasmatic domains (like MthK), which control the gating or the conduction characteristics of the channel. Thanks to this structural heterogeneity, potassium channels show different functional behaviours. The existence of a bunch of potassium channels with different functional characteristics is crucial in biological processes. Potassium channels are involved in a wide range of physiological functions. They regulate the duration of the action potential in the cardiac cycle, and they also contribute to reabsorption in the kidneys. The fine balances of ionic currents required by these complex biological functions would not be possible without the diversity of the potassium channel family.

Most of the computation analyses presented in this thesis deal with the pore region of potassium channels. This is where the conduction processes take place, and where several pharmaceutical blockers interact with potassium channels. Despite the general architecture of the pore region, minor differences in its atomic structure influence the conduction and the

pharmacological characteristics of potassium channels. Understanding how the atomic structure of the pore is related to the functionality of potassium channels is the subject of Chapter 3, Chapter 4 and Chapter 5.

1.3 Channels as Molecular Sensors

In section 1.1 the important role of ion channels in the sensory system has been highlighted. Channels respond to physical stimuli (i.e. membrane voltage, mechanical stress and neurotransmitters) by changing their conductance. Since measuring the single channel currents is relative easy (see section 1.4), ion channels can be used as transducers, capable of converting some chemical-physical stimulus into an electrical current.

Several characteristics make the usage of ion channels in technological applications a particular attractive opportunity. Ion channels show an amazing variability in the stimuli governing their conductance, which implies an equivalent variability in the possible usage of ion channels as sensing elements. Then, the sensitivity of channels to stimuli is usually high, and the response fast. Ion channels sensible to analytes in nanomolar concentrations are not uncommon, like responses in the microsecond time scale. Moreover, the gating of ion channels is a reversible processes, which allows the detection of more than one event by the same channel. As a final remark, an ion channel can usually responds to more than one stimulus. The cross-reactivity of ion channels can be exploited in order to use a single sensor for several analytes.

The possible usage of ion channels as sensing elements has already been demonstrated in several applications. Channels have been used to detect anions or cations (Braha, 2000), small organic molecules (Gu, 1999), and DNA or RNA (Kasianowicz, 1996). The nucleotide sequence of DNA molecules has also been analyzed by ion channels (Howorka, 2001). Genetic engineering and site-specific chemical modification techniques can be used

to functionalize ion channels, in order to promote the detection of specific molecules. The availability of these techniques is a further motivation for the usage of ion channels in technological applications.

Up to now, the development of ion channel sensors has been slowed down by the fragility of the planar lipid bilayer, where the channels have to be embedded. Several techniques have been tested to overcome the problem, like pores in the nanometre scale (McGeoch, 2000), solid-supported bilayers (Sackmann, 2000), and more recently protected planar bilayers (Kang, 2007). Nowadays, the protected lipid bilayers technique is the most promising methodology to produce ion channel sensors. Using this technique, Kang et al (Kang, 2007) have developed a chip containing a single ion channel and operative for several weeks, in 2007.

In the context of a possible usage of ion channels as sensing elements, Chapter 7 describes a research project regarding the atomic structure of α-Hemolysin, the prototype channel for technological applications.

1.4 Experimental Techniques for Ion Channel Analyses

Since the introduction of the patch clamp technique (Hamill, 1981), measuring the ionic currents through a single protein channel has become a routine experiment. Moreover, thanks to improvements in molecular biology, ion channels can now be expressed in heterologous system, and eventually genetically mutated. The introduction of mutation in the aminoacid sequence of an ion channel allows studying how an alteration in the channel structure affects the functionality. These studies are particularly useful to analyze the structure-function relation in channels, which is the final goal of this thesis. Most of the experimental data refereed throughout the thesis are single channel currents, thus the experimental techniques used to perform these measurements are briefly described in this introductory

chapter. The sub-section 1.4.1 describes the patch clamp technique, while in the sub-section 1.4.2 a different technique for current measurements in artificial lipid bilayer is described.

Opposed to the feast of functional data, a famine of structural data is available about ion channels. Nowadays, around 150 atomic structures of membrane proteins have been experimentally solved (White). X-Ray crystallography and Nuclear Magnetic Resonance are the experimental techniques used to obtain these data. All the structural data used in this thesis are from X-Ray crystallography. This technique provides a static structure of the protein in a crystal environment, with atomic resolution. Structural data are required for numerical simulations of ion channels at the atomic level, and at the same time numerical simulations are important to relate the static picture offered by X-Ray crystallography to the dynamic functioning of ion channels.

1.4.1 Patch Clamp

Most of what we know today about ion channel functioning comes from voltage-clamp measurements of channel currents. In a voltage clamp experiment the electric potential through the cell membrane – or through a membrane patch – is controlled to a reference value (V_m), and the current flowing through the membrane is at the same time measured. Figure 1-3 shows a simplified scheme of a recording system for voltage clamp experiments (Sakmann, 1995).

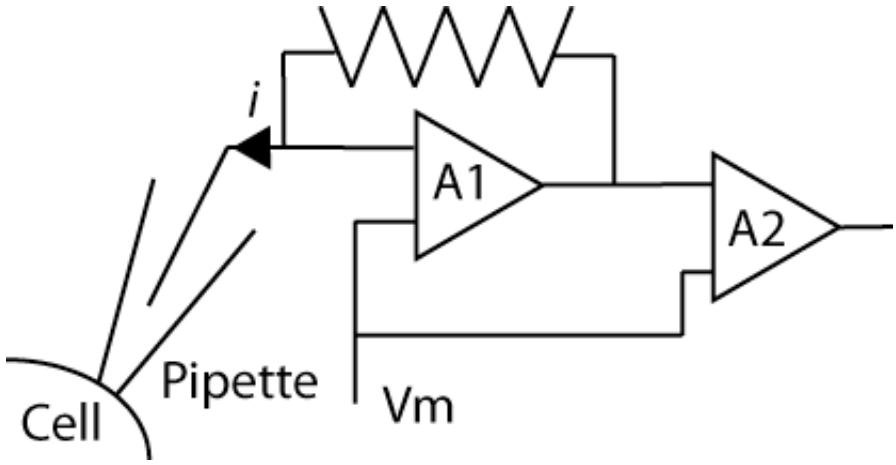

Figure 1-3 Voltage Clamp Amplifier

The first operational amplifier (*A1*) forces the pipette potential to the reference value, supplying the appropriate current (*i*) through the feedback resistance. The second amplifier (*A2*) subtracts the reference potential from the *A1* output, in order to have an output signal proportional to the current *i*. To perform a patch clamp experiment the recording pipette is first pushed against the cell membrane. By appropriate experimental expedients (clean surfaces, negative pressure in the pipette), a gigaohm resistance is created between the lipid layer of the membrane and the pipette (gigaseal). This gigaseal is crucial for high-quality recordings. In case of low resistance, part of the membrane current would not flow through the pipette, but directly in the bathing solution. Moreover, a low seal resistance would produce a high noise in the recording system because of thermal motions, which would prevent the measurement of single channel currents. Once realized a high quality gigaseal, three different experimental conditions are possible, named whole cell, inside-out, and outside-out.

In the whole-cell modality the current through the entire cell membrane is measured, while in inside-out and outside-out only the current through a limited patch of the membrane is measured. Inside-out and outside-out differ in the orientation of the cytoplasmatic side (inside) of the membrane with

respect to the pipette: outside in inside-out; inside in outside-out. Throughout the thesis patch clamp experiments in the three experimental configurations will be refereed.

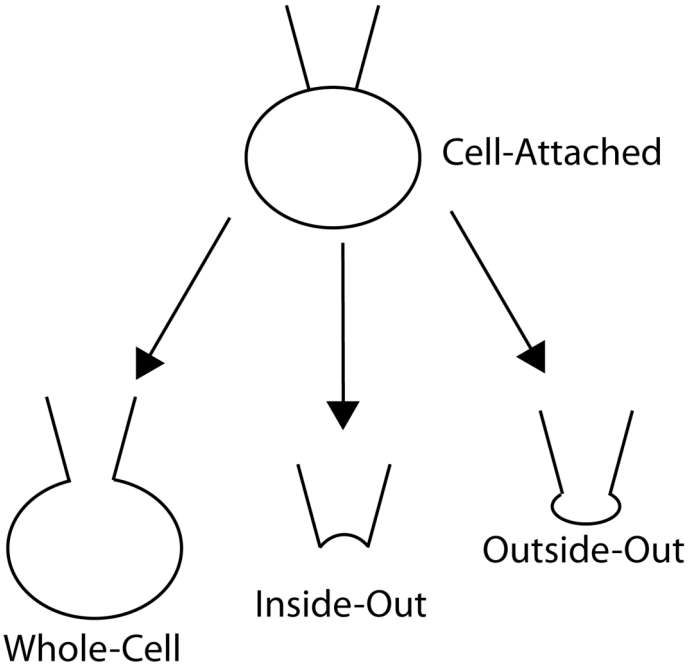

Figure 1-4 Patch Clamp Modes

1.4.2 Planar Lipid Bilayer

In the patch clamp approach channels inserted in the cell membrane are used for current recordings. An alternative approach is to measure the ion currents through protein channels embedded in an "artificial" planar lipid bilayer. A simple technique to create a lipid bilayer is to paint a hole trough a plastic material – separating two water compartments – with lipid molecules (Mueller, 1962). Because of their amphipathic nature lipid molecules will auto-assemble in a bilayer. Afterwards, ion channels can be embedded in the lipid bilayer by fusion of lipid vesicles containing the channels, or by direct insertion of water-soluble channels (Morera, 2007). A great advantage of the

recordings in planar lipid bilayers is the possibility to study ion channels not accessible by the patch clamp technique. Moreover, the easily accessible water compartments simplify the control of the water-solutions at the two sides of the channels. As a counterpart, the mechanical instability of the bilayer introduces a higher noise in the recording system. The planar lipid bilayer technique was used in this thesis to measure ion currents through the α-Hemolysin channel (Chapter 7).

Chapter 2

Computational Techniques for Structure-Function Analyses

Numerical simulations are a powerful tool to investigate the structure-function relation in molecular systems. At the atomic level, the behaviour of a system is described by Quantum Mechanics. Quantum mechanics explicitly represents electrons, thus a large number of particles are included in the mathematical model, and simulations are time consuming. Many of the problem that we would like to tackle in molecular biology, are too large to be considered by quantum mechanical calculations. Molecular Dynamics (MD) techniques explicitly represent just the nuclear coordinates, and offer a reliable alternative for the simulation of complex molecular systems in the nanosecond time scale. Biological relevant processes are usually slower - millisecond time scale – hence even MD is too computational demanding, and simplified mathematical models are require. This chapter introduces the MD approach, and the simplified methodologies used in the thesis to analyze the structure-function relation in ion channels.

2.1 Molecular Dynamics

Molecular dynamics (MD) simulations are widely used to analyze complex molecular systems - like proteins - at the atomic level. In MD simulations the molecular system is described by N classical particles. Each particle represents one or more atoms of the system, and evolves according to the Newton's equation of motion:

$$\frac{d\bar{p}}{dt} = \bar{F} \qquad \textbf{Equation 2-1}$$

Where $\bar{p}$ is the array of the momenta of the N particles in the molecular system ($\bar{p} = [p_x^1, p_y^1, p_z^1, ..., p_x^N, p_y^N, p_z^N]$), and $\bar{F}$ is the array of the forces. Forces are valued by the gradient of a potential energy function ($V(\bar{r})$, $\bar{r}$ being the array of the particle positions):

$$\bar{F} = -\nabla V(\bar{r}) \qquad \textbf{Equation 2-2}$$

The potential energy $V(\bar{r})$ is a crucial element in MD simulations, and a brief discussion on its functional form is given in section 2.1.1. Thanks to the simplified mathematical model of Equation 2-1 and Equation 2-2, complex molecular systems (hundreds of thousands of atoms) can be simulated by the MD approach. An important parameter in the numerical algorithm used to integrate the equation of motion (Hockney, 1970; Verlet, 1967) is the integration time step, Δt. A too short time step would slow down the exploration of the configurational space, while a too long time step would cause instability in the integration algorithm. To avoid instability, the time step must be shorter than the period of the fastest motion in the system. In molecular systems, the fastest motions are the oscillations of hydrogen

atoms, having a period of ~10fs. As a consequence, the time-step is restricted to the femtosecond time scale. This short time-step limits the time-scale accessible to molecular dynamics simulations, as further discussed in section 2.4.

2.1.1 Force Fields

In MD simulations the forces on each atom are computed by means of a potential energy function (Equation 2-2). The exact form of the potential energy changes according to the adopted force field, but a common expression will include terms associated with the deviation of bonds and angles from their equilibrium values, and terms modeling the interactions between non-bonded particles. The energetic penalties due to deviations of bonds and angles from their equilibrium values are usually modelled by harmonic potentials, while Lennard-Jones potentials are used to model the van der Waals interactions. Equation 2-3 shows a simple functional form of a force field:

$$V(\bar{r}) = \sum_{bonds} k_b (d - d_0)^2 + \sum_{angles} k_a (\theta - \theta_0)^2 + \\ + \sum_{torsions} \frac{V_t}{2}\left(1 + \cos\left(n_t \omega - \gamma_t\right)\right) + \\ + \sum_{i=1}^{N} \sum_{j=i+1}^{N} \left[\frac{A_{ij}}{d_{ij}^6} - \frac{B_{ij}}{d_{ij}^{12}} + \frac{q_i q_j}{4\pi\varepsilon_0 d_{ij}} \right] \qquad \textbf{Equation 2-3}$$

The first term models the interaction between bonded particles, by harmonic potentials (d is the bond length). The elastic constant (k_b) and the equilibrium bond length (d_0) are defined according to the atomic species involved in the bond. A harmonic potential is also used to model the deviation of bond angles from their equilibrium values (θ_0), while a periodic

potential models the potential energy related to torsion angles. The last two terms of Equation 2-3 describe the potential energy due to non-bonded interactions, i.e. van der Waals and electrostatic interactions (A_{ij} and B_{ij} are the parameters of the Lennard-Jones potential between particle i and particle j; q_i and q_j are the partial atomic charges; d_{ij} is the distance between particle i and particle j; and ε_0 is the vacuum permittivity).

The usage of simplified functions, like Equation 2-3, to define the potential energy of the molecular system is of course an approximation. Actually, the definition of a potential energy as a function of the nuclear coordinates only is itself an approximation (Born-Oppenheimer approximation). In spite of this simple scheme, MD simulations properly reproduce a wide spectrum of experimental data. These successes are the main arguments in support of the MD approach.

2.1.2 Molecular Dynamics in the NPT Ensemble

Molecular dynamics are Newtonian dynamics of N interacting particles. In this simple scheme, the number of particles, the energy and the volume of the molecular system do not change along the simulation (at least in principle, to guarantee the energy conservation along the numerical integration of the equation of motions is not a trivial problem). The microscopic configuration of the molecular system – described by positions and momenta, $[\bar{r}, \bar{p}]$ – will evolve among the possible configurations satisfying these constrictions (constant volume, energy and number of particles). This set of microscopic configurations is denoted as microcanonical ensemble, or NVT ensemble. This ensemble does not properly mimic the experimental conditions we are usually interested in. The variables controlled in a common experimental environment are the temperature and the pressure, not the volume and the energy. Thus, it would

be preferable to control the same variables in MD simulations. The set of microscopic configuration with constant number of particles, temperature and pressure is usually denoted as NPT.

Different schemes have been developed to control the temperature and the pressure in MD simulations. In the remaining part of this section, the coupling to external baths is described as an example, in order to introduce the problematic of pressure and temperature control in MD simulations. Most of the simulations presented in the second part of the thesis were performed at constant pressure and temperature.

The temperature of a molecular system is related to its average kinetic energy by:

$$T = \frac{2}{3Nk} \sum_{i=1}^{N} \frac{p_i^2}{2m_i}$$ **Equation 2-4**

Where k is the Boltzmann constant, p_i is the particle momentum, and m_i is the particle mass. According to Equation 2-4, the temperature of a molecular system can be controlled by controlling the particle velocities. A simple scheme to control the velocities is to couple the molecular system to a temperature bath (Berendsen, 1984), by the equation:

$$\frac{dT}{dt} = \frac{T_{bath} - T}{\tau_{bath}}$$ **Equation 2-5**

Where T_{bath} is the temperature of the bath, and τ_{bath} is the time constant of the coupling between the bath and the molecular system. As a consequence of Equation 2-5, in a time-step Δt the change in the system temperature is:

$$\Delta T = \frac{\Delta t}{\tau_{bath}}\left(T_{bath} - T\right)$$ **Equation 2-6**

This temperature change corresponds to a scaling of the velocities by a factor λ_T:

$$\lambda_T = \sqrt{1 + \frac{\Delta t}{\tau_{bath}}\left(\frac{T_{bath}}{T} - 1\right)}$$ **Equation 2-7**

When the coupling to an external bath is used to control the temperature, the equations of motion are solved in the usual way. Then after a time step Δt, the temperature is calculated by Equation 2-4. This value of the temperature is used in Equation 2-7 to get λ_T, which is then used to update the particle velocities (v_i) according to:

$$v_i = \lambda_T v_i$$ **Equation 2-8**

A similar scheme can be used to control the pressure value. Instead of coupling to a temperature bath, the molecular system will be coupled to a pressure bath by an equation analogous to Equation 2-5. The pressure (P) in a molecular system is related to the volume (V) by the isothermal compressibility, K_V:

$$K_V = -\frac{1}{V}\left(\frac{\partial V}{\partial P}\right)_T$$ **Equation 2-9**

Thus, to produce a pressure change ΔP in a time-step Δt the volume must be scaled by the factor:

$$\lambda_P = 1 + \frac{k\Delta T}{\tau_{pressurebath}}\left(P_{bath} - P\right) \qquad \textbf{Equation 2-10}$$

Where P_{bath} is the target pressure, and $\tau_{pressurebath}$ is the coupling time constant between the molecular system and the pressure bath.

2.2 Free Energy Calculations

According to the second law of thermodynamic, a system in the microcanonical ensemble (constant volume, energy, and number of particles) evolves towards states with maximum entropy (S). An equivalent statement of the second law is that a system in the canonical ensemble (constant volume, temperature and number of particles) evolves towards states with minimum Helmholtz free energy ($F = E - TS$, E is the energy of the system, T is the temperature); and a system in the isothermal-isobaric ensemble (constant pressure, temperature and number of particles) evolves towards states with minimum Gibbs free energy ($G = F + PV$, P is the pressure, and V is the volume) (Chandler, 1987). It follows that entropy and free energies are among the most important variables to be determined in thermodynamic systems, since they provide information about the spontaneous evolution of the system.

Unfortunately, these thermodynamic variables are at the same time the most complicated to calculate in numerical simulations. The difficulties in determining the thermodynamic variables S, F, and G are due to difficulties in determining the dimensionality of a thermodynamic system, i.e. the number of accessible microscopic states. Indeed, the entropy is defined by:

$$S = k \ln \Omega \qquad \textbf{Equation 2-11}$$

Where Ω is the number of possible microstates corresponding to the observed thermodynamic macrostate, and k is the Boltzmann constant. Numerical simulations of a molecular system tend to explore restricted regions of the configurational space, which cause a poor estimation on the number of accessible microstates. Numerous computational techniques have been developed in order to improve the estimation of the free energies (Chipot, 2007). In this thesis the umbrella sampling approach (Torrie, 1974), described in the next section, was used.

2.2.1 Umbrella Sampling

In the MD approach the configuration of the molecular system is described by the positions ($\bar{r}$) and the momenta ($\bar{p}$) of the N particles. The instantaneous value of a generic property (A) is a function of $[\bar{r}, \bar{p}]$. This value fluctuates continuously along the MD trajectory. An experimental measurement will always provide the mean value of the property A in a time interval. Thus, in order to compare simulations and experimental data, the temporal average of A needs to be computed. In an ideally infinite MD simulation, the temporal average ($\overline{A}$) is:

$$\overline{A} = \lim_{\tau \to \infty} \frac{1}{\tau} \int_0^{\tau} dt A(t) \qquad \textbf{Equation 2-12}$$

The ergodic hypothesis, which is usually postulated in molecular systems, states that the temporal average coincides with the ensemble average, $\langle A \rangle$ (i.e. average value on the accessible microstates of the thermodynamic system):

$$\langle A \rangle = \frac{\iint drdp\rho(r,p)A(r,p)}{\iint drdp\rho(r,p)} \qquad \textbf{Equation 2-13}$$

Where $\rho(r,p)$ is the probability density of the microstates. Multiplying both numerator and denominator of Equation 2-13 by $w(r,p)$, gives:

$$\langle A \rangle = \frac{\iint drdp\rho(r,p)w(r,p)A(r,p)}{\iint drdp\rho(r,p)w(r,p)} = \frac{\left\langle \frac{A}{w} \right\rangle_w}{\left\langle \frac{1}{w} \right\rangle_w} \qquad \textbf{Equation 2-14}$$

Where the subscript w is used for ensemble averages in a system with density of microstates equal to $\rho(r,p)w(r,p)$. The density of microstates is a function of the potential energy of the molecular system, which in the NVT ensemble satisfies:

$$\rho(r,p) \propto e^{-\frac{H(r,p)}{kT}} \qquad \textbf{Equation 2-15}$$

Where $H(r,p)$ is the Hamiltonian of the molecular system. Therefore, a change in the density of microstates is related to a change in the potential energy, and can be modeled as:

$$\rho'(r,p) \propto e^{-\frac{H'(r,p)}{kT}} = e^{-\frac{H(r,p)}{kT}} e^{-\frac{W(r)}{kT}} \propto \rho(r,p)w(r,p) \qquad \textbf{Equation 2-16}$$

Where the apex is used to indicate the variables in the molecular system with the modified potential energy.

Equation 2-14 states that instead of computing the ensemble average in the system with the original potential energy, the average can be computed in a

system with a modified potential energy. This observation is the key point of the umbrella sampling technique. Actually, the problem in the calculation of thermodynamic variables like entropy and free energies is the poor sampling of configurational space with low probability. A change in the potential energy can increase the probability of specific configurations, then Equation 2-14 can be used to estimate the average value of the property A in the original system.

A common situation in the simulation of molecular systems is the calculation of the free energy along a reaction coordinate, ξ. In this case it is sufficient to split the range of variability of the reaction coordinate in a set of windows. Then, a MD simulation is run for each window adding to the potential energy of the system an harmonic term, like:

$$W(\xi) = k_{\xi}\left(\xi - \xi_0\right)^2 \qquad \textbf{Equation 2-17}$$

Where ξ_0 is the center of the window, and k_{ξ} an elastic constant. If the elastic constant and the width of the window are properly defined, the system will be forced to explore the configurations around the ξ_0 value of the reaction coordinate. Afterwards, opportune numerical algorithms – like the Weighted Histogram Analysis Method (Kumar, 1992)– can be used to unbiased the data, and compute the free energy along the reaction coordinates in the original system, not biased by the harmonic potential $W(\xi)$.

2.3 Docking

Ion channels may interact with several pharmaceutical molecules, which can eventually alter the channel activity. Predict the structure of the channel-blocker molecular complex is of great interest for the pharmaceutical

research, since it can inspire the synthesis of new drugs, with higher affinity and selectivity. MD simulations, together with techniques for free energy calculations, are an accurate approach to estimate the structure of an intermolecular complex. However, in many practical cases an approach based on MD simulations is not feasible, because of the complexity of the molecular system and the consequent high-computational resources required for the simulation. Docking is a simplified approach to the problem, widely used for computer-aided drug design (Leach, 2006; Romano, 2007).

The basic idea of the docking method is to minimize the energy of interaction between the receptor and the ligand. Interaction energy is usually defined empirically, using for example, a set of ligand-receptor complexes where both the binding constants and the molecular structures are known (Aiay, 1995). Different docking procedures have been proposed. They can be classified according to the number of degrees of freedom taken into account. The simplest approaches use just six degrees of freedom, defining the relative position of the two molecules (Kuntz, 1982). At the other side of the spectrum, there are techniques that take into account molecular motions both of the ligand and the receptor (Leach, 1994). The calculations reported in this thesis used an intermediate approach, where the receptor – the ion-channel – is modeled as a static structure, while atomic motions in the ligand – the channel blocker – are taken into account (Morris, 1998). Once defined the degrees of freedom and the interaction energy, the docking algorithm is a minimization algorithm, which explore the configurational space searching for the most probable structure of the intermolecular complex.

2.4 Simplified Approaches to Simulate Ion Conduction

The simulation of the molecular dynamics of an ion channel embedded in a lipid membrane implies the simulation of a complex system, composed of

hundreds of thousands atoms. The complexity of the system limits molecular dynamics simulations to the nanosecond scale. This temporal scale is adequate to observe single conduction events (transit time in a potassium channel is in the nanosecond scale) but not to estimate channel current, whose computation requires the mean temporal proprieties of conduction to be known. Since ion current is an important functional characteristic of ion channels and can be determined experimentally (Sakmann, 1995), it is noteworthy to relate the channel conductance to its atomic structure. Most of the complexity lies in the large number of water molecules in the extracellular and intracellular compartments, thus the computational load is strongly reduced in models based on a continuum picture of the solvent. Brownian dynamics and Poisson-Nernst-Planck (PNP) electrodiffusion theory are possible approaches based on this idea. Brownian dynamics preserve the discrete nature of ions (Chung, 2002a; Noskov, 2004b), while PNP handles the whole system as a continuum. Since the studies presented in this thesis make an extensive use of the PNP approach, the PNP electrodiffusion theory is described in this section. The sub-section 2.4.1 deals with the formulation of the PNP mathematical model, while in sub-sections 2.4.2, 2.4.3 and 2.4.4 the numerical procedure used to solve the PNP differential equation set is described. A pseudo code of the numerical solver is listed in appendix A.

2.4.1 Poisson-Nernst-Planck Theory

The Poisson-Nernst-Planck electrodiffusion theory describes a steady state condition for a system of mobile charges. The mobile charges in membrane channels are the different ion species in solution. A continuum picture is used for the space distribution of ions, which are described by the concentrations $C_s(\vec{r})$ (subscript s marks the s-th ion species; $\vec{r}$ is the

position in space). The flux of the s-th ion species ($J_s(\vec{r})$) is modelled by the drift-diffusion equation (also named Nernst-Planck equation):

$$\vec{J}_s(\vec{r}) = -D_s(\vec{r})\vec{\nabla}C_s(\vec{r}) - \mu_s(\vec{r})C_s(\vec{r})\vec{\nabla}V_s(\vec{r}) \qquad \textbf{Equation 2-18}$$

Where $D_s(\vec{r})$, $\mu_s(\vec{r})$ are diffusion coefficient and mobility of the s-th ion specie; and $V_s(\vec{r})$ is the potential energy forcing the drift of the s-th ion specie. The first term, which is proportional to the concentration gradient, is due to diffusion processes, while the second is due to the drift forces acting on ions. Since the PNP theory describes a steady state condition, all quantities in Equation 2-18 are time independent. Moreover, because of the mass conservation law, the divergence of $J_s(\vec{r})$ is zero, which gives the set of differential equations (Continuity equation, Mass conservation law):

$$\vec{\nabla} \cdot \vec{J}_s(\vec{r}) = 0 \qquad s = 1,...,M \qquad \textbf{Equation 2-19}$$

With s ranging over the M ion species in solution. Assuming diffusion coefficients and mobilities as parameters (related by the Einstein relation $D/\mu = kT$, k Boltzmann constant and T absolute temperature), the mass conservation law (Equation 2-19) gives M equations with $2M$ unknown quantities: the ion concentrations ($C_s(\vec{r})$) and the potential energies ($V_s(\vec{r})$). The number of variables sensibly decreases if the driving forces are reduced just to the electrostatic forces. According to this approximation the potential energies are:

$$V_s(\vec{r}) = -ez_s\phi(\vec{r}) \qquad \textbf{Equation 2-20}$$

And the variables decrease to $M+1$ ($\phi(\vec{r})$ is the electrostatic potential, z_s is the valence of the s-th ion species, and e is the elementary charge). The PNP

theory formulation is completed by the relationship between the electrostatic potential and the ion concentrations. This relation is defined by the Poisson's equation:

$$\vec{\nabla}\cdot\left[\varepsilon(\vec{r})\phi(\vec{r})\right] = -\rho(\vec{r}) - \sum_{s=1}^{M} e z_s C_s(\vec{r}) \qquad \textbf{Equation 2-21}$$

Where $\varepsilon(\vec{r})$ is the dielectric constant; and $\rho(\vec{r})$ is the charge distribution of the protein atoms. Unlike ion charge distribution, the protein charge distribution is fixed in space, thus no protein atomic movements are included in the PNP theory.

2.4.2 Mathematical Model

In the PNP calculations presented in this thesis just two monovalent ion species are included in the mathematical model: one positive, to mimic potassium ions; and one negative, to mimic chloride ions. Thus, the PNP differential equation set is reduced to:

$$\begin{cases} \vec{\nabla}\cdot\left[D_{K^+}(\vec{r})\left[\vec{\nabla}C_{K^+}(\vec{r}) + \dfrac{e}{k_B T} C_{K^+}(\vec{r})\vec{\nabla}\phi(\vec{r})\right]\right] = 0 \\ \vec{\nabla}\cdot\left[D_{Cl^-}(\vec{r})\left[\vec{\nabla}C_{Cl^-}(\vec{r}) - \dfrac{e}{k_B T} C_{Cl^-}(\vec{r})\vec{\nabla}\phi(\vec{r})\right]\right] = 0 \\ \vec{\nabla}\cdot\left[\varepsilon(\vec{r})\nabla\phi(\vec{r})\right] = -\rho(\vec{r}) - eC_{K^+}(\vec{r}) + eC_{Cl^-}(\vec{r}) \end{cases} \qquad \textbf{Equation 2-22}$$

Once these equations are solved, ion concentrations and electrostatic potential are computed; then Equation 2-18 is used to calculate the ion fluxes, thus the channel currents.

A numerical algorithm, based on a Finite Differences approach, was implemented to solve the differential equations of the PNP theory (Equation 2-22). Two different discretization volumes were included in the algorithm: one cubic and one cylindrical. The cubic grid was the original choice, inspired by the availability of several routines for the discretization of the differential equations (Rocchia, 2002). The cylindrical grid is a more natural choice for the analysis of ion channels. In a cylindrical grid the volume is divided in slices orthogonal to the cylinder axis, and each slice is divided in segments and rings. As a consequence, the grid elements are tinier close to the cylinder axis and larger far from the axis. If the grid axis is chosen as the channel axis, a more accurate discretization in this region - where the analysis is usually focused - is obtained.

Poisson equation (Equation 2-21) was solved in the whole volume, while the continuity equations (Equation 2-19) were solved for the water solution only. As boundary condition for Poisson equation, the electrostatic potential on the boundary surfaces was assigned. The potential was set to zero on the upper boundary, whereas the membrane potential was applied at the lower boundary. For the potential of the side surfaces (six faces for the cubic grid, the lateral surface for the cylindrical grid), a linear interpolation between zero and the membrane potential was used. Two different boundary conditions were assigned for the continuity equations. On the upper and lower surfaces, the boundary conditions were the ion concentrations to simulate. To have electrically neutral boundaries on both faces, anion and cation concentrations were set equal. Boundary conditions on the side surfaces and at the separation surfaces with channel and membrane were:

$$\vec{J}_{K^+} \cdot \hat{i}_n = 0 \qquad \vec{J}_{Cl^-} \cdot \hat{i}_n = 0 \qquad \textbf{Equation 2-23}$$

Where $\hat{i}_n$ is the surface normal vector. In this way, no ion flux was allowed through these surfaces.

2.4.3 Partial Differential Equation Solver

The numerical procedure used to discretize the continuity equation for potassium ions in the cylindrical grid is presented here. The generalization to the Poisson equation and to the cubic grid is immediate. Three indexes (i,j,k) are used to identify an element in the grid. Figure 2-1 defines the direction associated with these three indexes.

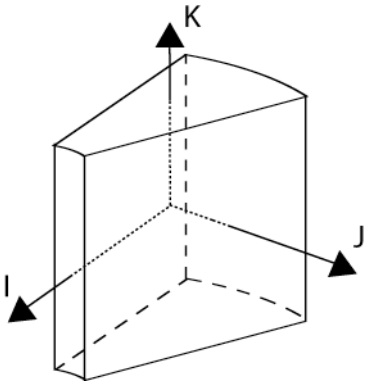

Figure 2-1 Grid element

The outwards ion fluxes from the grid element (i,j,k) were defined as ($C_{i,j,k}$ is the potassium concentration in the grid element, $\phi_{i,j,k}$ the electrostatic potential):

$$J_{i-1} = -\frac{D_{i,j,k} + D_{i-1,j,k}}{2}\left[\frac{C_{i-1,j,k} - C_{i,j,k}}{dr} + \frac{e}{kT}\frac{C_{i,j,k} + C_{i-1,j,k}}{2}\frac{\phi_{i-1,j,k} - \phi_{i,j,k}}{dr}\right]$$

$$J_{i+1} = -\frac{D_{i,j,k} + D_{i+1,j,k}}{2}\left[\frac{C_{i+1,j,k} - C_{i,j,k}}{dr} + \frac{e}{kT}\frac{C_{i,j,k} + C_{i+1,j,k}}{2}\frac{\phi_{i+1,j,k} - \phi_{i,j,k}}{dr}\right]$$

$$J_{j-1} = -\frac{D_{i,j,k} + D_{i,j-1,k}}{2}\left[\frac{C_{i,j-1,k} - C_{i,j,k}}{dtdr(i+0.5)} + \frac{e}{kT}\frac{C_{i,j,k} + C_{i,j-1,k}}{2}\frac{\phi_{i,j-1,k} - \phi_{i,j,k}}{dtdr(i+0.5)}\right]$$

$$J_{j+1} = -\frac{D_{i,j,k} + D_{i,j+1,k}}{2}\left[\frac{C_{i,j+1,k} - C_{i,j,k}}{dtdr(i+0.5)} + \frac{e}{kT}\frac{C_{i,j,k} + C_{i,j+1,k}}{2}\frac{\phi_{i,j+1,k} - \phi_{i,j,k}}{dtdr(i+0.5)}\right]$$

$$J_{k-1} = -\frac{D_{i,j,k} + D_{i,j,k-1}}{2}\left[\frac{C_{i,j,k-1} - C_{i,j,k}}{dz} + \frac{e}{kT}\frac{C_{i,j,k} + C_{i,j,k-1}}{2}\frac{\phi_{i,j,k-1} - \phi_{i,j,k}}{dz}\right]$$

$$J_{k+1} = -\frac{D_{i,j,k} + D_{i,j,k+1}}{2}\left[\frac{C_{i,j,k+1} - C_{i,j,k}}{dz} + \frac{e}{kT}\frac{C_{i,j,k} + C_{i,j,k+1}}{2}\frac{\phi_{i,j,k+1} - \phi_{i,j,k}}{dz}\right]$$

Equations 2-24

Where J_{i-1} is the outward flux between the grid elements (i,j,k) and $(i-1,j,k)$ - a coherent nomenclature is used for the fluxes in the other directions; and dr, dt and dz are the grid steps in the I, J and K directions, as defined in Figure 2-1. Equations 2-24 are nothing else but the lattice versions of Equation 2-18. According to the mass conservation law, the net steady state flux through any grid element is zero, that is:

$$J_{i-1}S_{i-1} + J_{i+1}S_{i+1} + J_{j-1}S_{j-1} + J_{j+1}S_{j+1} + J_{k-1}S_{k-1} + J_{k+1}S_{k+1} = 0$$

Equation 2-25

$$S_{i-1} = i(drdtdz)$$
$$S_{i+1} = (i+1)(drdtdz)$$
$$S_{j-1} = S_{j+1} = drdz$$
$$S_{k-1} = S_{k+1} = (i+0.5)dtdr^2$$

Equations 2-26

Where S_{i-1} is the boundary surface between the grid elements (i,j,k) and $(i-1,j,k)$, and a coherent nomenclature is used for the other boundary surfaces. Replacing in Equation 2-25 the Equations 2-24 and the Equations

2-26, the concentration in the grid element (i,j,k) and in the six surrounding grid elements are related by:

$$C_{i,j,k}\sum_{rnd}\frac{D_{i,j,k}+D_{rnd}}{2}\left[1+\frac{ez}{2kT}\left(\phi_{rnd}-\phi_{i,j,k}\right)\right]S_{rnd}-$$
$$-\sum_{rnd}C_{rnd}\frac{D_{i,j,k}+D_{rnd}}{2}\left[1-\frac{ez}{2kT}\left(\phi_{rnd}-\phi_{i,j,k}\right)\right]S_{rnd}=0$$

Equation 2-27

Where *rnd* is an index that rounds over the six surrounding grid elements. In case one of the surrounding grid elements does not belong to the water solution compartment, the flux toward it will be zero, and the corresponding term in Equation 2-27 will disappear. On the other way, if one of the surrounding elements has a fix ion concentration, like in the upper and lower boundaries, the corresponding concentration in Equation 2-27 will not be an unknown quantity, but a given value. Equation 2-27 can be rewritten in a matrix form:

$$A\bar{c}=\bar{b}$$ **Equation 2-28**

Where $\bar{c}$ is the unknown array of ionic concentrations; and $\bar{b}$ is a given array, function of the electrostatic potential, the boundary concentrations, and the diffusion coefficients profile. The matrix A is a function of the electrostatic potential and the diffusion coefficients profile, as defined by Equation 2-27.

The linear systems representing the partial differential equations of the PNP model (Equation 2-28) were solved by the Bi-conjugate Gradient Stabilized (BiCGS) Algorithm (Vorst, 1992). BiCGS is a non-stationary iterative method, suitable for the solution of large linear system. Unlike stationary

methods (as Successive Over-Relaxation (Young, 1971)), non-stationary methods exploit in the computation information that changes at each iteration. Typically, inner products of residual or related vectors are used to update the searching direction and the update-weight. For a more detailed description, the code of the BiCGS algorithm is included in Appendix A. The BiCGS algorithm was chosen because of the smooth converge to solution, even in non-symmetric linear system. This is not necessary for the Poisson equation, which is described by a positive definite matrix, but it is crucial for the solution of the continuity equations. Indeed, the linearization of the continuity equations gives linear system with non-symmetric matrix, and the convergence to solution of the other algorithms tested (Successive Over-Relaxation, Conjugate Gradient, Bi-conjugate Gradient, Conjugate Gradient Squared (Barrett, 1994)) was not guaranteed.

2.4.4 Iterative Algorithm

The differential equation set (Equation 2-22) was solved by an iterative scheme. At the first step, the electrostatic potential was computed solving Poisson equation with ion concentrations set to zero. Then, the electrostatic potential was updated, according to:

$$\overline{\phi} = (1 - w_P)\overline{\phi}_{old} + w_P\overline{\phi}_P \qquad \textbf{Equation 2-29}$$

Where $\overline{\phi}_{old}$ is the electrostatic potential in the previous step (zero in the first step); and $\overline{\phi}_P$ is the electrostatic potential obtained by the solution of the Poisson equation. The updating-weight (w_P) is a parameter of the algorithm, twiddled to guarantee the convergence of the iterative procedure. Once updated the electrostatic potential, the ion concentrations are computed by the solution of continuity equations. Then, the ion concentrations are updated with the same scheme used for the electrostatic potential (Equation 2-29),

but using a different updating-weight (w_N). Again the updating-weight is an algorithm parameter, twiddled to guarantee the convergence. The iterative procedure is repeated until a self-consistent solution is reached. The convergence is tested by the root mean square deviation between two successive iterations. A scheme of the algorithm is given in appendix A

2.5 Homology Modelling

A prerequisite to analyze the structure-function relation in protein molecules, like ion channels, is to know the atomic structure of the protein. Protein molecules are sequences of aminoacids, bounded by amide bonds. While it is relatively easy to identify the sequence of aminoacids forming a protein (primary structure), it is far more difficult and expensive to solve its three-dimensional atomic structure (quaternary structure). Indeed, the number of known primary structures overwhelms the number of known quaternary structures. As a result, there is a remarkable interest in theoretical methods to predict the atomic structure of a protein molecule from its aminoacid sequence. This problem is known as the *protein folding problem*, and it is one of the major topics in computation chemistry. An extensive introduction to the topic is not the purpose of this section, however computational methods for the prediction of protein structures are used in Chapter 5, so the basic scheme of the adopted method is introduced in the remaining of the section.

The theoretical approaches to predict protein structures can be classified in two categories: *ab initio* methods, and homology modeling (also known as comparative modeling). *Ab initio* methods try to define the protein atomic structure from first principle. The idea is to identify the most favourable energetic configuration of the protein, searching in the configurational space. The number of possible configurations of a protein is overwhelming, which hampers the usage of *ab initio* methods. MD simulations have been used to

analyze protein folding, but their application is still limited to simple polypeptides (Garcia, 2007; Wu, 2004). Homology modeling uses a complete different strategy (Ginalski, 2006). A reasonable hypothesis is that proteins with similar aminoacid sequences have similar three-dimensional structures. Thus, if a target protein has a primary structure similar to a template protein - with known three-dimensional structure - it is possible to model the atomic structure of the target protein on the template protein. Modeling the quaternary structure by homology modelling consists of three phases. First a template protein with known atomic structure has to be identified. Then, a sequence alignment between the two proteins has to be defined, and finally the target protein can be modeled on the template protein, according to the alignment. The quality of the model can be improved by including more than one template proteins in the homology-modeling scheme (Shatsky, 2007), or by refining the structure through energy minimization and MD simulations.

Homology modeling is used in Chapter 5 to define possible atomic structures of the pore region of the hErg and hEag1 potassium channels. Identifying the template protein and the sequence alignment in this case was straightforward, because of the similarity of the pore region among different potassium channels.

PART II

Research Projects

Chapter 3

Application of the Poisson-Nernst-Planck Theory to KcsA

The Poisson-Nernst-Planck electrodiffusion theory (see section 2.4) serves to compute charge fluxes and is here applied to the ion current through a protein channel. KcsA was selected as an example because of the abundance of experimental and theoretical data. The potassium channels MthK and KvAP were used as templates to define two open channel models for KcsA. Channel boundary surfaces and protein charge distributions were defined according to atomic radii and partial atomic charges. To establish the sensitivity of the results to these parameters, two different sets were used. Assigning the potassium diffusion coefficients equal to the value for free-diffusion in water (1.96×10^{-9} m^2/s), the computed currents overestimated the experimental data. Ion distributions inside the channel suggest that the overestimate is not due to an excess of charge shielding. A good agreement with the experimental data was achieved by reducing the potassium diffusion coefficient inside the channel to 1.96×10^{-10} m^2/s, a value of substantial motility but nonetheless in accord with the intuitive notion that the channel has a high affinity for the ions and therefore slows them down. These results are independent of the open channel model and the parameterization adopted for atomic radii and partial atomic charges. The method offers a reliable estimate of the channel current with low computational effort.

Most of the content of this chapter has been published in: S.Furini, F. Zerbetto, S. Cavalcanti, "Application of the Poisson-Nernst-Planck equations with space dependent diffusion coefficients to KcsA", Biophys J, 92(9):3017-27, Oct 2006.

3.1 Introduction

Ion channels are proteins embedded in the cell membrane that allow the flow of chemical species through the hydrophobic lipid bilayer (see section 1.1). The atomic structure of bacterial channels selectively permeable to potassium ions - KcsA, MthK, and KvAP- was characterized by X-Ray crystallography (Doyle, 1998; Jiang, 2002a; Jiang, 2003). The pore region is remarkably conserved among different potassium channels, as outlined in section 1.2. However, the structure of the intracellular mouth differs in the crystallographic structures of KcsA, MthK and KvAP. In KcsA a bundle among the inner helices, close to the intracellular mouth, reduces the hydrophobic pore diameter to 4 Å, preventing ion fluxes through the channel: this configuration corresponds to a functionally closed state. In MthK and KvAP an outward movement of the inner helices, accomplished by bending around a hinge glycine, opens the intracellular mouth (Figure 3-1). The structures of MthK and KvAP are representative of open states for potassium channels (Jiang, 2002b).

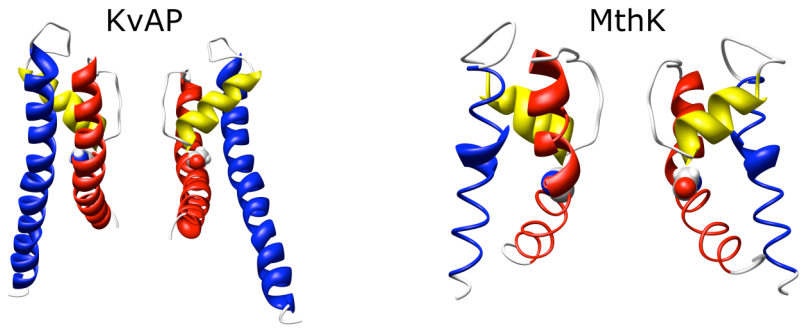

Figure 3-1 KvAP and MthK channels
Side views of MthK and KvAP channels. A rotation around the hinge glycines (highlighted in the CPK mode) opens the intracellular channel mouths to different extents in the two channels.

Molecular dynamics (MD) simulations have disclosed the atomic details of conduction and selectivity (Allen, 1999; Aqvist, 2000; Berneche, 2000; Compoint, 2004; Shrivastava, 2000), but they cannot routinely predict the ion current through the channels (Chung, 2002b) because of the timescale of ion transport (see section 2.4). A conductivity estimate of KcsA in good agreement with the experimental data was obtained by Brownian Dynamics simulations based on a potential of mean force computed by MD (Berneche, 2003). Applications of the PNP theory to membrane ion channels are more controversial (Corry, 1999). In wide channels this approach reproduces the experimental data quite well (Nonner, 1999). On the other hand, the applicability of the PNP theory to narrow channels - with radii lower than 2 Deybe lengths - has been challenged (Corry, 2000). An overestimate of charge shielding inside the channel was indicated as the main cause of the PNP quantitative failure in these channels (Corry, 2003).

Testing of the PNP theory in narrow channels was limited to simplified channel models: simple cylindrical channels or models shaped on KcsA without explicitly including the protein charge distribution (Corry, 2000). In this chapter the PNP theory is used to predict the conductance of the KcsA potassium channel, including the atomic coordinates in the mathematical model. Two different open channel models are used for open KcsA. One is based on MthK, the other on KvAP. In PNP, channel boundary surfaces and protein charge distributions are defined according to atomic radii and partial atomic charges. Two different sets of parameters are used to assess the sensitivity of the results to these parameters. Independently of the parameterization and the open channel model adopted, the same results are reached: i) inside the selectivity filter anion concentration is several orders of magnitude lower than cation concentration; ii) the PNP theory overrates experimental data when diffusion coefficients are set at the experimental values for free diffusion in water, but a reasonable decrease of ion motility inside the channel makes experiments and theory coincide; iii) cation

distribution in the selectivity filter (SF) is characterized by four peaks corresponding to the potassium binding sites S1-S4 (see Figure 1-2).

3.2 Methods

3.2.1 KcsA Models

The three-dimensional atomic coordinates of the KcsA channel were taken from the crystallographic structure determined at 2Å resolution by Y. Zhou et al. (Zhou, 2001) (File 1K4C.pdb in the Protein Data Bank). The atomic coordinates of the first 21 amino acids at the N terminal and of the last 36 at the C terminal are not determined experimentally. Since both C and N terminals are located in the cytoplasm, far from the conduction pathway, these amino acids are not crucial for the present study and therefore were not included in the channel model. Side chains with missing atoms were completed using ideal internal coordinates from the AMBER99 force field (Case, 2004), the same procedure was used to add the hydrogen atoms. All the ionizable residues were assumed in the default protonation state except Glu71, assumed protonated (Berneche, 2002). An acetyl and an N-methylamine group were added to the C and N terminal, respectively.

The experimental structure of KcsA corresponds to a closed state of the channel. To compute ion fluxes it is necessary to use an open channel structure. Closure of KcsA is due to a bundle of the four inner helices at the intracellular channel mouth (Doyle, 1998). A connection between channel opening and outward movements of the transmembrane helices was first proved by Electronic Paramagnetic Resonance experiments (Perozo, 1999). These movements were further characterized by the X-Ray crystallographic structure of MthK (1LNQ.pdb), which, unlike KcsA, was crystallized in an open state (Jiang, 2002a). MthK and KcsA structures are very similar, except in the inner helices. These helices are bent at the amino acid Gly83 in MthK,

and, as a consequence, the selectivity filter is connected to the intracellular space by a wide pore (minimum radius 6 Å). High conservation of this hinge glycine among different potassium channels suggests a common mechanism for channel gating. Despite this common mechanism, the inner helix bending can differ in different channels. In the crystallographic structure of KvAP (1ORQ.pdb) (Jiang, 2003) the inner helices bending, hence the pore opening, is lower than in MthK (Figure 3-1). It is not currently known if the KcsA open state is more similar to KvAP or to MthK, or if an intermediate configuration is adopted. Consequently, two different open channel models were used to test the PNP theory: one based on MthK (Model I) and one based on KvAP (Model II).

To define these models, MthK and KvAP were superimposed on KcsA, minimizing the root mean square distance (RMSD) among the selectivity filter atoms. Channel structures differ mainly in the C terminal of the inner helix, after the hinge glycine (Gly83 in MthK, Gly99 in KcsA, and Gly220 in KvAP). Smaller structural differences are localized in the outer helices. KcsA backbone angles in the inner and outer helices were modified to minimize the RMSD with backbone atoms of MthK (Model I) or KvAP (Model II). In detail, Model I was defined superimposing the amino acids 22-45 and 99-114 of KcsA with the amino acids 19-42 and 83-98 of MthK; Model II was defined superimposing the amino acids 22-60 and 99-119 of KcsA with the amino acids 134-172 and 220-240 of KvAP. Open channels structures were refined by 500 steps of energy minimization, using the SANDER module of AMBER. During minimization backbone atoms were restrained by a harmonic potential, with a force constant of 40 Kcal*mol/$Å^2$ to avoid large backbone displacements. A similar procedure to define open channel structures was previously used to perform Poisson Boltzmann calculations in KcsA (Jogini, 2005).

Channel models are completed by atomic radii and partial atomic charges, needed to define channel boundaries and protein charge distribution. These

parameters were taken from the AMBER99 force field. To test the effects of the parameterization on the results, a second set of channel models was defined using the atomic radii and partial atomic charges proposed by Nina et al. (Nina, 1997).

3.2.2 Numerical Solver

The Poisson-Nernst-Planck equation set was solved numerically considering a cubic volume divided into three distinct sub-volumes: the ion channel, the membrane, and the water solution. The channel was placed with its geometric centre at centre of the cube and with the pore axis orthogonal to the upper and lower faces. The extracellular side of the channel pointed to the upper face. The height of the cube was twice the channel length along the pore axis (z axis). The position, radius, and partial charge of all the atoms define the ion channel sub-volume. To separate extracellular and intracellular spaces, a sub-volume surrounding the channel and extending between two planes orthogonal to the pore axis was included. This volume corresponds to the lipid bilayer of the cell membrane. The water solution spreads throughout the volume not occupied by channel and membrane. A mesh of 200x200x200 cubic grid elements was used to discretize the whole volume. The channel was meshed on the grid using the discretization algorithm implemented in DELPHI, a well-known Poisson-Boltzmann equation solver (Rocchia, 2002). The Poisson-Nernst-Planck differential equation set was solved by the iterative algorithm described in section 2.4.

3.2.3 Parameter Assignment

The relative dielectric constant was set at 80 for the water solution and 2 for the channel and the membrane. To define membrane thickness the position of the aromatic residues Trp113 (z = -16 Å) and Trp87 (z = 14 Å) of the

inner helices was used. The water relative dielectric constant is probably below 80 in the channel interior due to the small volume and to the consequently reduced mobility of water molecules. At the same time, because of the mobile charges, the channel dielectric constant can locally differ from 2. To assess the sensitivity of the results to the assignment of this parameter we tested the effects of small changes in the relative dielectric constant with respect to reference values (relative dielectric constant set at 60 for water solution and 4 for the channel).

The diffusion coefficients were assigned considering three distinct regions: the channel outside (CO) corresponding to $z > 15.5$ Å and $z < -15.5$ Å, the selectivity filter (SF) spanning from $z = -0.5$ Å to $z = 15.5$ Å and the intracellular chamber (IC) from the intracellular channel mouth, $z = -15.5$ Å, to the intracellular end of the SF, $z = -0.5$ Å. Outside the channel the diffusion coefficients were set at $D^+ = 1.96 \times 10^{-9} m^2/s$ and $D^- = 2.03 * 10^{-9} m^2/s$, according to the experimental values of free-diffusion in water solution for potassium (D^+) and chloride (D^-) (Lide, 2004). Since the mean radii of SF and IC are 1.4 Å and 5 Å to 7 Å, depending on the channel model, ions and water molecules in these areas interact with the channel, requiring a different value of the diffusion coefficients. MD simulations predicted a potassium diffusion coefficient one order of magnitude lower in SF and roughly half in IC (Allen, 1999; Allen, 2000). To assess the effects of space dependent diffusion coefficients on the computed currents, we tested four diffusion coefficient profiles within the channel: i) equal to the free diffusion values, both in SF and IC; ii) reduced to 10% in SF; iii) reduced to 10% in SF and 50% in IC; iv) reduced to 10% both in SF and IC. Computed currents were compared with KcsA experimental single channel currents measured in a planar bilayer system (LeMasurier, 2001).

3.3 Results

The ion currents predicted by the PNP theory (Figure 3-2) overestimated the experimental data when the diffusion coefficients were assigned to the typical values for free-diffusion in water in the whole system (SF, IC and OC). For the current-voltage characteristics (Figure 3-2A-B, dashed green line), the percentage relative inaccuracy was large, independently of the membrane potential (at 25 mV 360% for Model I and 220% for Model II; at 200 mV 430% for Model I and 260% for Model II). By contrast, boundary ion concentrations strongly affected the percentage deviation as shown by the current-concentration characteristics in Figure 3-2C-D, dashed green line (at 20 mM 160% for Model I and 50% for Model II; at 400 mM 440% for Model I and 380% for Model II). The conclusion is that the PNP theory, with constant diffusion coefficients, cannot reproduce the currents properly, especially at high ion concentrations.

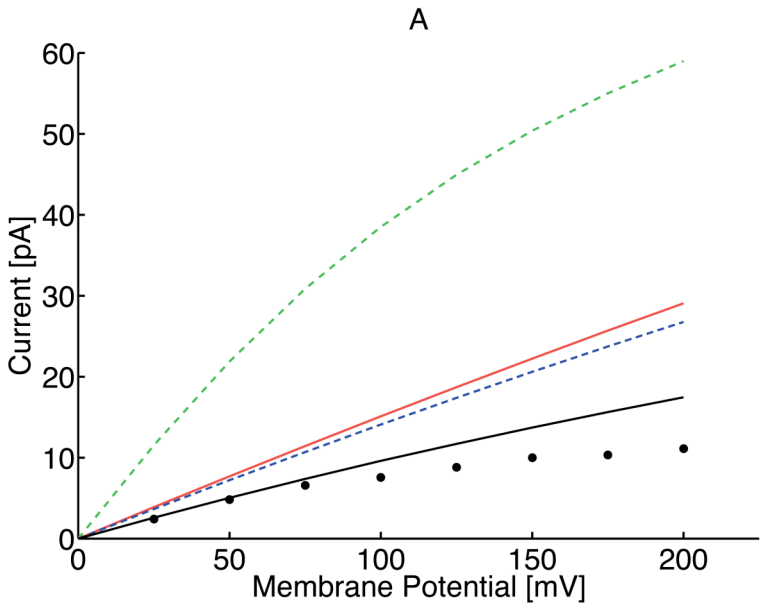

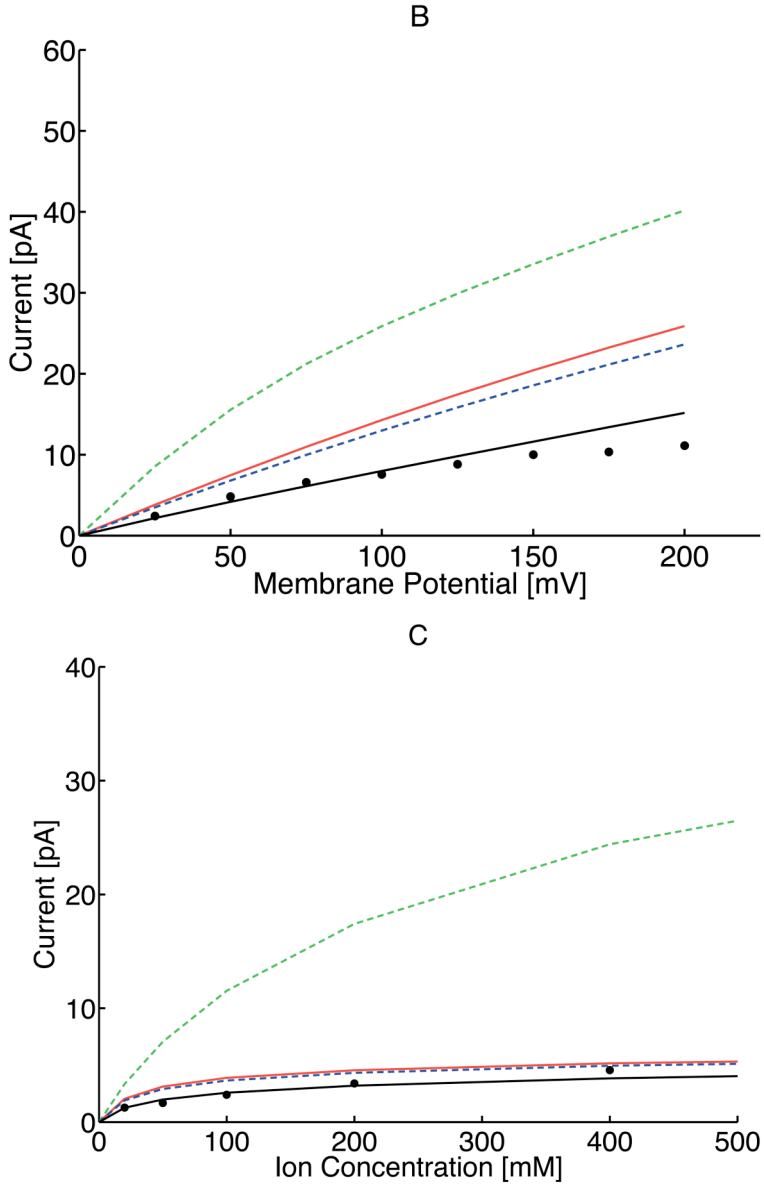
B
Current [pA]
Membrane Potential [mV]
C
Current [pA]
Ion Concentration [mM]

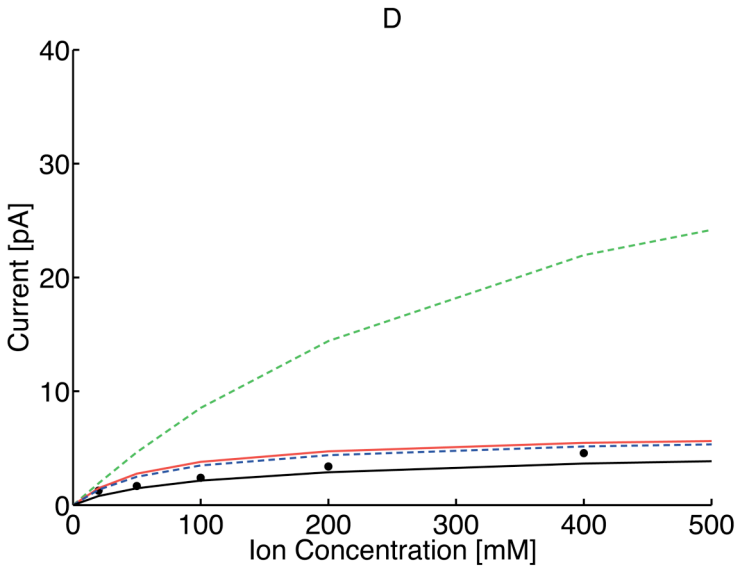

Figure 3-2 Computed currents varying the diffusion coefficients (D)
D was set at the bulk value in the whole system (dashed green line); D was reduced to 10% of bulk in SF (red line); D was reduced to 10% in SF and to 50% in IC (dashed blue line); D was reduced to 10% both in SF and IC (black line). Experimental data by LeMasurier et al. (●). (A) Current-voltage characteristic with ion concentrations set at 100 mM in Model I. (B) Current-voltage characteristic with ion concentrations set at 100 mM in Model II. (C) Current-concentration characteristic with membrane potential set at 25 mV in Model I. (D) Current-concentration characteristic with membrane potential set at 25 mV in Model II.

To establish whether the quantitative failure of the PNP theory is connected with charge shielding overestimate, the ion concentrations inside the channel were analyzed. The amount of positive charge inside the SF (with boundary ion concentrations set at 100 mM and membrane potential at 25 mV) was around 2 elementary charges for both channel models. Under the same conditions, the negative charge was less than 10^{-1} elementary charges. Thus the positive charge is almost unshielded in the narrowest region of the channel, and consequently charge shielding overrate cannot really be the main cause of the PNP failure. Ion concentrations along the channel pore further confirmed this conclusion (Figure 3-3). The ratio between positive and negative charge inside the SF decreased when boundary ion concentrations were increased, and consequently charge shielding rose. Ion

concentrations as high as 800 mM were tested and even in this case the ratio was higher than 10. Thus, even if the problem of shielding overrate at high concentration exists, it does not introduce quantitative deviations in the physiological range. Anion exclusion from the channel inside entails a channel current made up mainly of the positive charge flux. The ratio between positive and negative ion fluxes was higher than 3000 for both channel models (membrane potential set at 25 mV and ion concentrations at 100 mM). This ratio, just like the ratio between ion charges in the SF, decreased by increasing ion concentrations, but even at 800 mM it was higher than 200.

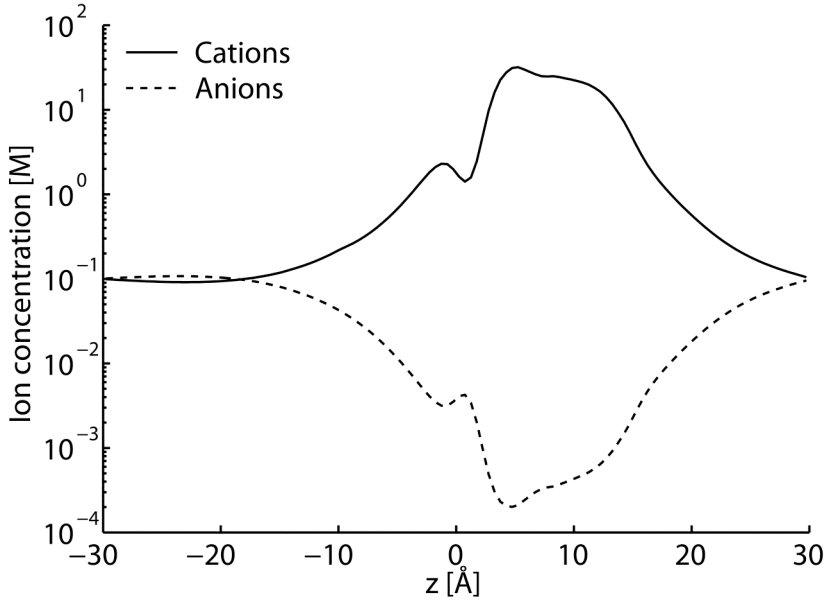

Figure 3-3 Ion concentrations along the channel axis
Model I; Boundary ion concentrations set at 100 mM; Membrane potential at 25 mV.

The agreement between computed and experimental data improved using lower values of diffusion coefficients in SF and IC (Figure 3-2). All the data shown were obtained reducing both diffusion coefficients. Since most of the current is due to positive ion fluxes, similar results would have been reached

by reducing just the positive ion diffusion coefficient. A reduction to 10 % of diffusion coefficients in the SF greatly improved the agreement with the experimental currents, especially at high ion concentrations. In fact, current overrate does not increase when boundary ion concentrations are increased (Figure 3-2C-D, red line). Thus, the reduction of diffusion coefficients, even restricted to a specific region of the pore, is enough to reproduce the current saturation at high ion concentrations. This result was confirmed for both channel models. Better agreement with the experimental data was reached (Figure 3-2) by reducing the diffusion coefficients also in the IC. Among the different diffusion coefficient profiles tested, the best agreement was reached by a reduction to 10 % both in SF and IC, independently of the channel model. The agreement was particularly satisfactory for physiological conditions (membrane potential up to 100 mV; ion concentrations in the range 50 mM – 200 mM), where the mean relative deviation was 13% and 8% for Model I and II, respectively.

Similar results were obtained using the parameterization proposed by Nina et al. for atomic radii and partial atomic charges (Figure 3-4). Also with this parameterization the best agreement with the experimental data was reached by a reduction of diffusion to 10% in SF and IC, with a mean relative deviation of 15% and 20% for Models I and II, respectively.

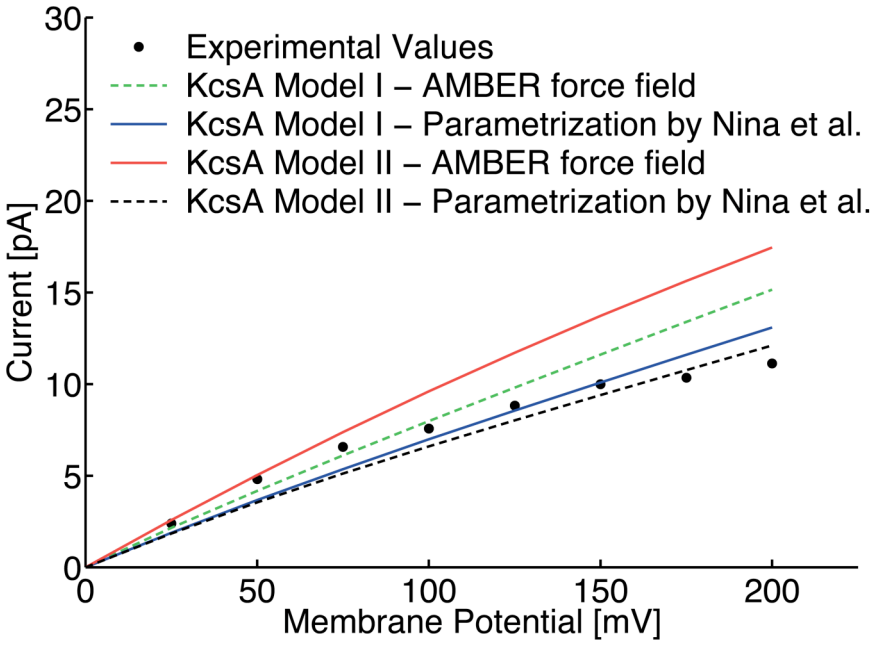

Figure 3-4 Current-voltage characteristics in 100 mM symmetric ion concentrations

As a further test of the PNP theory in potassium channels the positive ion distribution in the SF was analysed. The channel inside was divided into slices orthogonal to the pore axis and an ion occupancy index was defined in each slice, according to:

$$O = \frac{n_{ion} V_{ion}}{V_{slice}} \qquad \textbf{Equation 3-1}$$

Where V_{slice} is the slice volume, n_{ion} the number of ions in the slice (computed by ion concentration) and V_{ion} the ion volume (defined according to standard Pauling radii). Independently of the channel model and the parameterization adopted, the cation occupancy profile shows four peaks in the SF, corresponding to the potassium binding sites S1-S4 (Figure 3-5). The occupancy values in these peaks ranged from 0.2 to 0.5, depending on

boundary ion concentrations. These results agree with the data obtained by X-Ray crystallography (Zhou, 2003).

A dielectric constant change to 60 for water solution and 4 for membrane and protein did not significantly alter the previous results.

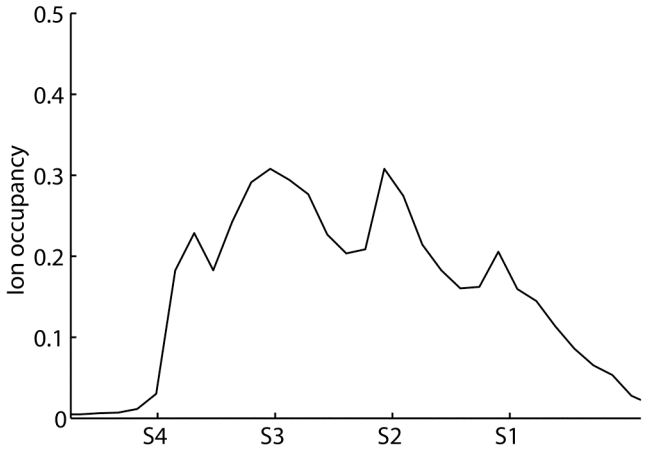

Figure 3-5 Cation occupancy index inside the selectivity filter
The positions of the binding sites S1-S4 are marked on the ordinate axis. (Model I; Boundary ion concentrations set at 100 mM; Membrane potential at 25 mV).

3.4 Discussion

The applicability of the PNP electrodiffusion theory to narrow ion channels (with internal radius lower than 2 Deybe lengths) has been challenged (Corry, 1999). The PNP theory describes the charge distribution by continuum functions, thus neglecting the discrete nature of ion charge. The consequence of this assumption is an overestimate of charge shielding near dielectric boundary surfaces. Overestimate of the shielding effect can lead to overestimate of both ion concentrations in the channel and ion fluxes. This inaccuracy was quantified by comparing the PNP theory with Brownian Dynamics (BD) and Dynamic Lattice Monte Carlo simulations (DLMC) (Corry, 2000; Graf, 2004). The discrete nature of ion charges is preserved by

BD and DLMC. The overestimate of the shielding effect introduced by PNP is reduced in the presence of fixed charges at the boundary surfaces. If the fixed charges are negative, as in the selectivity filter of potassium channels, many more positive than negative ions enter. The partial exclusion of negative charges from the channel inside limits the positive charge shielding. The improvement of the PNP theory prediction in the presence of fixed charges was confirmed by comparison with BD using a simplified channel model (Corry, 2000), but no previous study was based on the experimental atomic structure of an ion channel. In the present study a finite differences numerical algorithm was used to solve the PNP equations in three dimensions. The algorithm was applied to compute ion fluxes through the KcsA channel, described by its experimental atomic structure, partial atomic charges and radii. KcsA was chosen for the wide availability of experimental functional data (fluxes and ion concentrations in the selectivity filter). The current predicted by the PNP theory overestimated the experimental data when diffusion coefficients were set at the bulk experimental values, but the overestimate was not due to wrong charge shielding. When the experimental atomic structure of the channel is used, the concentration of negative ions in the narrowest part of the channel is negligible, due to the presence of negative fixed charges in the channel protein. Thus in this region no shielding is introduced by the PNP theory.

PNP theory predictions were improved by using space dependent diffusion coefficients. Four different diffusion coefficient profiles were tested. The best fit of the experimental data was achieved by a reduction of diffusion to 10% both in SF and IC. This result was independent of (i) the specific model adopted for the open channel structure; (ii) the atomic radii and partial atomic charges parameterization; (iii) small changes in the relative dielectric constants. The fit could be further improved for a specific parameterization and channel model, by minor adjustments of the diffusion coefficients. However, the aim of the present study was not to find this optimal fitting but

to test the PNP theory in a channel model based on the protein atomic structure and to investigate the possibility to predict the experimental currents by adopting a reasonable reduction of diffusion coefficients inside the channel. According to these results we conclude that when the PNP theory is applied to a channel model based on the protein atomic structure, the experimental currents can be fitted by reducing ion motility inside the channel. Indeed, a reduction to 10% of the potassium diffusion coefficient in the SF agrees with MD simulations (Allen, 1999) and in further MD simulations, the potassium diffusion coefficient reduction in IC was gauged at around 50% (Allen, 2000). The focus on the potassium diffusion coefficient is justified since the cation fluxes are far higher than anion fluxes. Application of the PNP theory to Gramicidin, another narrow ion channel, required a similar reduction of diffusion coefficients to reproduce the experimental data (Cardenas, 2000; Kurnikova, 1999). The agreement between our procedure and that used for Gramicidin strengthens the case for a systematic reduction of diffusion coefficients in narrow ion channels when the PNP model is used.

The K^+ fluxes are not only due to the shear transport within the channel, but are also determined by association and dissociation processes with the local atomic charges of the filter (Mafe, 2005). The latent periods due to these processes are not included in the PNP theory and so a reduced diffusion coefficient of potassium compensates for this theory limitation. In practice, the value of the diffusion coefficients used to reproduce the experimental currents can be considered an effective parameter that is ultimately determined by the approximations used to obtain the PNP approach. The main approximations are: (i) the discrete nature of ions is neglected and aspects such the exclusion of an ion from an already occupied binding site are not taken into account; (ii) the channel is modelled as a static structure, while the protein conformation changes are almost instantaneous with respect to the time involved in the conduction process (Allen, 2004).

Aside from these limitations, the simple method proposed reproduces the experimental current and the position of the ion binding sites quite well. Compared to an approach based on Brownian dynamics, the PNP approach needs far fewer computational resources. PNP can therefore be a useful preliminary method to analyze the effects of protein structural changes on channel currents, providing a simple way to analyze channel functioning (see Chapter 4).

Chapter 4

Molecular Determinants of the Potassium Channel Conductance

In this chapter the role of several fragments of the potassium channel KcsA is examined, using the Poisson-Nernst-Planck theory. The efficiency of the computational method allowed comparing a large number of channel models, with different intracellular gate openings, partial atomic charges, and aminoacid sequences. Perhaps counter-intuitively, the calculated ion current decreases when the mean radius of the entrance cavity increases. Widening of the vestibule, in fact, increases the volume accessible to water, which is the volume with a high dielectric constant. In turn, water screens the attractive charges of the P-loop backbone. The backbone charges of the M2 helixes instead oppose the entrance of Potassium ions through a complicated mechanism that can be separated in the activity of two interfering dipoles. The conductance of the KcsA models increased when two neutral residues in M2 were mutated to glutamic acid, in agreement with previous experimental results. As a general conclusion, a relation between channel conductance and Potassium concentration in the intracellular cavity emerged. Although the ion transport is the result of the fine balance of a number of different effects, the experimental results can be reproduced quantitatively only on the basis of electrostatic forces, which are the only driving forces modelled by the PNP theory.

Most of the content of this chapter has been published in: S. Furini, F. Zerbetto, S. Cavalcanti, ”The role of the intracellular cavity in potassium channel conductivity”, J Phys Chem B,111(50):13993-4000, Dec 2007.

4.1 Introduction

In this chapter the relation between atomic structure and conductance in potassium channels is theoretically analyzed, by a continuum model of electrodiffusion in the Poisson-Nernst-Planck formulation.

The atomistic comprehension of the role of the protein architecture on channel conductance can be reached by computer simulations, which require the detailed knowledge of the structure of the protein (see Chapter 2). The crystallographic structures of five distinct potassium channels (KcsA, MthK, KvAP, KirBac1.1 and Kv1.2) reveal a common architecture of the pore (Doyle, 1998; Jiang, 2002a; Jiang, 2003; Kuo, 2003; Long, 2005). The pore architecture is described in section 1.2, and shown in Figure 4-1 for the potassium channels KcsA, KvAP and MthK. In this chapter the name M1 will be used for the outer helixes (blue helixes in Figure 4-1), while the name M2 will be used for the inner helixes (red helixes in Figure 4-1). In spite of the high similarity of their architectures, the conductance of potassium channels varies widely (Hille, 2001). Channels belonging to the BK family have a conductance almost two orders of magnitude higher (~200pS) than other potassium channels, such as the voltage gated channels (Latorre, 1989). The selectivity filter itself is not likely to cause this variability, since it retains the same atomic structure in channels characterized by very different conductances. Conversely, the cytoplasmatic, water-filled vestibule at the centre of the membrane shows some variability (Shealy, 2003). This intracellular cavity regulates the exchange of ions between the intracellular compartment and the selectivity filter; it contributes to the channel selectivity (Grabe, 2006) and must play an essential role in channel conductance. Perhaps surprisingly, the theoretical demonstration of the role of the structure of the cavity in determining the conductivity is still lacking.

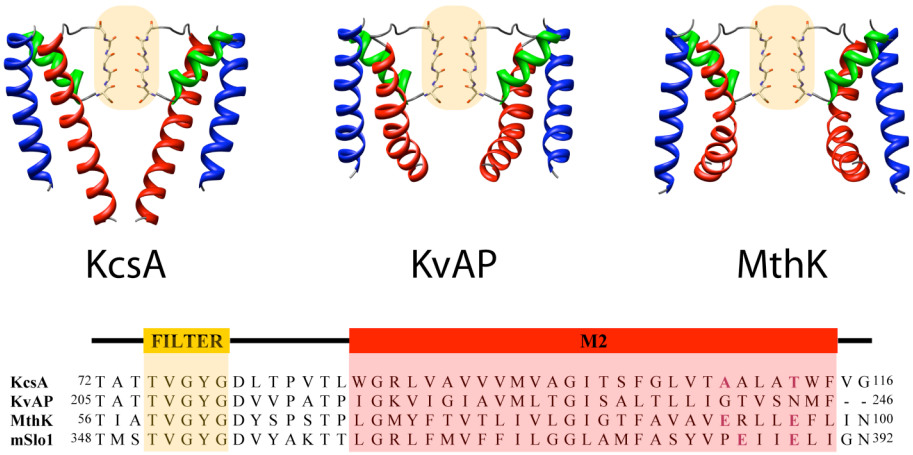

Figure 4-1 Channel models and aminoacid sequences.
The crystallographic structure of KcsA is shown, together with the structures of the KvAP- and MthK-based models. For the sake of clarity, only two of the four channel subunits are shown (M1 helixes in blue, M2 in red and P-loop in green). The aminoacid sequences of KcsA, KvAP, MthK and mSlo1 (BK potassium channel) are shown at the bottom. The aminoacid A108 and T112 in the KcsA sequence are highlighted in purple, as the negatively charged residues in the M2 helix of MthK and mSlo1.

The intracellular cavity differs in the structures available to date. The cavity is almost closed in the crystallographic structure of the KcsA channel because of the presence of a bundle between the M2 helixes. Indeed, KcsA was likely crystallized in the closed state and the M2 helixes were identified as the intracellular gate (Doyle, 1998). On the contrary, KvAP and MthK were crystallized in the open state (Jiang, 2002a; Jiang, 2003). Both the crystallographic structures of KvAP and MthK show a wider intracellular opening than KcsA owing to a movement of the M2 helixes (Jiang, 2002b; Perozo, 1999). The movement is more pronounced in MthK than in KvAP so that the intracellular cavity of the former is wider.

The influence of the intracellular gate opening on the electrostatic potential inside the cavity has been studied in KcsA by Poisson-Boltzmann theory (Jogini, 2005). A lumen similar to that of the experimental structure of KvAP was found optimal for conductance since it provides a flat energy

profile for the ion transport from the bulk solution to inside the cavity. The wider opening revealed in MthK hardly improves the probability of entrance inside the cavity of potassium. However, experimental data suggest a wider pore in the BK potassium channels, and a relation between the wider pore and the higher conductance was suggested (Brelidze, 2005).

Additionally to the amount of gate opening, the behaviour of ions in the cavity is affected by the charge distribution in the protein. Charges from the backbone and the sidechains may hinder or accelerate ion passage. Poisson-Boltzmann calculations revealed the important role of the backbone charges in the P-loop alpha helixes (Roux, 1999). In practice, the local atomic charges of the P-loop helix generate an electric dipole, which points toward the cavity and attracts potassium ions. Indeed, a potassium ion inside the cavity was experimentally revealed in the crystallographic structure of KcsA (Doyle, 1998). The P-loop backbone charges must therefore be important for the conduction mechanism, but this effect has not been quantified yet.

The role of the sidechain charges on the channel functioning has been experimentally investigated in several channel families (Chen, 2003; Fujiwara, 2006; Imoto, 1988; Li, 1999; Smith, 2001; Xu, 2006). Concerning potassium channels, it was found that negatively charged residues in the M2 helixes, which are highly conserved in BK potassium channels, are crucial for the high conductance phenotype (Brelidze, 2003; Nimigean, 2003). An increase in the potassium concentration inside the cavity was proposed as the mechanism by which negatively charged residues in M2 increase the conductance (Brelidze, 2003).

In this chapter, it is demonstrated that KcsA conductivity is highly sensitive to the presence of negative residues and that, for physiological concentrations of potassium, they cause an increase of its concentration inside the cavity. The potassium concentration inside the cavity emerges as a general driving force that regulates channel conductance. Electrostatic interactions lie at the core of this mechanism.

4.2 Methods

4.2.1 Channel Models

A model of KcsA in the closed state was defined according to its high-resolution crystallographic structure (1K4C (Zhou, 2001)), using the same procedure outlined in section 3.2.1.

The experimental structures of KvAP (pdb 1LNQ (Jiang, 2003)) and MthK (pdb 1ORQ (Jiang, 2002a)) were used as templates for the KcsA open state. The procedure used to define the open models of KcsA was slightly different from the procedure described in section 3.2.1. The aminoacid sequences of KcsA, KvAP and MthK were aligned using the T-Coffee software (Figure 4-1) (Notredame, 2000). Two models of KcsA in the open state were defined, moving the KcsA backbone atoms to the analogous atoms of KvAP and MthK. The crystallographic structures of KcsA, KvAP and MthK differ mainly in the M2 helixes, with minor differences located in the M1 helixes. Therefore, only the KcsA aminoacids from 28 to 51 and from 87 to 114 were displaced to open the channel. The resulting models have the backbone structure of KvAP and MthK, while the sidechains orientation of KcsA is preserved. In addition to the KvAP and MthK based models, a series of "in-between" models were defined, gradually shifting the channel structures one into another.

The KcsA models were used to analyze the role of the gate opening, without taking into account the possible biasing contribution of the aminoacid sequence. Since potassium ions enter the cavity in the hydrated form (Doyle, 1998), only channel models with an intracellular gate wider than a hydrated potassium ion (3.31 Å, corresponding to the first hydration shell (Volkov, 1997)) were considered. The narrowest channel model used here is referred to as KcsA-based model. The names KvAP-based model and MthK-based

model are adopted for the KcsA open structures modelled on KvAP and MthK (Figure 4-1).

To study the influence of the sidechain charges on the channel conductance, the models of three mutated channels were defined (A108E, T112E, and A108E/T112E). The sidechains of the mutated aminoacids were manually placed by the software DeepView, choosing a rotamer state having no steric clashes with the rest of the protein (Guex, 1997).

4.2.2 Numerical Solver

The PNP differential equation set was solved numerically (Furini, 2006) in a cylindrical grid. The grid axis was chosen as the channel axis to provide a more accurate discretization in this region, where the analysis is focused. The grid axis length was set to twice the channel length, and the grid radius 1.5 times the channel external radius. The number of grid points was: 140 along the axis (distance 0.05nm); 150 along the radial direction (distance 0.025nm) and 72 along the angular direction (distance 0.087rad). The iterative procedure used to solve the Poisson and the Nernst-Planck equations was stopped once the distance between consecutive solutions fell below 10^{-10}mV for electric potential and 10^{-10}mM for ion concentrations.

The relative dielectric constant was set to 2 in protein and 80 in water. A volume with low dielectric constant (ε = 2) was introduced around the channel, to mimic the presence of the lipid bilayer. The aromatic residues tyrosine 45 and tryptophan 113 were used to define the upper and lower boundary of the lipid bilayer. Diffusion coefficients were set to the experimental bulk values in water outside the channel (D_{K^+} = 1.96 × 10^{-9} m^2/s and D_{Cl^-} = 2.03 × 10^{-9} m^2/s (Lide, 2004)), and were reduced to 10% inside the channel. A reduction of diffusion coefficients to 10% was sufficient to fit the experimental currents as shown in Chapter 3, and in line with molecular dynamics simulations of narrow ion channels (Allen, 2000;

Mamonov, 2006). The radii and partial atomic charges of the protein atoms were set to the values proposed by Nina et al (Nina, 1997). The effect of their variation has been reported in Chapter 3.

4.3 Results

4.3.1 Intracellular Gate Opening

Perhaps counter-intuitively, when the mean radius of the intracellular cavity increases from 0.36nm to 0.63nm, the calculated conductance decreases by ~20%, regardless of the applied membrane potential (Figure 4-2). A mean radius of 0.63nm corresponds to the KvAP-based model. Further increase of the gate opening does not affect the channel conductance. The currents through the KvAP- and the MthK-based models differ less than 1%, in spite of an increase in the mean internal radius of ~30%. The conductance values for gate openings from the KvAP- to the MthK-based model are in good agreement with experimental data (77.3±0.8 pS versus 75.6±10 pS, with membrane potential set to 100 mV and ion concentrations set to 100 mM; 96.0±1.0 pA versus 95.6±11 pA, with membrane potential set to 25 mV and ion concentrations set to 100 mM (LeMasurier, 2001)).

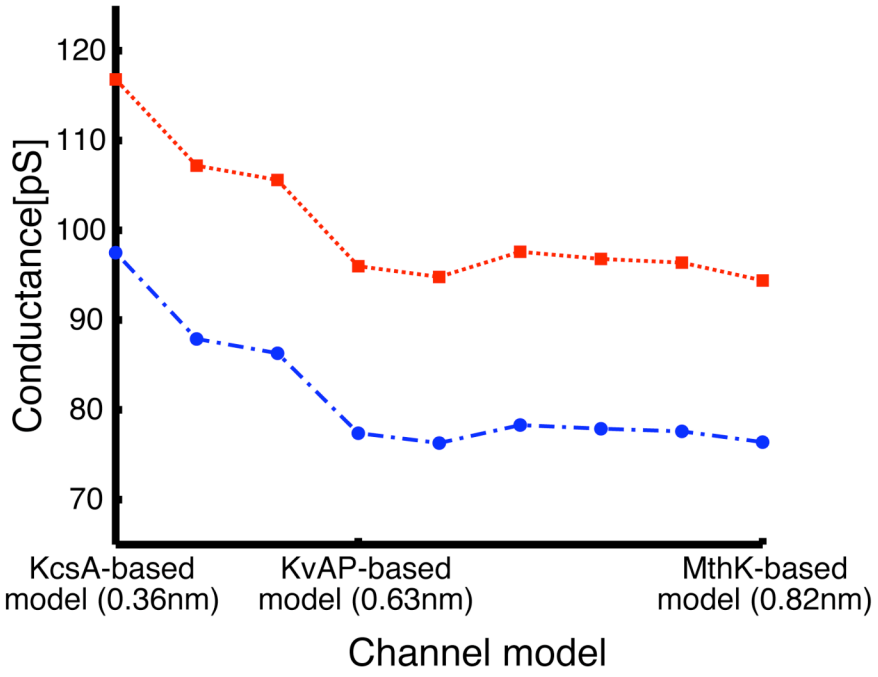

Figure 4-2 Channel conductance at different gate openings.
The blue dashed line (circular points) and the red dotted line (square points) show the channel conductance when the membrane potential is set to 100 mV and 25 mV respectively. The x-axis ranges from the KcsA-based model to the MthK-based model. Tics on the x-axis highlight the location of the KcsA-, KvAP- and MthK-based model. The mean radius of cavity in these structures is shown in the x-axis labels. Potassium and Chloride concentrations are set to 100 mM.

The gate opening affects the electric potential and the potassium concentration only inside the intracellular cavity (Figure 4-3). Electric potential and concentration are almost unchanged in the selectivity filter, in agreement with previous results by Monte Carlo free energy integration (Garofoli, 2003). The potential in the intracellular cavity is more positive in wider channels and, consistently, the potassium concentration is lower. Potassium concentration exhibits a peak below the selectivity filter (intracellular side). This peak is preserved in all the channel models, regardless of the opening extent (Figure 4-3). The position of this peak resembles the position of the potassium ion experimentally revealed in the

KcsA crystallographic structure (Doyle, 1998). The peak value decreases from 700 mM in the KcsA-based model, to 420 mM in the KvAP-based model (membrane potential set to 100 mV; ion concentrations set to 100 mM). Further channel openings cause a minor decrease in the potassium concentration peak.

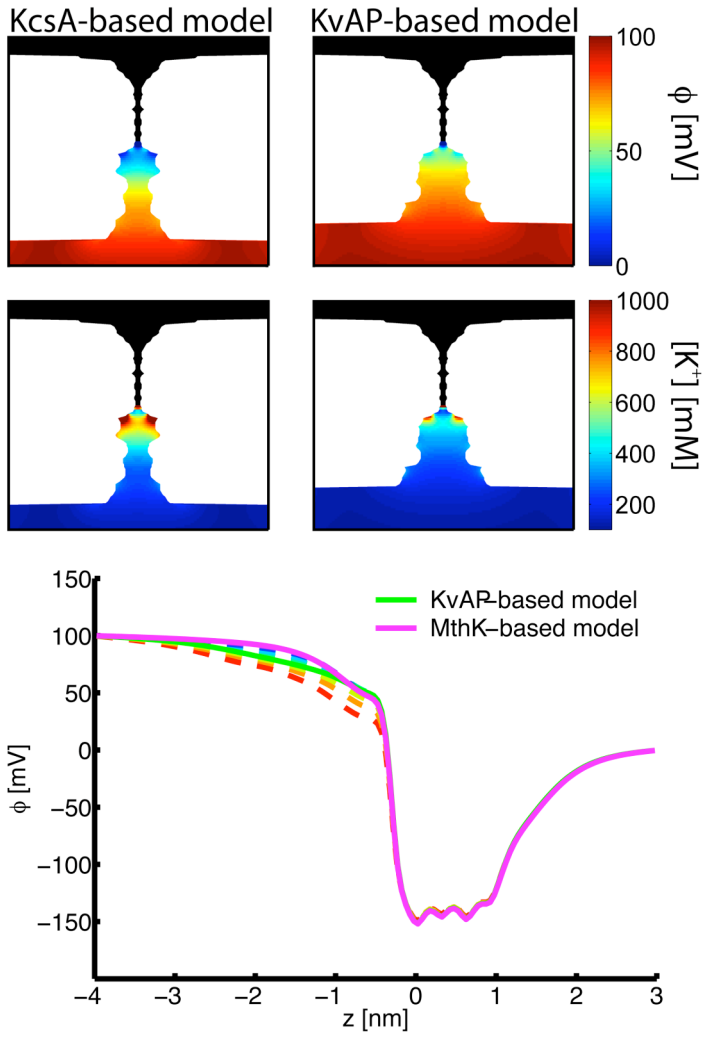

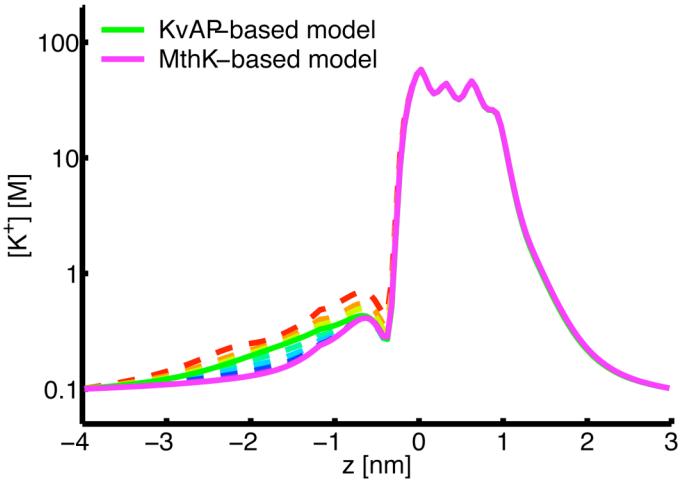

Figure 4-3 Gate opening: electric potential and K^+ concentration.
(Upper panels, previous page) Electric potential (ϕ) and potassium concentration ($[K^+]$) inside the KcsA- and the KvAP-based model. The colour-maps show the electric potential and the potassium concentration on a longitudinal section of the channel. In order to focus the colour-maps on the intracellular cavity, electric potential and the potassium concentrations in the selectivity filter and in the extracellular compartment are not shown. (Bottom plots) Electric potential (ϕ) and potassium concentration ($[K^+]$) along the channel axis. The z-axis extents from the intracellular to the extracellular compartment. A logarithmic scale is used for the potassium concentration. Different colours are used for different intracellular gate openings: KcsA-based model in red, colour spectrum from red to purple for wider gate openings. Continuous lines are used for the KvAP- and MthK-based model, dashed lines for the other structures. Membrane potential is set to 100 mV, and ion concentrations are set to 100 mM, both for the data in the colour-maps and in the plots.

The decrease in current, caused by the gate opening, is due to the presence of the P-loop backbone charges (see sub-section 4.3.2.1). These charges stabilize the presence of a potassium ion inside the cavity (Roux, 1999) with a non-trivial mechanism. Widening of the vestibule increases the volume accessible to water, that is the volume with a high dielectric constant. Increasing the volume with high dielectric constant increases the shielding of the P-loop backbone charges and reduces the attraction exerted by these charges on potassium ions. Indeed, according to Poisson-Boltzmann calculations, the stabilization energy provided by the charges of the P-loop

backbone on a potassium ion in the cavity is -27.5 Kcal/mol in the closed model of KcsA. This energy decreases to -7.0 Kcal/mol in a KcsA structure modelled on the KvAP experimental structure (Jogini, 2005).
The geometry of the intracellular cavity was probed experimentally with sugar molecules, and a wide cavity for the BK channels was suggested (Brelidze, 2005). This wider cavity has been associated to the high conductance phenotype of BK channels. Actually, according to our results, the wider cavity does not necessarily imply an increase of conductance.

4.3.2 Protein Charge Neutralization

4.3.2.1 P-loop Helixes

Neutralization of the partial atomic charges of the P-loop backbone atoms causes a sizable decrease of channel current (Table 4-1). The decrease is not related to the extent of the gate opening. Indeed, KcsA-, KvAP- and MthK-based models show almost the same current drop by nearly an order of magnitude. The electric potential inside the cavity turns from negative to positive, and the peak in the potassium concentration disappears (Figure 4-4). Importantly, potential and concentration in the selectivity filter do not change. The applied membrane potential does not affect the decrease in channel current. The percentage variation in the channel current ($\Delta I_{\%}$) almost does not change when the membrane potential ranges from -100 mV to +100 mV, as proved by the low standard deviation (Table 4-2). To further confirm the crucial role of the backbone charges, calculations were repeated removing the sidechain charges of the P-loop, and retaining the backbone charges. No sizable change in conductance, electric potential and potassium concentration was observed in these conditions (Table 4-1; Figure 4-4).

	KcsA-based Model		KvAP-based Model		MthK-based Model	
	I[pA]	**$\Delta I_{\%}$**	**I[pA]**	**$\Delta I_{\%}$**	**I[pA]**	**$\Delta I_{\%}$**
Wild-type channel No neutralized charge	9.75	-	7.74	-	7.64	-
P-loop backbone	1.11	-89%	1.09	-86%	1.09	-85%
P-loop sidechain	9.11	-7%	6.96	-10%	6.96	+9%
M1 backbone	10.28	+5%	8.31	+7%	7.70	+1%
M2 backbone	9.55	-2%	9.04	+17%	9.92	+30%
Mutation A108E	12.89	+32%	11.64	+50%	10.24	+34%
Mutation T112E	11.71	+20%	11.46	+48%	9.76	+28%
Mutations A108E/T112E	14.31	+46%	16.53	+114 %	12.87	+68%

Table 4-1 Computed channel currents with a membrane potential of 100 mV
Ionic currents (I) through three channel models are reported, together with data on charge neutralizations and aminoacid mutations. The percentage variation in the channel current ($\Delta I_{\%}$) refers to the current in the wild-type channel – same channel model - with no neutralized charge. Potassium and Chloride concentrations are set to 100 mM.

	$\Delta I_{\%}$		
	KcsA-based Model	**KvAP-based Model**	**MthK-based Model**
P-loop backbone	(-88.6±0.2)%	(-85.1±0.9)%	(-84.8±0.9)%
M2 backbone	(-3±1)%	(16.3±0.6)%	(29.6±0.4)%
Mutations A108E/T112E	(49±2)%	(113±1)%	(67.9±0.9)%

Table 4-2 Dependence of the current changes on the membrane potential
The percentage variation in the channel current ($\Delta I_{\%}$) refers to the wild-type channel – same channel model - with no neutralized charge. Currents were computed at different membrane potential, ranging from -100 mV to +100 mV with a 25 mV step. The mean percentage variation along this range of membrane potential is reported, together with the standard deviation. Potassium and Chloride concentrations are set to 100 mM.

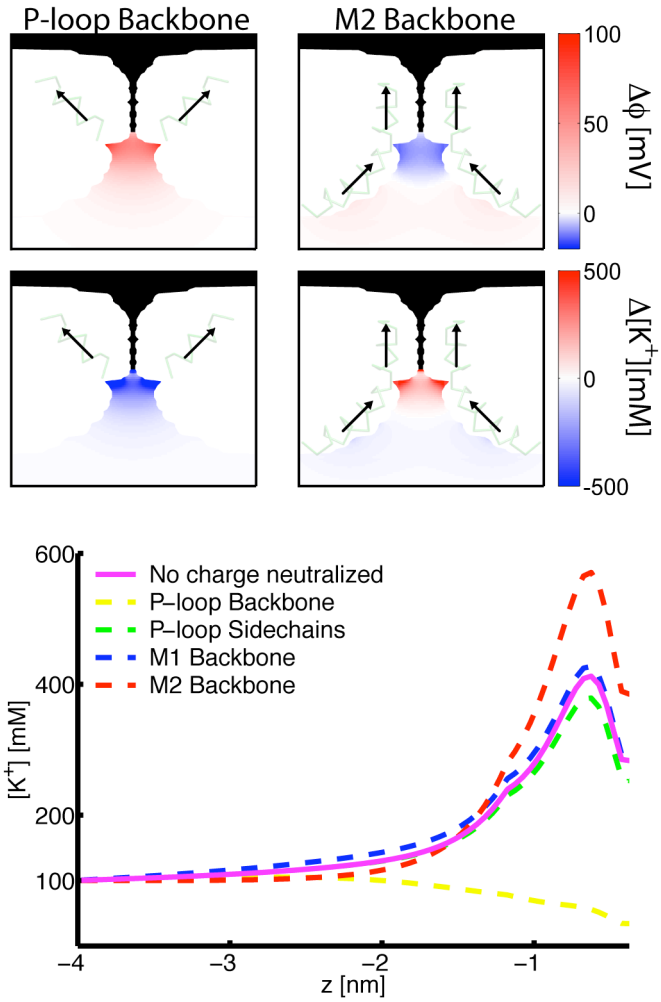

Figure 4-4 Protein charges neutralization: electric potential and K^+ concentration in the MthK-based model

(Upper panels) Changes in electric potential ($\Delta\phi$) and potassium concentration (Δ [K^+]) induced by the neutralization of the P-loop or M2 backbone charges in the MthK-based model. As in figure 3, a longitudinal section of the channel is shown and the colour-maps are focused on the intracellular cavity. P-loop and M2 helixes, together with dipole directions (from the negative to the positive pole), are shown. (Bottom plot) Potassium concentration ([K^+]) along the channel axis. The z-axis extents from the intracellular compartment to the bottom of the selectivity filter. Membrane potential is set to 100mV, and ion concentrations are set to 100mM, both for the data in the colour-maps and in the plot.

In a related system, Chatelain et al. (Chatelain, 2005) challenged the role of the electrical dipole generated by the P-loop backbone charges. They showed that the presence of a positive residue close to the P-loop C terminal of a mutated Kir2.1 channel does not change the conductance. This seems to suggest that the P-loop backbone dipole does not play a role in the conduction mechanism. However, comparison of the X-ray structures of KcsA (Doyle, 1998) and KirBac1.1 (Kuo, 2003) shows that P-loop backbone charges likely play a different role in inward rectifier channels. At odds with the present case, the P-loop helixes do not point towards the centre of the intracellular cavity and the sidechains are peripheral with respect to the alpha helix backbone so that the interplay of the backbone dipole, the atomic charges in the sidechains, and a potassium ion in the cavity could differ.

4.3.2.2 M1 and M2 Helixes

The backbone charges in the M1 helixes have no sizable effect on conductance, electric potential and ion concentrations (Table 4-1; Figure 4-4). M1 helixes are too far from the chamber to exert a Coulombic effect. On the contrary, a functional role of the M2 backbone charges emerges. Neutralization of the M2 backbone charges causes a sizable increase in the channel current and in the potassium concentration, both for the KvAP (+17%) and the MthK-based (+30%) models (Table 4-1; Figure 4-4). On the contrary, the neutralization of the M2 backbone charges does not affect the ion transport in the KcsA-based model (Table 4-1). These results are not affected by the applied membrane potential (Table 4-2).

In the closed state, M2 helixes have a straight axis and effectively generate a single electric dipole. The channel opening is achieved by bending the M2 helixes at a hinge glycine (Gly99 in KcsA). Once the M2 helixes are bent, they do not generate a single electric dipole. Each M2 helix is actually split in two helixes: one extending from the N-terminal of M2 to the hinge

glycine, and one extending form the hinge glycine to the C-terminal of M2. As a consequence, the electric dipole of M2 splits into two components: one associated to the N-terminal helix (~30Debye) and one to the C-terminal helix (~35Debye). The negative pole of the dipole associated to the N-terminal helix is close to the channel cavity, while the dipole associated to the C-terminal helix has the positive pole close to the cavity. Consequently, while the former stabilize an ion in the cavity, the latter destabilize it (Figure 4-4). The interference of the two effects almost balances for structures narrower than the KvAP-based model. When the M2 helixes are shifted, as in the crystallographic structure of MthK, the destabilizing dipole dominates. This destabilizing effect counterbalances the decrease of electrical resistance, and consequently the conductance does not vary going from the KvAP- to the MthK-based model. Both the M2 dipoles do not point towards the cavity centre and they are not as important as the P-loop dipole for the channel functioning.

4.3.2.3 Aminoacid Mutations

The mutation of aminoacids Ala108 or Thr112 to glutamate increases the channel current (Table 4-1). A rather similar current increase is present in all channel models for the two mutations. Mutating both the residues to glutamate further increases the current (Table 4-1). The highest increase is observed in the KvAP-based model (+114%), while a slightly smaller increase appears in the KcsA- and MthK-based models (+46% and +68%). The current increase is not affected by the applied membrane potential (Table 4-2). Potassium concentration inside the cavity increases in the channel as a consequence of the mutations (Figure 4-5). The concentration peak below the selectivity filter almost doubles in the channel with the mutations A108/ET112E (Figure 4-5).

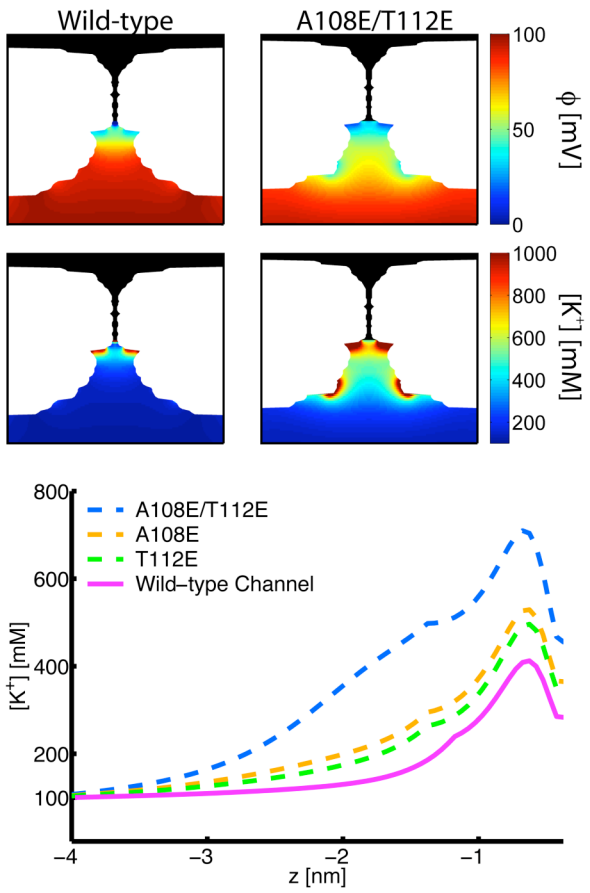

Figure 4-5 Aminoacid mutations: electric potential and K^+ concentration in the MthK-based model.
(Upper panels) Electric potential (ϕ) and potassium concentration ($[K^+]$) in the MthK-based model, wild-type or with the A108E/T112E mutations. As in figure 3, a longitudinal section of the channel is shown and the colour-maps are focused on the intracellular cavity. (Bottom plot) Potassium concentration ($[K^+]$) along the channel axis. The z-axis extents from the intracellular compartment to the bottom of the selectivity filter. Membrane potential is set to 100 mV, and ion concentrations are set to 100 mM, both for the data in the colour-maps and in the plot

Nimigean et al. measured a considerable increase in the channel current when Ala108 of KcsA (located facing the cavity) was mutated to aspartate (Nimigean, 2003). Similarly, Brelidze et al. observed a two-fold decrease of the conductance in the mSlo1 channel, when both glutamate residues of M2 were mutated to asparagines (Brelidze, 2003). We found a two-fold increase

of current when two negatively charged residues were introduced in M2 (+113% in the MthK-based model). Brelidze et al. also found experimentally that an increase of the bulk concentration of potassium from 150 mM to 500 mM has the same effect of the presence of two negatively charged residues. In accordance with these experimental data, we revealed the same current in the wild-type channel with potassium bulk concentration set to 500 mM and in the double mutated channel with potassium bulk concentration set to 100 mM.

To analyze the relationship between potassium concentration inside the cavity and conductance, the current through the doubly mutated channel was compared to the current through the wild-type channel at different potassium concentrations (Figure 4-6). At 20 mM the current of the mutated channel is more than double the current of the wild-type channel. At 1.6 M the two channels produce almost the same current. The result agrees with the hypothesis that the conductance increase in the mutated channel is related to the higher potassium concentration inside the cavity. At low bulk concentration, an efficient way to attract potassium ions in the cavity is extremely important to preserve a high conductance value. The negatively charged residues of the mutated channel attract potassium ions in the cavity more efficiently than the wild-type channel. When the bulk concentration is large, the attraction of potassium ions inside the cavity becomes marginal and the difference between mutated and wild-type channels decrease.

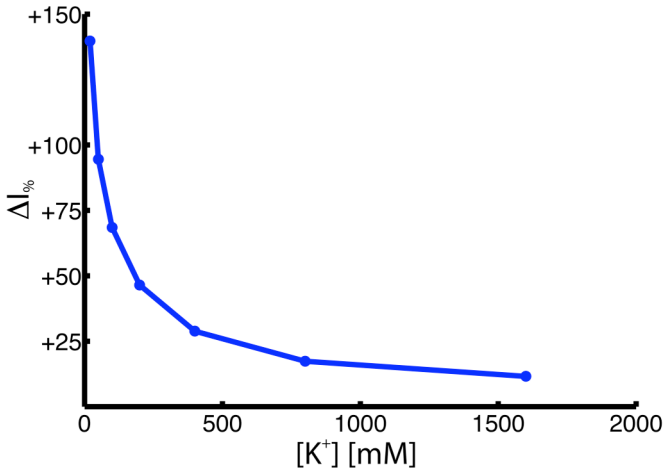

Figure 4-6 Current increase in the A108E/T112E mutated channel at different bulk concentrations of K+
Data on the MthK-based model with the A108E/T112E mutations are shown. The percentage variation in channel current ($\Delta I_{\%}$) refers to the wild-type MthK-based model at the same ion concentration. Membrane potential is set to 100 mV.

4.3.3 Potassium Concentration in the Cavity as a Conductance Determinant

Analysis of the potassium concentration in the intracellular cavity reveals a relation between the concentration peak and the channel conductance. In Figure 4-7 the current through the channel is shown as a function of the maximum potassium concentration inside the cavity (measured along the channel axis). Figure 4-7 includes data from all the different channel models, atomic charge neutralizations, aminoacid mutations, and applied membrane potentials discussed in the previous sections. Data were fitted by a line, in a least square approach. The cross-correlation index between concentration and current is 0.96, and the root mean square distance of the computed currents from the interpolating line is 1.2 pA. The sensitivity of the conductance to the potassium concentration inside the cavity is 12.5 pA/M.

An important conclusion emerges: there is a strict relationship between channel conductance and potassium concentration in the KcsA cavity.

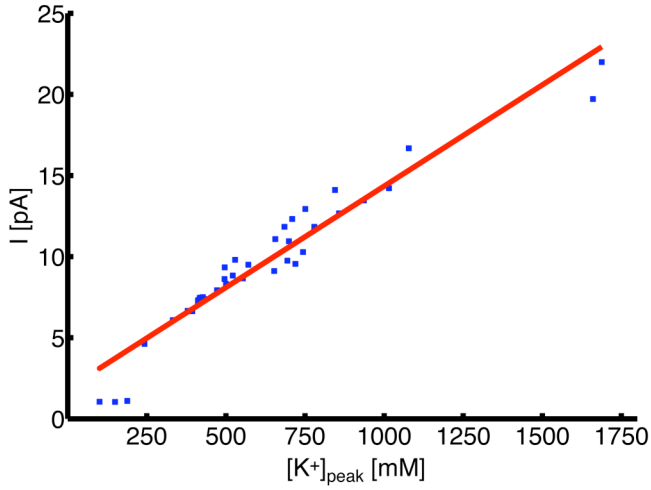

Figure 4-7 Correlation between Potassium concentration in cavity and channel current
Data of different channel models, charge neutralization schemes, aminoacid mutations, and membrane potentials are shown. A square dot is used for the computed currents, a continuous line for the interpolating line.

4.4 Discussion

Electro-diffusion theory is able to simulate accurately a large number of experimental data in ion channels (Nonner, 1999). Once tuned to account for the confinement effects that must be present in the potassium channels (Corry, 2000), PNP theory reproduces quantitatively the ionic currents and explains the high probability to observe the presence of a K^+ ion below the selectivity filter (intracellular side) in the static picture offered by X-ray crystallography (Furini, 2006). The variability of the channel conductance with amino-acid mutations and the role of the protein in the wider region outside the selectivity filter belong by right to the area of applicability of continuum electro-diffusion theory, because this is the region where confinement effects are less marked. In this context, the use of simplified

theories, as other recently reported cases of investigation of selectivity (Boda, 2007; Bostick, 2007) or in the study of diffusion through membranes (Shaw, 2007), allows one to remove unwanted details and highlights the basic principle governing the channel functioning.

The major issues addressed in this chapter are the functional activity of the P-loop backbone of the proteins, the similar functional activity of the local charges in the M1 and M2 helixes, and that of mutated negatively-charged residues in the inner helixes. The role of the charges of all these moieties is ultimately to modify the potassium ions concentration in the intracellular cavity, and by this the channel conductance. Channel conductance and potassium concentration are instead not affected by changes in the cavity size, once the intracellular gate is wider than in the KvAP experimental structure. In the PNP theory electrostatic interactions are the only driving forces acting on ions. Thus, the present analysis shows that the details and the variation of the mechanism of potassium transport are governed by electrostatic interactions.

A correlation between potassium concentration in the intracellular cavity and channel conductance emerged as a propriety of the KcsA channel. Potassium concentration and electric potential in the channel cavity are the driving forces acting on the ions in the selectivity filter. The intracellular vestibule may modulate these driving forces, and consequently the channel conductance. Despite all the numerical simulations refer to the KcsA channel, we are prone to suggest the concentration-conductance correlation as a general propriety of potassium channels. The hypothesis is supported by the structural conservation of the selectivity filter in the potassium channel family. Structural changes in the intracellular vestibule, like single residue mutations, are not likely to affect the selectivity filter. The filter may be regarded as a functional unit conserved among different potassium channels. In this context the intracellular vestibule, like other channel moieties, defines the boundaries conditions perceived by the selectivity filter, i.e. the ion

concentrations and the electric potential. The intracellular cavity couple the selectivity filter to the intracellular compartment, and it may play a pivotal role on the conductivity of potassium channels.

Chapter 5

Molecular Determinants of Blockage in hEag1 K^+ Channels

The voltage-gated potassium channel hEag1 was detected in tumor cells of diverse origin. The antihistamine drug astemizole and the antidepressant drug imipramine reduce cancer cell proliferation, apparently through inhibition of the hEag1 current. The structural determinants required for hEag1 blocking by these (and other) drugs were probed by mutating a residue at the C-terminal end of the S6 helix (inner helix), and also by generating mutant channels showing C-type inactivation. Introducing C-type inactivation decreased the affinity and slowed the block recovery caused by astemizole and dofetilide – an antiarrhythmic drug – but not imipramine, indicating that these drugs bind different sites. Mutation of the residue Phe468 in hEag1 increased the affinity for astemizole and imipramine, but only slightly that of dofetilide. Moreover dofetilide is not trapped by hEag1, in contrast to hErg (a closely related potassium channel) suggesting that structural differences exist between these channels. Atomic models of hEag1 and hErg were defined by homology modeling. Afterwards, a docking procedure was used to identify the binding sites for astemizole, imipramine and dofetilide in these channel models. The experimental data presented in this chapter are from the research group headed by Prof. Luis A. Pardo at the Max Planck Institute for Experimental Medicine (Goettingen, Germany).

Most of the content of this chapter has been published in: D. Gómez-Varela, C. Contreras-Jurado, S. Furini, R. García-Ferreiro, W. Stühmer, L. Pardo, "Different relevance of inactivation and F468 residue in the mechanisms of hEag1 channel blockage by astemizole, imipramine and Dofetilide". FEBS Lett, 580(21):5059-66, 2006

5.1 Introduction

The voltage-gated potassium channel Eag1 is mainly expressed in the central nervous system. Outside the central nervous system Eag1 shows an unparalleled specificity for tumor tissue (Gavrilova-Ruch, 2002; Ludwig, 1994), and its inhibition using the antihistamine astemizole (Ouadid-Ahidouch, 2001) or the tricyclic antidepressant imipramine (Gavrilova-Ruch, 2002) reduces proliferation of tumor cells. As a consequence, Eag1 is a potential target for the development of novel therapeutic approaches in oncology. The usage of hEag1 blockers in anticancer therapy is hampered by side effects on a closely related potassium channel, named hErg. hErg is expressed in different tissues, but mainly in the hearth where it is responsible for the repolarizing I_{Kr} current, required for cardiac action potential repolarization (Sanguinetti, 1995). Unfortunately, all known hEag1 blockers (including imipramine and astemizole, (Suessbrich, 1996), (Zhou, 1999),(Teschemacher, 1999)) also inhibit hErg, which represents a serious difficulty both for research purposes (due to a lack of specific inhibitors to dissect the functions of hEag1) and from a clinical point of view (because of the potential hErg-dependent cardiac complications of an hEag1-based treatment). The synthesis of a potent and specific hEag1 blocker will need to exploit structural differences in the blocking process between these channels. Additionally, lessons learned from the differences in the blockage mechanisms of hEag1 and hErg may suggest strategies by which hErg inhibition can be avoided in general, thereby minimizing the cardiac complications of many drugs.

Previous studies clarified some of the biophysical details of the blocking mechanism of hEag1 channels by astemizole and imipramine (Garcia-Ferreiro, 2004). Both drugs are open channel blockers and although their binding sites seem to overlap, their mechanism of action is probably

different. However, the structural determinants important for the binding underlying these differences are still unknown.

Amino acid residues located at the base of the pore helix and along the S6 segment are predicted to face toward the central cavity of potassium channels, and are very important for the block of potassium channels by different compounds (Decher, 2004). A second class of aminoacids important for the blockage of hEag1 and hErg are the residues involved in C-type inactivation (Mitcheson, 2000a). Inactivation of a voltage-gated channel is the reduction of the channel current, even though the activating voltage is maintained. Different region of the channel may contribute to the inactivation processes, thus different inactivation modality were defined. C-type inactivation is an inactivation processes related to structural changes at the extracellular side of the channel (Baukrowitz, 1995). Recent experimental data pointed out that structural changes at selectivity filter are likely the cause of C-type inactivation (Cordero-Morales, 2006). In hErg channels an intact C-type inactivation is crucial for the high-affinity binding of diverse drugs (Ficker, 1998; Herzberg, 1998; Lees-Miller, 2000; Wang, 1997). Similarly, introduction of C-type inactivation in a non-inactivating bovine Eag channel (bEag) by mutations at positions T432 and A443, both located in the pore region, increased the bEag affinity for Dofetilide (Ficker, 2001). Two residues at the C-terminal end of the S6 helix of hErg (Y652 and F656) are also crucial for the blockage by several compounds, (Sanchez-Chapula, 2002), (Kamiya, 2001). However, the importance of analogous residues located at the carboxyl end of the S6 helix of hEag1 remains to be determined.

In the study presented in this chapter, it is examined how the introduction of C-type inactivation into hEag1 (by targeting the pore residues T432 and A443), and how the aminoacid F468 affect the blockage by astemizole, imipramine and dofetilide. Clear differences emerged in how the effects of the drugs are altered, suggesting that at the molecular level the blocking

mechanism for hErg and hEag1 is distinct. Finally, to extract structural information from these experimental findings *in silico* molecular modeling, based on the crystal structure of the open mammalian Kv1.2 channel (Long, 2005), was performed using hEag1 and hErg homology models. The results from the modeling are in good agreement with the experimental observations. The major conclusions are that i) depending on the blocker, different residues in hEag1 channel are required for blocking, and ii) that structural differences between hEag1 and hErg exist that could be exploited in the rational design of specific compounds to specifically block hEag1, but not hErg channels. Such compounds would facilitate the study of Eag1 function in different tissues and could provide information as to how to eliminate the undesirable hErg blockage characteristic of many drugs.

5.2 Materials and Methods

5.2.1.1 *Molecular Biology.*

Mutations were introduced into the pSGEM-hEag1 (Pardo, 1999) using the QuikChange XL site-directed mutagenesis kit (Stratagene). All constructs were thereafter sequenced in full. The forward primer used to generate hEag1F468C was (5'-3'; the reverse primer had the complementary sequence):TATGCCACCATCTGCGGGAATGTGACG.
hEag1T432S/A443S was constructed sequentially (first T432S and then A443S). The forward oligonucleotides used were: TCTCCTCGTTGTATTTCACAATGTCCAGCCTCACC (T432S) and TGGGAACATCTCCCCATCCACAGACATTG (A443S). Oocyte preparation and electrophysiological recordings were performed as described elsewhere (Stuhmer, 1992).

5.2.1.2 *Data Analysis.*

Curve-fittings were performed using Igor Pro (WaveMetrics). IC_{50} values (drug concentration that blocks half of the current) and Hill coefficients (h) were obtained through fittings to the Hill equation. Deactivation kinetics was determined by exponential fitting. Data are represented as mean ± s.e.m., where n=number of oocytes. Statistical significance was considered at $p<0.01$ in two-tailed *t* test.

5.2.1.3 *Drugs.*

Astemizole, N-methyl-astemizole, dofetilide and MK-499, were diluted from a DMSO stock solution. The final concentration of DMSO was always 0.1%, a concentration that showed no effects on hEag1 currents (data not shown). Imipramine was used from stocks in distilled water. Astemizole and imipramine were purchased from Sigma. Pfizer and Merck and Co. kindly supplied Dofetilide and MK-499, respectively.

5.2.1.4 Molecular Modeling

Structural models of hEag1 and hErg were built by homology modelling (see section 2.5). The Kv1.2 Protein Data Bank entry 2A79 (Long, 2005) was used as a template for the open state. Proteins were aligned with the program T-Coffee (Table 5-1) (Notredame, 2000). The amino acid sequence of the pore helix and S6 is highly conserved among these three channels, which should facilitate homology modeling of the channels' inner vestibule. Aligned sequences were submitted to SWISS-MODEL (Schwede, 2003) to obtain the protein structures. These structures were replicated in four identical units, symmetrically placed around the pore axis to build the tetrameric channels. Finally, channel molecules were energy minimized by 500 steps of steepest descent, using AMBER (Case, 2004). Since energy

minimizations were performed in the absence of solvent and lipid bilayer, the protein backbone was restrained with a force constant of 7 Kcal $mol^{-1}Å^{-2}$. Imipramine, astemizole and dofetilide were modeled in the protonated state. Partial atomic charges of all the drugs were parameterized by the ANTECHAMBER module of AMBER. Protein atomic charges were defined according to the AMBER99 force field.

The docking procedure (see section 2.3) was performed using the AUTODOCK 3.0 software (Garret, 1998). AUTODOCK performs the automated docking of a flexible ligand in a rigid receptor, minimizing an empirical energy function on a 3D grid. All bound angles in the ligands were free to rotate. The grid was defined to cover the whole internal vestibule of the channels and the energy was minimized by the Lamarckian genetic algorithm. In order to achieve a broad statistical analysis, every binding position search was carried out by 150 docking runs (Hetenyi, 2002). The results were clustered according to the root mean square distance (RMSD). Binding positions with a RMSD lower than 2 Å were placed in the same cluster (Hetenyi, 2002). The binding position with the lowest energy in the group of most populated cluster was selected for the $R_{closest}$ analysis.

	Pore Helix	Filter		Inner Helix
hEag1	YISSLYFTMTST	SVGFG	NIAPSTI	EKIFAVAIMMIGSLLYATIFGV
Herg1	YVTALYFTFSST	SVGFG	NVSPNTS	EKIFSICVMLIGSLMYASIFGV
Kv1.2	IPDAFWWAVVST	TVGYG	DMVPTTG	GKIVGSLCAIAGVLTIALPVPI

Table 5-1 Alignement of hEag1, hErg1 and Kv1.2 channels from the pore helix region to the final residue of the S6 segment

5.3 Results

5.3.1 Charged Astemizole – hEag1 Channels

Previous research showed that N-methyl-imipramine, a permanently charged form of imipramine, blocks hEag1 channels from the intracellular side as it was able to inhibit the current when applied to the bathing solution of inside-out patches, but not that of outside-out patches (Garcia-Ferreiro, 2004).
Astemizole however blocks a significant amount of the hEag1 current when applied to such patches in the outside-out configuration. Although the kinetics of this blockage seem to correspond to those of drug equilibration across the membrane (Garcia-Ferreiro, 2004), the existence of a binding site on the extracellular side of the hEag1 channel protein could not be excluded.
To obtain clearer evidence for an intracellular blockage of hEag1 by astemizole, we used the permanently charged, quaternary derivative of this drug (N-methyl-astemizole, NMA). Application of NMA (100 μM) to the bathing solution of oocytes under two-electrode voltage clamp reduced current amplitudes by approximately 20 %, therefore with an IC_{50} larger than 100 μM (inset Figure 5-1). Using the same oocyte, 10 μM astemizole (AST), in contrast, blocked approximately 90 % of the current (Figure 5-1).
The lack of a NMA effect when added to the oocyte bathing solution is not due to loss of affinity for hEag1, because NMA is able to reduce the current amplitude when applied to the intracellular side of inside-out patches in a time period with no significant rundown of hEag1 currents in the patches. Addition of 100 nM NMA to inside-out patches led to a virtual abolition of the hEag1 current (Figure 5-2A, *left traces*); under these conditions, the IC_{50} for this NMA effect was 30 nM i.e. three times smaller than the IC_{50} for AST in the same situation (91 nm, Figure 5-2B).

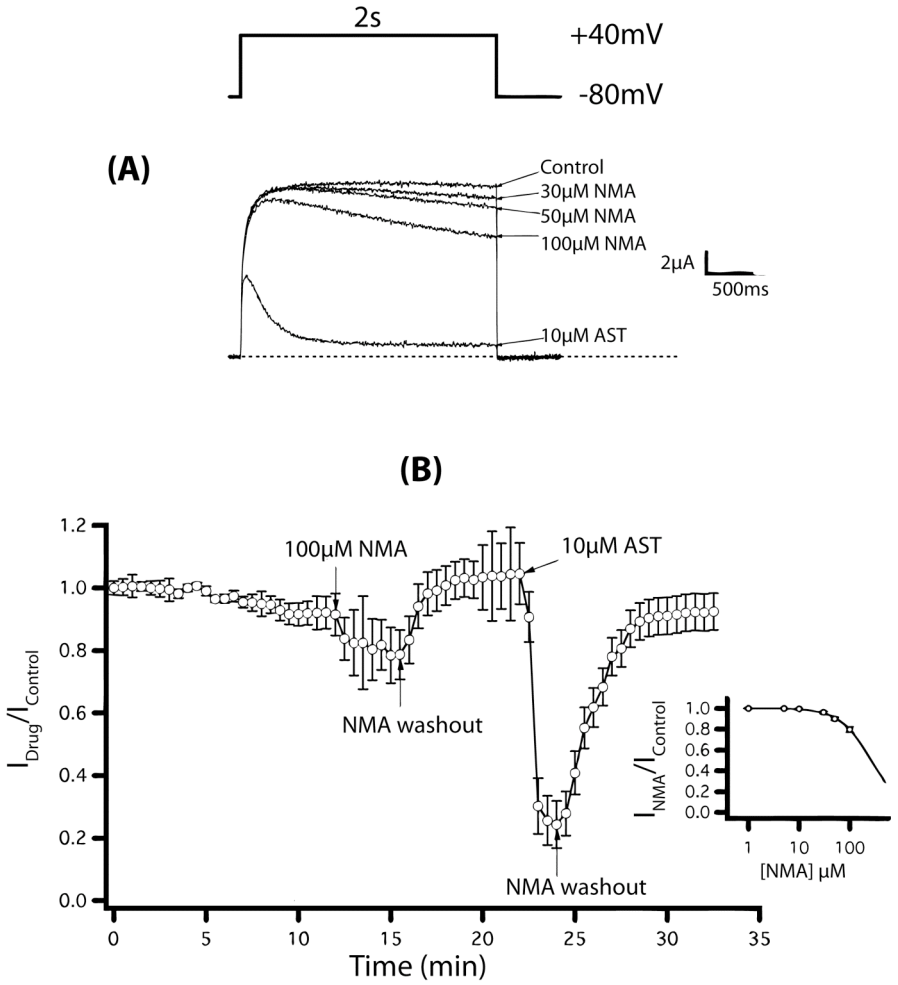

Figure 5-1 Lack of inhibition of hEag1 currents expressed in *Xenopus oocytes* by NMA.

(A) hEag1 currents in the presence of increasing concentrations of NMA and 10 μM AST. Traces elicited by test pulses applied every 20 s, from a holding potential of -80 mV to +40 mV for 2 s and return to -80 mV. The *dashed line* indicates the zero current level. (B) Time course of normalizing current amplitude (n=4) in the presence of the NMA concentrations indicated in A (for clarity we indicated only the addition of 100 μM NMA), after the NMA washout (NMA Washout), in the presence of 10 μM AST and after the AST washout (AST Washout). Currents were measurement at the end of the pulse at +40 mV and were normalized to the amplitude of the current before the addition of the NMA (Control in A). *Inset*, NMA dose-response curves of normalized mean data (n=10) obtained using the same protocol as described in A. Additionally the Hill fit according to the Hill equation described in the *Material and Methods* is shown. The respective Hill coefficients were 262.5 and 1.4.

It is formerly possible that AST acts both extra- and intra-cellulary at two independent binding sites, and that NMA has lost the affinity for the extracellular site. This explanation however does not agree with previous data on blockage by AST (Garcia-Ferreiro, 2004). Based on these previous studies, our interpretation of the data is that both AST and NMA block the channel from the intracellular side and that the charged form of AST (and therefore NMA) blocks more effectively (Garcia-Ferreiro, 2004).

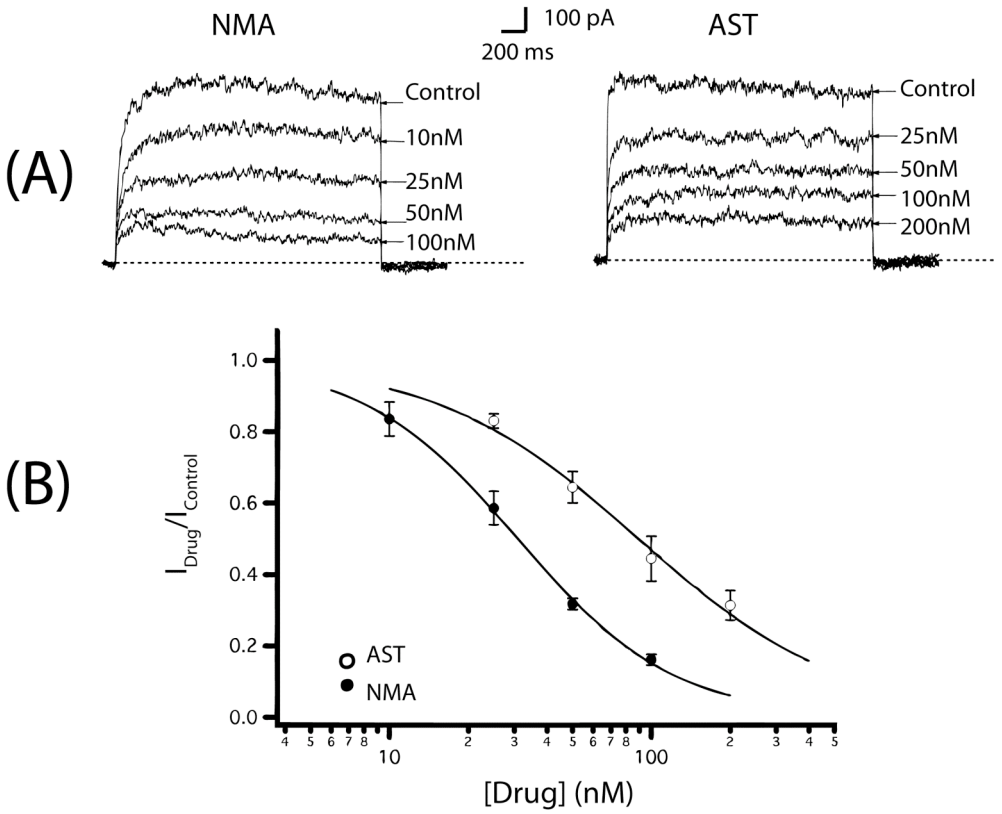

Figure 5-2 Blocking of hEag1 currents in inside-out patches of *Xenopus oocytes* by AST and NMA

(A) hEag1 currents in inside-out patches in the presence of increasing concentrations of NMA and AST. Traces elicited by test pulses applied every 20 s, from a holding potential of -80 mV to +40 mV for 2 s and return to -80 mV. The *dashed line* indicates the zero current level. (B) Dose-response curves of normalized mean data (n=4-6) obtained using the same protocol described in A. Currents were normalized to the amplitude of the current elicited at the end of the pulse at +40 mV before the addition of the drugs (Control in A). Additionally the

Hill fit according to the Hill equation described in the *Material and Methods* is shown. Respective Hill coefficients were 30.91 and 1.46 for NMA, and 89.42 and 1.11 for AST.

5.3.2 Astemizole - Mutations T432S/A443S and F468C

Although not always necessary for the blockage of hErg by drugs (Mitcheson, 2000a), intact C-type inactivation in hErg channels seems to be an important requisite for the high-affinity block by methanesulfonanilides (Ficker, 1998). Similarly, introduction of C-type inactivation into bovine Eag channels by a double mutation (T432S/A443S**)** increases the potency of blockage by Dofetilide (Ficker, 2001). We tested if introduction of C-type inactivation had any effect in AST blockage using hEag1 T432S/A443S. Analogously to the data reported for bovine Eag1 (Ficker, 2001), these mutations in the context of hEag1 produce C-type inactivation, as shown in Figure 5-3 (T432S/A443S *traces*). Although the most evident, the appearance of inactivation is not the only kinetic parameter altered by the double mutation. The deactivation of the mutant channel is slowed at all voltages between -70 and -140 mV, and the voltage-dependence of the activation process is shifted (the mutant starts to activate 10-15 mV more negatively than the wild type). The possible importance of these kinetic alterations in the blocking process will be discussed below.

We next determined the IC_{50} values obtained for AST with hEag1 and hEag1 T432S/A443S and found that the double mutation increased the affinity of AST for the channel (Figure 5-3). To determine the IC_{50} values, a steady state blockage was first achieved for each AST concentration (which requires 2-3 minutes), prior to measuring the current at the end of a 2 second +40 mV depolarization. In this way, we showed that AST has an IC_{50} of 2.82 μM for hEag1 WT (n=10, Figure 5-3B). To determine the IC_{50} of AST for hEag1 T432S/A443S, we applied the same pulse protocol as above, but rather than measuring the currents at the end of the pulse (due to the

inactivation), this was performed in the peak at +40 mV. This was possible because AST did not affect the activation or inactivation kinetics of the mutant channel under these conditions (data not shown). Using this strategy, the IC_{50} of AST for hEag1 T432S/A443S was determined to be 1.19 μM (n=8; Figure 5-3B).

In conclusion, as reported for the effect of dofetilide on bovine Eag channels (Ficker, 2001), the introduction of C-type inactivation into the hEag1 channel increases the potency of blocking by AST.

It is well documented that amino acid residues located in the C-terminal end of the S6 segment are important for the blockage of potassium channels by different compounds (Decher, 2004). Phe at position 656 in hErg channels is crucial for the binding of AST (Ficker, 2002) and other open channel blockers. To test the involvement of the corresponding residue for the AST-mediated block of hEag1, we mutated the analogous aromatic residue (F468C) and studied its effect on this process.

The current amplitudes obtained after expression of this mutant were greatly reduced when compared with wild type channels. However, the poor functional expression of the mutant channel compromised its kinetic characterization and we did not detect significant differences in either the activation or the deactivation process. We cannot though discard the possibility that the channel's kinetics has been altered, which is a documented consequence of a mutation in the equivalent hErg channel residue (Fernandez, 2004).

A higher AST concentration was required to reduce the current amplitude by 50% in the mutant channel when compared to wild type hEag1 (Figure 5-3A, F468C *traces*). We determined an IC_{50} of 49.8 μM (n=7), approximately 20 times higher than the IC_{50} for wild type channels. Steady state blockage was reached in 3-4 minutes when using the same pulse protocol as that described above for hEag1 WT.

This result strongly suggests that F468, putatively located at the entrance of the internal vestibule of hEag1, plays a crucial role in the blocking of these channels by AST.

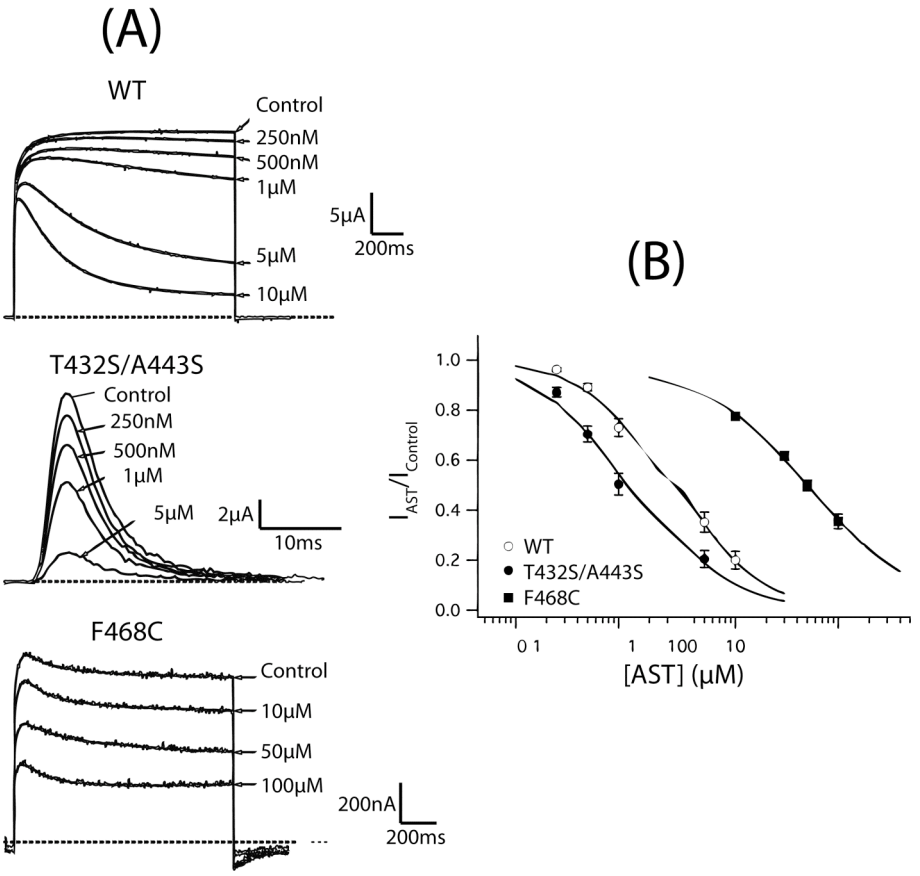

Figure 5-3 Concentration-dependent block of hEag1 WT, T432S/A443S and F468C by AST

(A) hEag1 currents after the steady-state blockage with the concentrations of AST indicated for WT (*upper traces*), T432S/A443S (*middle traces*) and F468C (*lower traces*). Traces elicited by test pulses applied every 20 s, from a holding potential of -80 mV to +40 mV for 2 s and return to -80 mV. The *dashed line* indicates the zero current level. (B) Dose-response curves of normalized mean data (n=7-10) obtained using the same protocol as described in A. Currents were measured at the end of the pulse at +40 mV in WT (open circles) and F468C (closed squares) and at the peak at +40 mV for T432S/A443S (closed circles). Currents were normalized to the amplitude of the current prior to the addition of the drugs (Control in A). Additionally the Hill fit according to the Hill equation described in the *Material and Methods*

is shown. The respective Hill coefficients were 2.82 and 1.11 for WT, 1.19 and 1.01 for T432S/A443S, and 49.82 and 0.81 for F468C.

5.3.3 Imipramine - Mutations T432S/A443S and F468C

AST and IMI competitively inhibit hEag1 channels, suggesting that both drugs have an overlapping intracellular binding site. However, the different affinity and altered voltage dependence of blockage (Garcia-Ferreiro, 2004) suggests that the overlap is not perfect, and the binding sites are subtly different.

We studied how the various mutations reported here affect the IMI blockage and measured the IC_{50} values of IMI for hEag1, hEag1 T432S/A443S and hEag1 F468C channels. Figure 5-4A shows representative traces recorded using the same protocol as described above in Figure 5-3. Measuring the current at the end of the +40 mV pulse, the IC_{50} of IMI for hEag1 WT channels was 40.2 μM (n=10, Fig. 4B). This value is 10 times higher than that for AST, in good agreement with the differences determined previously in hEag1 expressing HEK293 cells (Garcia-Ferreiro, 2004). We also observed a rising phase in the first milliseconds of the wild type hEag1 current traces at intermediate IMI concentrations (30 and 50μM, Figure 5-4A) that may represent equilibration between the association and dissociation processes prior to the establishment of the steady state block (Garcia-Ferreiro, 2004).

To study the effects of IMI on hEag1 T432S/A443S (Figure 5-4A), we applied the same pulse protocol as for AST, because IMI did not change the activation and inactivation kinetics of this mutant channel (data not shown). The IC_{50} of IMI for hEag1 T432S/A443S was 71.5 μM (n=8, Fig. 4B). Therefore the introduction of C-type inactivation in hEag1 did not reduce the IC_{50} of IMI, but instead increased it. Therefore, the introduction of inactivation affects IMI- and AST-mediated blocking of hEag1 channels differently, suggesting that a distinct binding site exists for each drug.

We also studied the blockage of hEag1 F468C by IMI. Using the pulse protocol described above, a steady state block was attained at all drug concentrations. The highest concentration tested (100 μM) was unable to block more than 30% of the current (Figure 5-4A). We did not analyze the effect of IMI concentrations greater than 100 μM and so did not determine a more accurate IC_{50}. However, as the IC_{50} is higher than 100 μM, this mutated channel has lost its sensitivity to IMI.

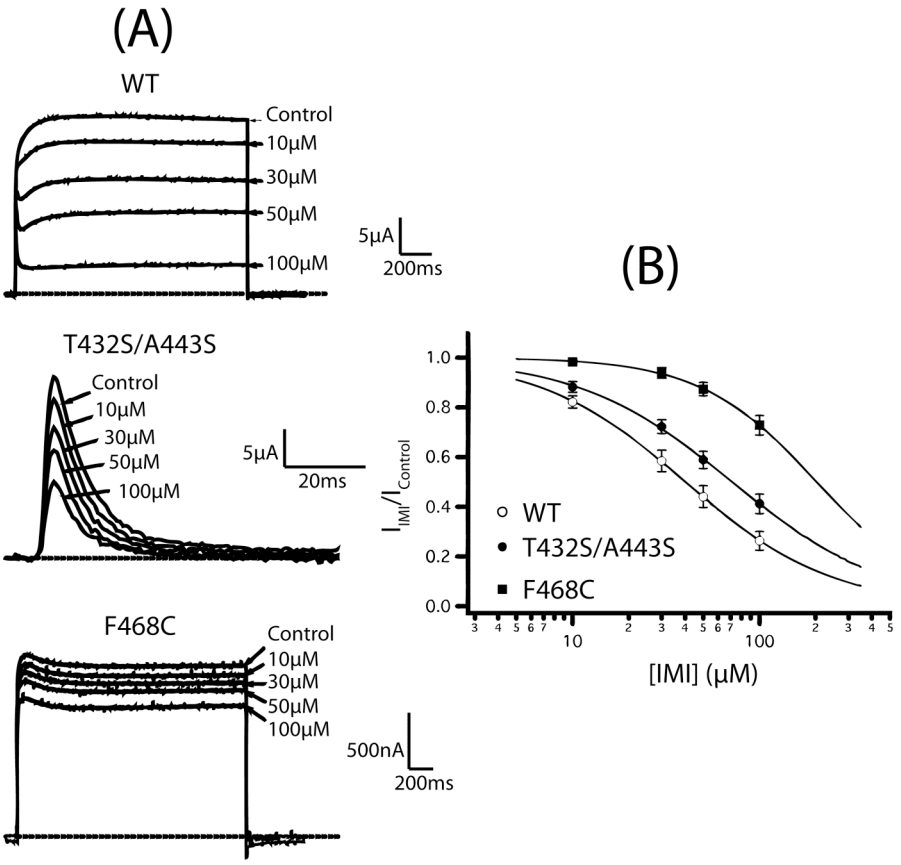

Figure 5-4 Concentration-dependent block of hEag1 WT, T432S/A443S and F468C by IMI

(A) hEag1 currents after the steady-state blockage with the indicated concentrations of IMI for WT (*upper traces*), T432S/A443S (*middle traces*) and F468C (*lower traces*). Traces were elicited by the same protocol as for Figure 5-3. The *dashed line* indicates the zero current level. (B) Dose-response curves of normalized mean data (n=8-10) obtained using the

protocol described in Figure 5-3. Currents were measured and normalized as in Figure 5-3. Additionally the Hill fit according to the Hill equation described in the *Material and Methods* is shown. The respective Hill coefficients were 40.2 and 1.11 for WT, 71.5 and 1.05 for T432S/A443S, and 202.5 and 1.39 for F468C.

5.3.4 Dofetilide - Mutations T432S/A443S and F468C

In a previous study, introduction of C-type inactivation into bovine Eag channels induced an increase in the blocking potency of Dofetilide (Ficker, 2001). Because both C-type inactivation and Phe656 residue are crucial for the DOF block in hErg channels (Ficker, 1998; Lees-Miller, 2000), we decided to characterize DOF binding to hEag1 WT, T432S/A443S and F468C channels.

As shown in Figure 5-5B, a steady state block of hEag1 WT channels was achieved with a DOF IC_{50} value of 29.6 μM (n=9). This value is in agreement with that previously reported for bovine Eag channels (31.8 μM;(Ficker, 2001)).

The introduction of inactivation in hEag1 channels increased the potency of blocking by DOF. DOF did not change the activation and inactivation kinetics of this mutant (data not shown), and the IC_{50} calculated for hEag1 T432S/A443S was 8.21 μM (Figure 5-5B; n=10). Therefore similarly to bEAG (Ficker, 2001), these mutations clearly reduce the IC_{50} value relative to the wild type hEag1 channel. This result confirms the assumption that the molecular determinants of DOF blocking are very alike for the hEag1 channel and the bovine isoform.

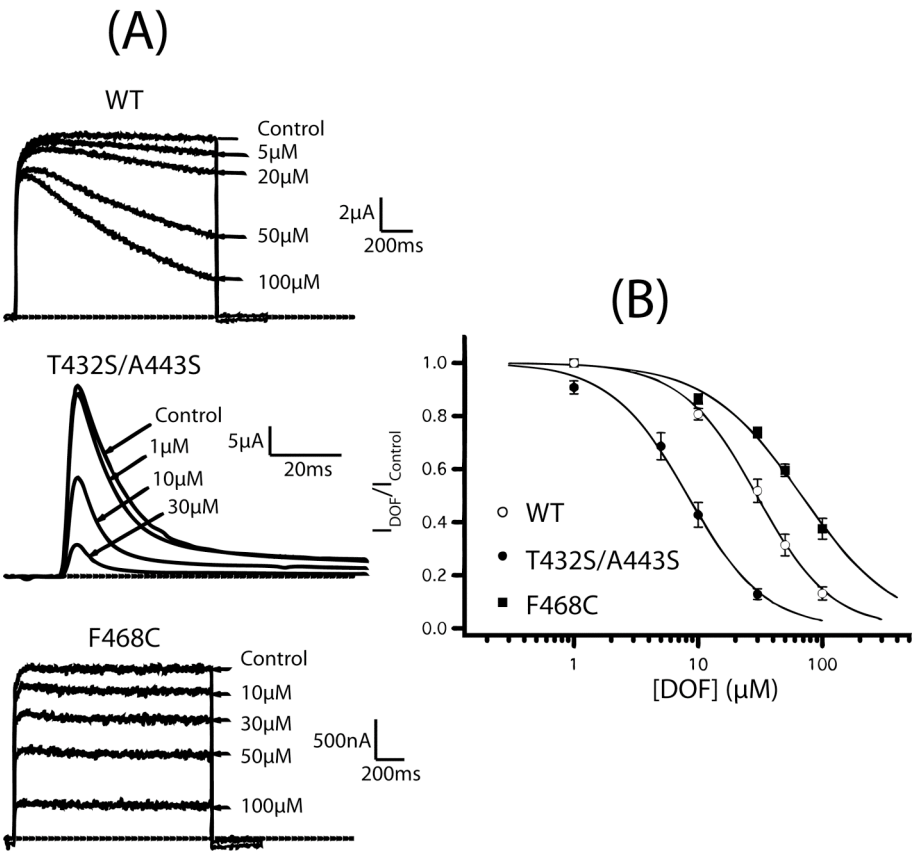

Figure 5-5 Concentration-dependent block of hEag1 WT, T432S/A443S and F468C by DOF

(A) hEag1 currents after the steady-state blockage with the indicated concentrations of DOF for WT (*upper traces*), T432S/A443S (*middle traces*) and F468C (*lower traces*). Traces were elicited by the same protocol as for Figure 5-3. The *dashed line* indicates the zero current level. (B) Dose-response curves of normalized mean data (n=9-10) obtained using the protocol described in Figure 5-3. Currents were measured and normalized as in Figure 5-3. Additionally the Hill fit according to the Hill equation described in the *Material and Methods* is shown. The respective Hill coefficients were 29.6 and 1.04 for WT, 8.2 and 1.4 for T432S/A443S, and 67.7 and 1.14 for F468C.

Dofetilide blocked hEag1 F468C with an IC_{50} of 67.7 μM (Figure 5-5B; n=10). Although this IC_{50} value is 2-fold greater than that for hEag1 WT, the loss of affinity is not as dramatic as that for hErg where a mutation in F656 increases the IC_{50} of DOF 100 fold (Lees-Miller, 2000). Therefore, although

our data suggest that the F468 residue plays a role in DOF binding to hEag1 channels, its importance seems to be less significant than that in hErg channels. A possible structural explanation for these data will be discussed later.

Mutations T432S/A443S and F468C alter the recovery from AST-, IMI- and DOF- mediated blockage in different ways. As we described above, introduction of C-type inactivation into hEag1 increases the blocking potency of AST and DOF, but not IMI, strongly suggesting that the binding site for IMI is different from the other two drugs. This hypothesis was further reinforced by studies on the block recovery.

After blocking the hEag1 WT current (Figure 5-6) with either 10 μM AST, 100 μM IMI or 100 μM DOF, between 40% and 90% recovery was achieved after a 5 minute wash. This strongly indicates that none of these drugs are trapped in the hEag1 channels during closing. In contrast, T432S/A443S and F468C mutations significantly slow the recovery from the block mediated by AST and DOF, but not that by IMI. After a 5 minute wash, the recovery percentages of T432S/A443S were 6.7% (AST) and 6.6% (DOF), and for F468C 31.2% (AST) and 11% (DOF). In contrast, as shown in Figure 5-6, recovery from IMI blocking was much faster for both mutants: 61% (T432S/A443S) and 96.2% (F468C).

In this experimental study, we applied the drug concentration necessary to obtain the maximum block. When lower concentrations of AST and DOF were used, sufficient only to block 50% of the T432S/A443S current, only 7.1% and 6.8% of the current after AST and DOF exposure, respectively, was recovered after 5 minute (not shown). This finding argues against the idea that the less efficient IMI-mediated hEag1 inhibition is responsible for the differences observed on the speed of recovery between the three drugs. Similarly, the slower recovery from AST and DOF treatment is probably not due to the low stimulation frequency used during the washing period, because we did not observe any significant increase in the recovery induced

by 20 preconditioning pre-pulses of 400 ms to +40 mV. This is similar to the described effects on bEag1 (Ficker, 2001). We believe that the differences in the recovery kinetics substantiate our hypothesis that the binding site in hEag1 shared, at least to some degree, by AST and DOF is different from that of IMI.

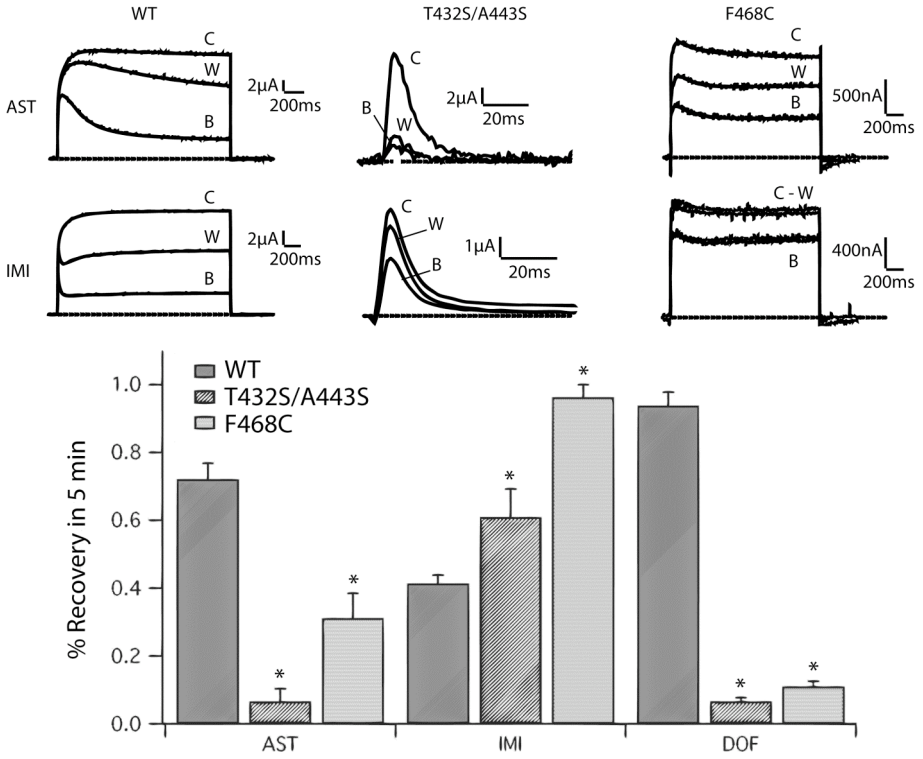

Figure 5-6 Differences in AST, IMI and DOF levels of block recovery between hEag1 WT, T432S/A443S and F468C channels.
(Upper traces). hEag1 WT, T432S/A443S and F468C currents prior to the block (C), after the steady-state block (B) and after the washout (W) of 10 μM AST and 100 μM IMI. Traces were elicited by the same protocol as in Figure 5-3. The *dashed line* indicates the zero current level. (Lower plot) Percentage of current at +40 mV recovered after 5 min of washing. Current at +40 mV was measured as indicated in Figure 5-3. The blocked current recovered after 5 minutes of washing was normalized to the total current blocked by each drug. The bars represent the SEM of 5-8 oocytes.

5.3.5 Dofetilide and MK-499 in hEag1 Channels.

In cardiac myocytes, DOF blocks the I_{Kr} current by a trapping mechanism (Carmeliet, 1992). A similar mechanism might be involved in the blockage of hErg in heterologous systems, because the washout of dofetilide is slower than in bEAG channels (Ficker, 1998). In the same way, dofetilide does not block hEag1 by a trapping mechanim (Figure 5-7A), as a DOF-mediated steady-state block using a concentration of 100 μM, is completely alleviated by a 5 minutes wash and the current is restored.

In order to extend this study to other methanesulfonanilide compounds we characterized the blocking mechanism of hEag1 by MK-499 (Figure 5-7A), which blocks hEag1 with an IC_{50} of 43.5 μM (n=4, data not shown). Recovery is complete in 5 minutes (Figure 5-7A), strongly indicating that for both DOF and MK-499 hEag1 blocking does not involve a drug trapping mechanism, in contrast to hErg channels (Mitcheson, 2000a). Recovery occurs with a time constant of 106.8 s for MK-499 and 82.6 s for DOF (Figure 5-7B). Additionally, a "foot in the door" mechanism (Kamiya, 2001) appears not to be implicated in the block of hEag1 by methanesulfonalinides, because the drugs do not alter the kinetics of deactivation, as can be deduced from the overlapping, normalized tail currents at -90 mV before and after the blocking with 40 μM MK-499 (Figure 5-7C). Exponential fits to the elicited tail current (Figure 5-7C) gave time constants of deactivation of 1.31±0.14 ms before, and 1.33±0.16 ms after the blocking (n=4).

Altogether, these results strongly indicate that, unlike in hErg channels, both MK-499 and DOF dissociate from hEag1 before it closes, and therefore blockage is not based on the trapping of the drug in the channel inner cavity during deactivation.

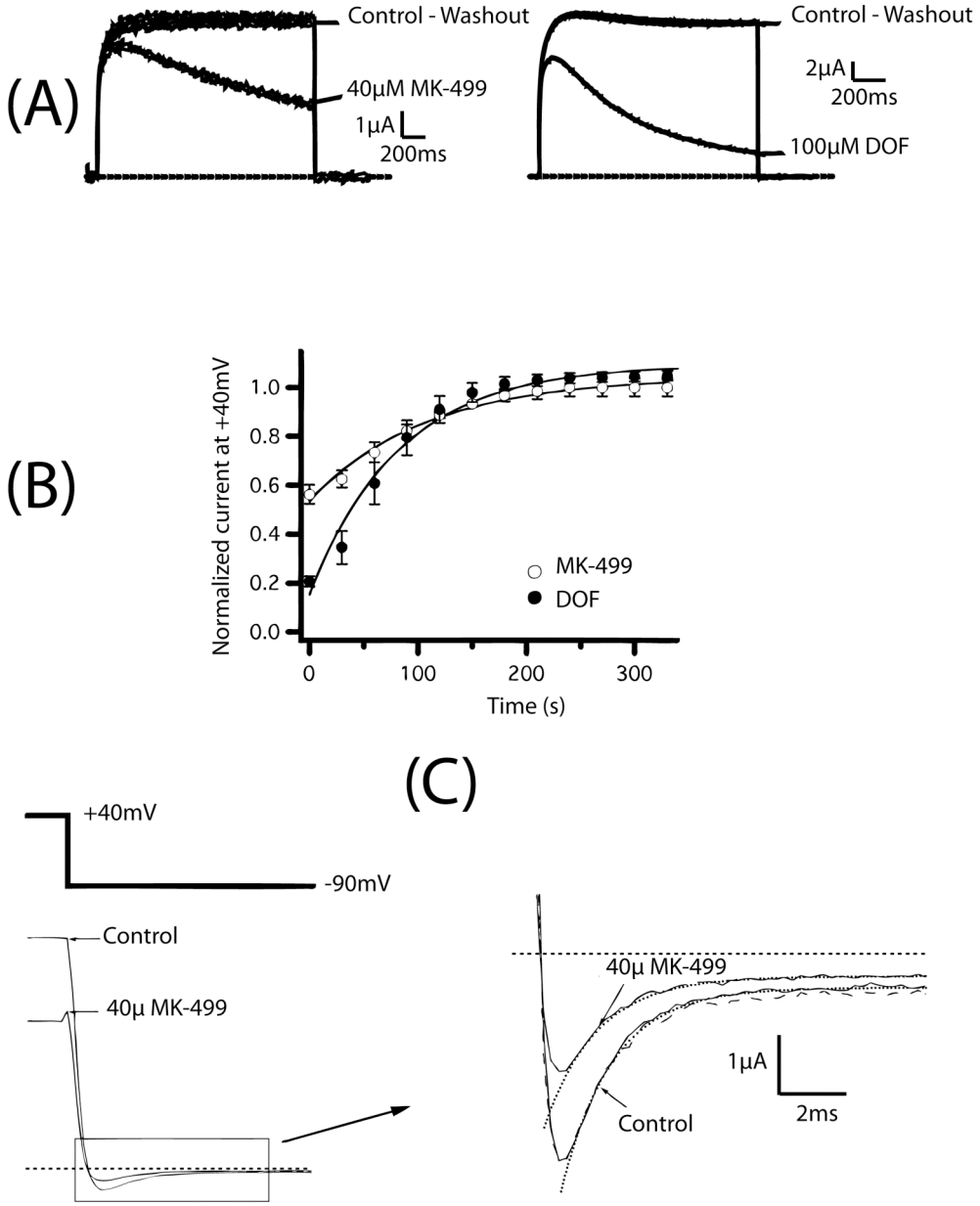

Figure 5-7 Mechanisms of block in hEag1 WT channels for DOF and MK-499
(A) hEag1 currents before the block (Control), in the presence of 40 μM MK-499 (*left traces*) and 100 μM DOF (*right traces*) and after washing (Washout). Traces were produced by the indicated protocol every 20 s. The *dashed line* corresponds to the zero current level. (B) Blocking recovery time-course during the washout of 40 μM MK-499 (open circles) and 100 μM DOF (closed circles). Currents were measured and normalized as in Figure 5-3. Additionally exponential fits to the currents according to the exponential equation described in the *Material and*

Methods are shown. The respective parameters were 1.04, -0.5 and 0.0093 for MK-499 and 1.09, -0.94 and 0.012 for DOF, respectively. (C) hEag1 WT currents in the absence (Control) and presence of 40 μM MK-499. Traces were produced according to the indicated protocol. The pulse at +40 mV had a duration of 2 s. *Right panel*, tail current traces recorded at -90 mV, in the absence (Control) and presence of 40 μM MK-499. The *dashed line* indicates the zero current level and the dotted line is the scaled tail current after addition of 40 μM MK-499 to the Control current level, allowing a better comparison of closing kinetics before and after the blocking to be made. Additionally, exponential fits to the currents according to the exponential equation under *Material and Methods* are shown. The respective parameters were -5.5, -2.55 and 762 for WT, and -6.79, -2.59 and 791 for MK-499.

5.4 Discussion

Many studies have shown that C-type inactivation and residues located at the C-terminal end of the S6 helix are key requirements for hErg channel blockage by several potent drugs (Kamiya, 2001; Wang, 1997). We have studied how the introduction of C-type inactivation into hEag1 channels and the mutation of a residue in the base of the S6 helix (Phe 468) affect AST, IMI and DOF blockage.

Similarly to bEag (Ficker, 2001) and hErg (Ficker, 1998) channels, C-type inactivation in the context of hEag1 increases the potency of blockage by DOF. We observed an equivalent effect for AST, but not for IMI. These three drugs ((Ficker, 1998), (Garcia-Ferreiro, 2004)), block Eag1 channels from the intracellular side. Current models predict that C-type inactivation of hErg results in a twisting of the S6 helices and a repositioning of Phe656 and Tyr652, to increase the sensitivity of the channel (Chen, 2002). Therefore, a similar movement is possible in the inner helices of hEag1 channels during C-type inactivation, thereby changing the position of some amino acids and increasing the affinity for AST and DOF but not IMI. Consequently, the increases in the potency of DOF and AST mediated channel block due to C-type inactivation represents an allosteric effect whereby changes in the structural conformation of the protein favor the binding of these two drugs,

but not IMI. In this study we additionally demonstrated that introduction of C-type inactivation into hEag1 renders DOF and AST blockage, but not that of IMI, irreversible (trapping). Interestingly, García-Ferreiro *et al.* demonstrated that AST and IMI compete for their binding site, which indicates that both drugs require common structures for the binding to hEag1 channels. In this study, we offer a plausible explanation for this competition, since we show that the activity of both drugs is sensitive to the Phe468 mutation. This suggests that the hydrophobic pocket formed by the Phe residues of the four subunits is important for the binding of both drugs. In conclusion, these data strongly suggest that the IMI binding site is different from that of AST and DOF, although it remains possible that some residues may still be common.

We detected clear differences between the blockage of hErg and hEag1 by distinct drugs. It is well established that mutations of hErg Phe656 increase the IC_{50} of DOF by 100-fold (Lees-Miller, 2000). However, mutation of the analogous Phe468 residue in hEag1 results in only a 2-fold increase in the IC_{50} value. While DOF is a high affinity, nanomolar hErg blocker, it has low, micromolar affinity for hEag1. However other low affinity hErg blockers, such as propafenone (Witchel, 2004), quinidine (Lees-Miller, 2000), chloroquine (Sanchez-Chapula, 2002) and vesnarinone (Kamiya, 2001) also are affected by mutations of the Phe656 residue. Furthermore, we also show that another low affinity blocker of hEag1 (IMI) is sensitive to Phe468 mutation. Taking this information together indicates that the various affinities of DOF for hErg and hEag1 are not the basis for the different sensitivities to the hEag1 Phe468 mutation. In addition, we also describe here that blockage mediated by DOF, AST, IMI and MK-499 is reversible in hEag1 channels, which contrasts with the extremely slow or non-reversible blocking (trapping) of these drugs in hErg channels (Mitcheson, 2000b; Snyders, 1996; Suessbrich, 1996; Teschemacher, 1999). All these features

highlight the clear differences that exist between hEag1 and hErg in terms of their sensitivity to various blockers.

In order to understand our results and for the design of further experiments, we generated a molecular model of hEag1 using the crystal structure of the mammalian Kv1.2 channel in the open state conformation (Long, 2005). It is important to note that Kv1.2 shows a Pro-Val-Pro motif in the S6 domain that has been described to be important for curving the inner helices during channel activation (del Camino, 2000), while the hEag1 channel, like KvAP, has a Gly residue in the corresponding position. Although we reached identical conclusions when using either KvAP or Kv1.2 as a template, probably because the Gly residue in KvAP also produces a curvature of the inner helices (Long, 2005), we will only comment on our results obtained employing Kv1.2.

Figure 5-8 shows the docking model for AST and DOF in the hEag1 vestibule. At first glance, it is clear that the hydrophobic rings of AST are closer than those of DOF to the Phe residue rings. It is also interesting to note that, although the conformation of the inactivating mutant (T432S/A443S) could not be predicted, our model suggests that the effects observed in the double mutant T432S/A443S could be allosteric, since neither of these two residues are in close proximity to the drugs. The *in silico* analysis also predicts that other residues in the selectivity filter could interact with the drugs and be important for their stabilization inside the inner vestibule, as has been described for some residues at the base of the pore helix of hErg and hEag1 (Mitcheson, 2000a). Interestingly, our model suggests that all three drugs could interact with Tyr464 (one helical turn away from Phe468) to make a cation-π interaction, which is the most important interaction between the analogous residue in hErg and the tertiary nitrogen of cisapride, terfenadine and MK-499 (Fernandez, 2004). Furthermore, the model suggests that the permanently charged AST derivative, NMA, would have an increased capacity to block hEag1 relative

to AST itself, since the charged nitrogen in NMA would be close enough to establish a cation-π interaction with the Tyr464 residue. Further mutagenesis studies will be necessary to elucidate the role of these residues in the blocking process of hEag1 by different drugs.

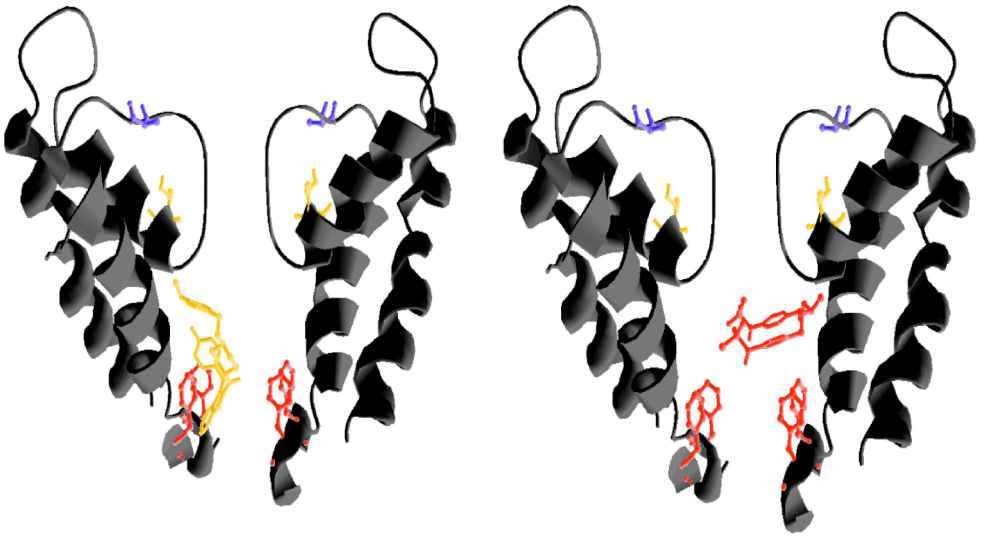

Figure 5-8 Docking of AST and DOF within the cavity of the hEag1 K^+ channel as constructed by homology
A. Homology model showing the S5-S6 domains of two hEag1 subunits with a docked molecule of AST (*left panel*) and DOF (*right panel*). F468 (red), T432 (blue) and A443 (yellow) residues are shown as balls and sticks.

Molecular modeling also provides us with a possible explanation for the effects of the Phe468 mutation. It is accepted that a π-π stacking interaction between two hydrophobic aromatic rings is energetically favorable dependent on the orientation and proximity of the phenyl groups (Hunter, 1991; McGaughey, 1998). The distance between the carbon atoms of the interacting rings ($R_{closest}$) must be between 3.4 and 4.5 Å (Hunter, 1991; McGaughey, 1998). To predict interactions between the different drugs and the Phe468 residue, we measured $R_{closest}$ between the four Phe rings of the channel and the atoms of the various aromatic groups of the drugs. Three of the phenyl groups of AST, nearly two in IMI and practically none in DOF

show $R_{closest}$ values within the 3.4-4.5 Å interval with respect to one or several phenylalanine hydrophobic rings. Figure 5-9 and Figure 5-10 indicate all the $R_{closest}$ values close to this interval for the three different drugs. This might explain the weak effect that the Phe468 mutation has on the block achieved by DOF and the large effect observed for AST and IMI.

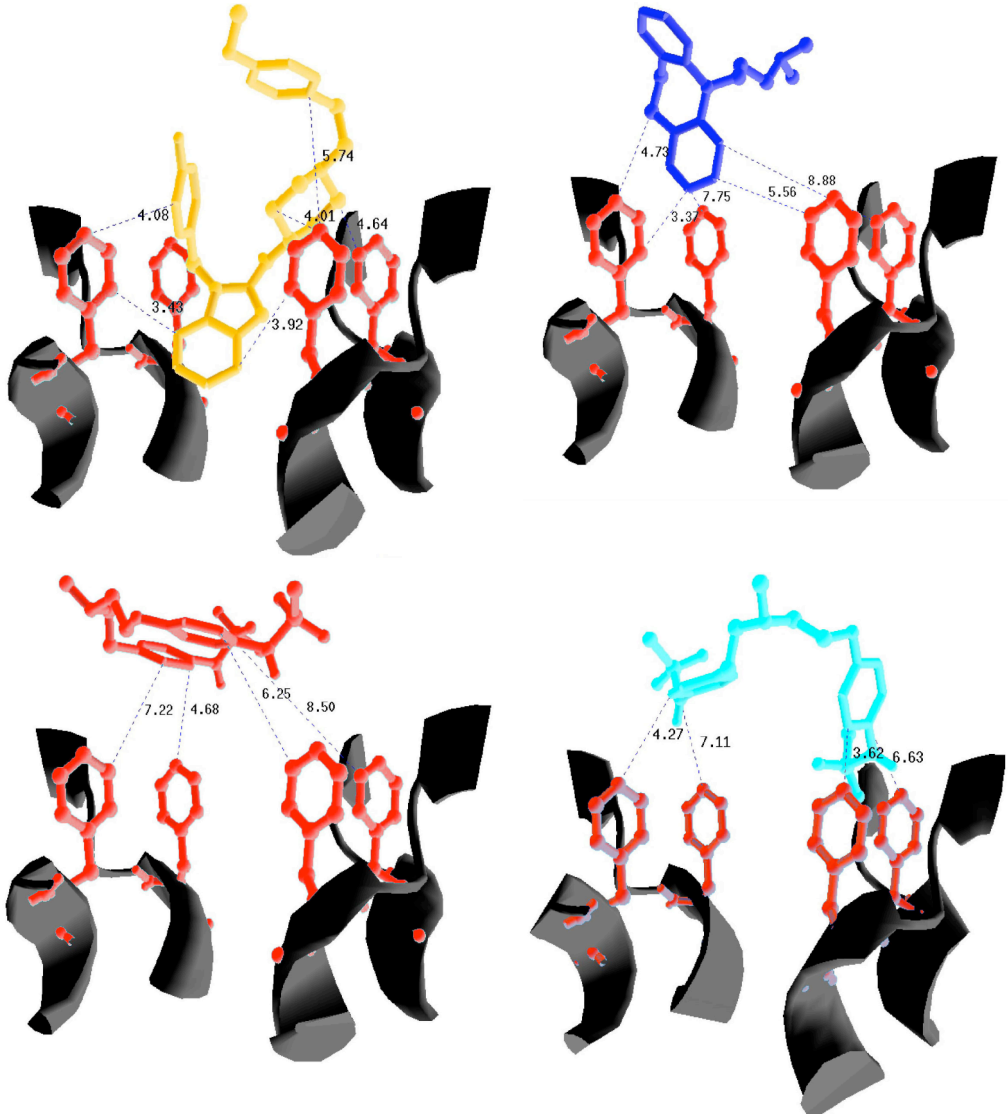

Figure 5-9 Distances between blocking drugs and the Phe residues in S6
Close-up views of the C-terminal end of the S6 helix showing the four F468 residues and the relative position of the drugs. The upper panels and lower left panel

correspond to hEag1 homology models with AST (yellow, *upper left*), IMI (blue, *upper right*) and DOF (red, *lower left*). For AST and DOF and for better observation, the structures are rotated about the Y axis with respect to the structures in Figure 5-8. The lower right panel is the hErg homology model with DOF (in light blue) and the F656 residues of the four subunits in red. In all four panels, the closest distances between the aromatic rings atoms of the phenylalanine residues and the drugs ($R_{closest}$) are indicated as dashed lines with the values in Å.

In order to validate the usefulness of the $R_{closest}$ parameter as an indication for possible π-π stacking interactions, we also developed a model of hErg using Kv1.2 as the template (Figure 5-9, lower right) and studied the docking of DOF. Interestingly, $R_{closest}$ analysis shows that DOF is closer to the Phe residues in hErg than in hEag1 channels (Figure 5-10). This would fit with recent studies that suggest that the orientation of the S6 aromatic residues with respect to the central cavity of hErg differs from those of Eag channels (Chen, 2002). Although other interactions must be important for DOF binding to hErg channels, this data could explain why a mutation in these Phe residues affects DOF binding more to hErg than to hEag1.

In summary, the experimental differences detected in this study between the AST, IMI and DOF binding process to hEag1 channels correlates well with information obtained from our molecular modeling approach. This demonstrates that a mutagenesis analysis together with an *in silico* approach are good tools to construct a general pharmacophore model that may represent a template for the future synthesis of a specific and potent hEag1 blocker.

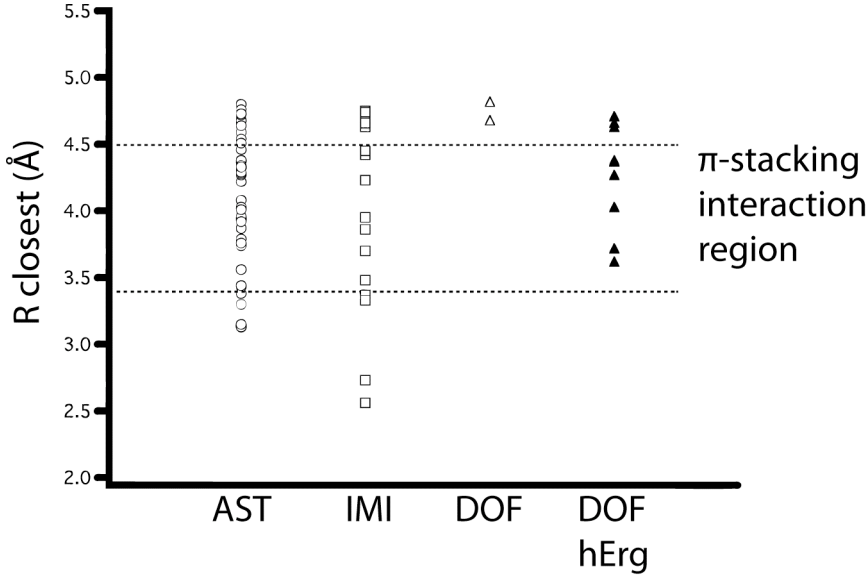

Figure 5-10 π interactions between blocking drugs and Phe aromatic ring
Aromatic ring (π– stacking) interactions in terms of phenylalanine aromatic ring atoms within the 3.4-4.5 Å of the drug phenyl ring atoms. This interval was taken to be the optimal inter-atomic distance of aromatic ring atoms that give rise to favorable π-stacking interactions (McGaughey, 1998). All the inter-atomic distances within the interval and beyond this interval are indicated for AST-hEag1 docking (empty circles), IMI-hEag1 docking (empty squares), DOF-hEag1 docking (empty triangles) and DOF-hErg docking (full triangles). The dashed lines represent the $R_{closest}$ values of 3.4 and 4.5 Å.

Chapter 6

Water Fluxes Through the KcsA Potassium Channel

The KcsA potassium channel has an osmotic permeability coefficient of 4.8 × 10^{-12} cm^3/s, higher than the osmotic permeability coefficient of some membrane channels specialized in water transport (Saparov, 2004). This high osmotic permeability requires the channel to be depleted from potassium ions, which otherwise would slow down the water permeation. The structure of the potassium-depleted KcsA channel, as the mechanisms of water permeation, are still unknown, and are here analyzed by all-atom molecular dynamics simulations, in conjunction with an umbrella sampling strategy and a novel approach to simulate pressure gradients (Zhu, 2002). Equilibrium molecular dynamics simulations (60 ns) identified a possible structure of the potassium-depleted KcsA channel, and umbrella sampling calculations revealed that this structure is not permeable by water molecules moving along the channel axis. The simulation of a pressure gradient across the channel (30 ns) identified an alternative permeation pathway, with sustained osmotic permeability. Water fluxes along this pathway did not proceed through collective water motions or transitions to vapor state. All the major results were robust against variations in a wide set of simulation parameters (force field, water model, membrane model, and channel state).

6.1 Introduction

Potassium ions and water molecules move through potassium channels in a concerted way. Experimental data and numerical simulations support a 1:1 ratio between the number of water molecules and potassium ions crossing a K^+ channel (Alcayaga, 1989; Berneche, 2001). The accepted view is that water and ions move through the selectivity filter (SF) of K^+ channels in single file, as exemplified by numerous molecular dynamics (MD) simulations (Aqvist, 2000; Berneche, 2000; Compoint, 2004; Domene, 2003). However, what happens when the concentration of K^+ is so low that the channel is depleted of ions? Saparov and Pohl (Saparov, 2004) measured water flow through potassium-depleted KcsA, and found a surprisingly high osmotic permeability coefficient, p_f = 4.8 × 10^{-12} cm^3/s. This osmotic permeability is about two orders of magnitude larger than those of some specialized water-conducting pores of the aquaporin family (Yang, 1997). A quick back-of-the-envelope calculation for the "intrinsic flux", $\phi_0 = 2\,p_f / V_w$ (de Groot, 2002), using the KcsA value for p_f and the water volume V_w = 30 $Å^3$, suggests that in equilibrium ~300 water molecules cross the KcsA channel per nanosecond. Considering the timescales associated with these permeation events, water fluxes should be detected in nanosecond MD simulations of KcsA. In this chapter, we report on such simulations and provide a detailed atomic picture of the water dynamics, and the structural changes that the channel undergoes in the absence of potassium ions.

The occupation of potassium ions has been shown to strongly affect the SF structure. In high-K^+ concentrations, the carbonyl oxygens of the SF point towards the central pore, as revealed by X-Ray crystallography, and each potassium ion is coordinated by eight backbone carbonyl oxygens (Doyle, 1998). Five potassium-binding sites were identified inside the SF, and are named S0 (intracellular side of the SF) to S4 (extracellular side of the SF), as outlined in section 1.2. In high-K^+ concentration two ions occupy the SF on

average, with a water molecule between them. Two configurations of ions and water, K^+-water-K^+-water and water-K^+-water-K^+, are thought to be the most stable ones in the KcsA K^+-channel. A low energetic barrier (~2-3Kcal/mol) between these two configurations allows rapid K^+ conduction through the SF (Berneche, 2001). The X-ray structure of the SF changes dramatically in low potassium concentration. At low potassium concentration the average occupancy of the SF is one potassium ion (Zhou, 2001). The carbonyl oxygen of Val76 does not point towards the filter lumen, Gly77 adopts a new conformation, and K^+ ions are only observed in S1 and S4. It is easily imagined that total absence of potassium ions in the SF would prompt further rearrangements in its atomic structure. Indeed, the SF of K^+ channels is far from being a rigid structure. MD simulations of KcsA (Berneche, 2000; Domene, 2003; Noskov, 2004a), and KirBac1.1 (Domene, 2004) described certain degree of flexibility in the SF, even in the presence of potassium ions. Depletion of potassium ions cause severe distortions of the SF both in KcsA and KirBac1.1 (Domene, 2004; Domene, 2003), which can be explained by the repulsion between carbonyl oxygens in the absence of stabilizing potassium ions.

The MD simulations reported in this chapter aim at shedding light on the nature of the transport of water molecules through the KcsA K^+-channel in the absence of ions, and at describing at atomic detail the structural changes that the SF undergoes. We began by performing equilibrium MD simulations of the system, using two different protein force fields and water models. As expected, in the absence of potassium ions, the X-Ray structure in high-K^+ concentration was no longer stable, and the SF evolved towards a new structure. The equilibrium MD simulations failed to capture the experimental high water permeation rates, and potential of mean force calculations showed that a significant energy barrier (~7Kcal/mol) hampers the water movements along the pore axis. To investigate alternative pathways for water permeation, simulations of KcsA were performed under the equivalent

of an osmotic pressure difference across the SF, employing a method proposed by Zhu et al. (Zhu, 2002). Pressure gradients induced appreciable water fluxes across KcsA, along a permeation pathway extending behind the SF. Permeation along this pathway does not proceed trough liquid-vapor oscillations. Transitions to vapor state were proposed as a possible mechanism explaining the high osmotic permeability of KcsA (Saparov, 2004), but were never observed in the whole simulated time (~100 ns). All the numerical simulations were repeated restraining the SF to the X-Ray structure in high-K^+ concentration. No water flux was detected across this configuration of the SF, which proves that structural changes are required for water permeation.

6.2 Methods

6.2.1 Equilibrium Molecular Dynamics Simulations

The osmotic permeability of a channel (p_f) is defined by:

$$J_w = p_f \Delta C \qquad \textbf{Equation 6-1}$$

where ΔC is the concentration gradient, and J_w is the water flux. If no concentration gradient is applied, like in equilibrium MD simulations, the net water flux is zero. Water molecules may travel through the channel pore, but the outwards and inwards fluxes ($J_{outward}$ and J_{inward}) will cancel each other on average. The ratio between the unidirectional water-flux, $J_{eq} = J_{outward} = J_{inward}$, and the water concentration C_w defines the diffusion permeability of the channel, $p_d = J_{eq}/C_W = J_{eq}V_w$(where the volume of a water molecule, V_w = 30 Å^3, was employed to define C_w). If water molecules

move in a single file, the diffusion permeability is related to the osmotic permeability by:

$$p_f = \frac{p_d}{N+1} \qquad \textbf{Equation 6-2}$$

where N is the number of water molecules in the single-file (Zhu, 2004). Unidirectional fluxes are simply the number of water molecules permeating the pore per unit time, directly obtained from equilibrium MD simulations. Within the single file assumption, Equation 6-2 can be used to estimate the osmotic permeability, once the length of the single-file column is known.

Several equilibrium MD simulations were performed, using different: i) channel models; ii) force fields and water models; iii) membrane compositions; iv) restraints on the selectivity filter (see Table 6-1 for details). Simulations denoted MD_GU, MD_GR, and MD_NUC used a KcsA model based on the X-Ray structure at 2 Å resolution in high-K^+ concentration (Protein Data Bank entry 1K4C (Zhou, 2001)). An acetyl group was added to the N-terminal (residue Ala23), and the C-terminal (residue Gly123) was protonated. All the residues were in the default protonation state, except Glu71 which was protonated to form a diacid hydrogen bond with the carboxylate group of Asp80, following the results presented by Ranatunga et al. (Ranatunga, 2001), and Bernerche and Roux (Berneche, 2002).

A model of the KcsA channel in the open state was used for the simulations denoted MD_NU, MD_NUP, and MD_NR. The open model of KcsA was defined as in section 4.2.1, using the crystallographic structure of MthK as a template.

	Simulation Type	Channel State	Membrane	Force-Field	Water Model	Selectivity Filter	[ns]
MD_GU	MD	Closed	POPC	GROMOS-96	SPC	Unrestrained	15
MD_GR	MD	Closed	POPC	GROMOS-96	SPC	Restrained to high-K^+	15
MD_K	MD	Closed	POPC	GROMOS-96	SPC	K^+ in S1 and S3	5
MD_NU	MD	Open	Octane	CHARMM-27	TIP3	Unrestrained	15
MD_NUP	MD	Open	POPC	CHARMM-27	TIP3	Unrestrained	15
MD_NUC	MD	Closed	Octane	CHARMM-27	TIP3	Unrestrained	15
MD_NR	MD	Open	Octane	CHARMM-27	TIP3	Restrained to high-K^+	15
US_U	Umbrella Sampling	Closed	POPC	GROMOS-96	SPC	Unrestrained	2x40
US_R	Umbrella Sampling	Closed	POPC	GROMOS-96	SPC	Restrained	2x40
PRS_U	Pressure MD ΔP=200MPa	Open	Octane	CHARMM-27	TIP3	Unrestrained	7.5
PRS_UP	Pressure MD ΔP=200MPa	Open	POPC	CHARMM-27	TIP3	Unrestrained	7.5
PRS_UC	Pressure MD ΔP=200MPa	Closed	POPC	CHARMM-27	TIP3	Unrestrained	7.5
PRS_R	Pressure MD ΔP=200MPa	Open	Octane	CHARMM-27	TIP3	Restrained to high-K^+	7.5

Table 6-1 Summary of simulations

An octane membrane was used in the simulations MD_NU, MD_NR, and MD_NUC, while a POPC membrane was used in the simulations MD_GU, MD_GR, and MD_NUP. The channel was inserted in a pre-equilibrated membrane (516 octane molecules, or 256 POPC molecules), with the pore axis orthogonal to the membrane boundaries. The extracellular aromatic belt (aminoacids Tyr45) was aligned to the upper boundary of the membrane. Membrane molecules closer than 1.2 Å from protein atoms were removed. The system was solvated, and chloride ions were added to neutralize the protein charges.

Simulations denoted by MD_GU and MD_GR were performed with GROMACS3.3 (Van der Spoel, 2005), using the GROMOS-96 (43a2) united atom force field (van Gunsteren, 1996), and the simple point charge (SPC) model for water molecules (Hermans, 1994). The LINCS algorithm was used to preserve the bond lengths, in order to use a 2 fs time step (Hess, 1997).

The coordinates were saved every 10 ps. Long-range electrostatic interactions were treated by the Particle Mesh Ewald algorithm (Essmann, 1995), and a 10 Å cut-off was used for the Van der Waals interactions. The pressure was controlled at 1 bar by coupling to a pressure bath (time constant of 1 ps), and temperature was kept at 300 K by coupling to a temperature bath (time constant 0.1 ps) (Berendsen, 1984). Energy was first minimized by a steepest descent procedure, followed by an equilibration period (200 ps) where harmonic restraints were applied to the protein atoms. After equilibration, MD simulations were run for 15 ns. In MD-GU all the atoms were unrestrained, while in MD-GR the backbone atoms of the SF were restrained to the crystallographic structure in high-K^+ concentration (Zhou, 2001) by a harmonic potential (force constant 2 Kcal*mol^{-1}* $Å^{-2}$).

The MD simulations denoted MD_NU, MD_NR, MD_NUC, and MD_NUP were run using NAMD2.6 (Kale, 1999), and the CHARMM-27 all atom force field (MacKerell, 1998) with the TIP3 water model (Jorgensen, 1983). The time step was set to 2 fs (SHAKE algorithm (Ryckaert, 1977)), and the coordinates were saved every 10 ps. Long-range electrostatic interactions were treated by the Particle Mesh Ewald algorithm (Essmann, 1995), and a 10 Å cut-off was used for the Van der Waals interactions. Langevin dynamics controlled the temperature at 300K, with a dumping factor of 5 ps^{-1}. The Langevin piston Nose-Hover method (Feller, 1995; Martyna, 1994) was used to keep a pressure of 1 bar (piston period was 200 fs and the dumping time scale was 100 fs). Harmonic restraints were applied to the protein backbone, and the energy was minimized by 10,000 steps of steepest descent. Constraints on backbone atoms were then gradually removed. A 5ns MD was run to equilibrate the simulations with the open channel model (MD_NU, MD_NUP, and MD_NR), while a 200 ps MD was run to equilibrate the simulation with the closed channel model (MD_NUC). After equilibration, MD simulations of 15 ns (MD_NU, MD_NR) or 5 ns (MD_NUP, MD_NUC) were run. In MD_NU, MD_NUP, and MD_NUC all

the atoms were unrestrained, while in MD_NR the backbone atoms of the SF were restrained to the X-Ray structure in high-K^+, as in MD_GR.

6.2.2 Umbrella Sampling

The umbrella sampling technique (Torrie, 1974) was used to compute the potential of mean force (PMF) for a water molecule moving along the channel axis. Calculations were confined to a 2 Å long region, which extends from the intracellular side of the SF, Thr75, to its extracellular side, Gly79. This region was divided in 40 windows, and 2 ns of MD were run for each window. The atomic system and the simulation parameters were as in MD_GU. The starting configurations were selected from the last 5 ns of MD_GU, choosing snapshots where a water molecule was closest to the center of the window. This water molecule was restrained to the window center by a harmonic potential (force constant set to 2 Kcal*mol^{-1}* Å $^{-2}$), and its coordinates were saved every 1 ps. The harmonic restraints were applied along the channel axis only (z axis), while water molecules were free to move in the orthogonal plane (x-y plane). The first 500 ps of each simulation were discarded for the analysis. The remaining data were divided in three sets, each including 500 ps of MD. The unbiased PMF was computed by the weighted histogram analysis method on each data set, recombining the biased distributions of the z position of the restrained water molecules (Kumar, 1992). The PMF was estimated as the mean value of the three data sets with the standard deviation of the data sets providing an estimate of the error.

Outside the SF, the PMF can be related to the equilibrium density of water molecules in MD simulations ($n(z)$) by:

$$G(z) = -kT \ln \frac{n(z)}{n_0} + G_0 \qquad \textbf{Equation 6-3}$$

where n_0 is the water density far from the channel, and G_0 is the free energy of the reference state. The water density along the channel axis was defined by the trajectory of the MD simulation denoted MD_GU. The PMF defined by Equation 6-3 was combined to the PMF computed by the umbrella sampling technique, matching the two PMF profiles at the boundaries of the SF.

The same procedure was used to compute the PMF through the SF restrained to the X-Ray structure in high-K^+. A MD simulation with potassium ions inside the channel was run to generate the starting configurations for this set of umbrella calculations (MD_K). The atomic model for MD_K was defined as in MD_GU, but keeping the crystallographic potassium ions at the binding sites S1 and S3 and in the cavity. This simulation was run for 5ns, using the same settings of MD_GU. The starting configurations for the umbrella simulations were picked from the last 3 ns, choosing the snapshots with a water molecule or a potassium ion closer to the center of the window to be simulated. All the potassium ions inside the channel and three chloride ions in bulk solution were then artificially mutated to water molecules. In the umbrella sampling simulations, the backbone atoms of the filter were restrained to the starting configuration by harmonic potentials. A force constant of 2 Kcal*mol^{-1}* $Å^{-2}$ was used. The restraints proved to be appropriate for keeping the SF in the high-K^+ structure, with all the carbonyl oxygens pointing towards the channel axis on average, but allowing enough freedom to let the backbone adjust depending on the occupancy of the filter. Outside the SF the PMF was defined by Equation 6-3, using the data of the simulation MD_GR to compute the water density along the channel axis.

6.2.3 Pressure Molecular Dynamics

Equation 6-1 defines the water flux produced by a concentration gradient, ΔC. In a dilute solution the same water flux results from a pressure gradient, $\Delta P = RT\Delta C$, where R is the gas constant and T is the temperature. As a consequence, the osmotic permeability can be simply estimated in MD simulations, by applying a pressure gradient across the channel. Zhu et al. (Zhu, 2002) proposed a method to generate a pressure gradient in MD simulations. The idea is to apply a constant force (f) to all the water molecules in a slab away from the region of interest. If these forces are orthogonal to the slab, a net force equal to nf (n being the number of water molecules in the slab) acts on the boundary surface, in the direction of the forces. This net force is equivalent to a pressure gradient across the slab of

$$\Delta P = \frac{nf}{A} \qquad \textbf{Equation 6-4}$$

where A is the area of the boundary surfaces. In order to apply the pressure gradient across a protein channel in a simulation with periodic boundary conditions, the upper and lower surfaces of the slab are placed respectively at the extracellular and intracellular side of the channel, and the force f is applied outside these surfaces (Figure 6-1).

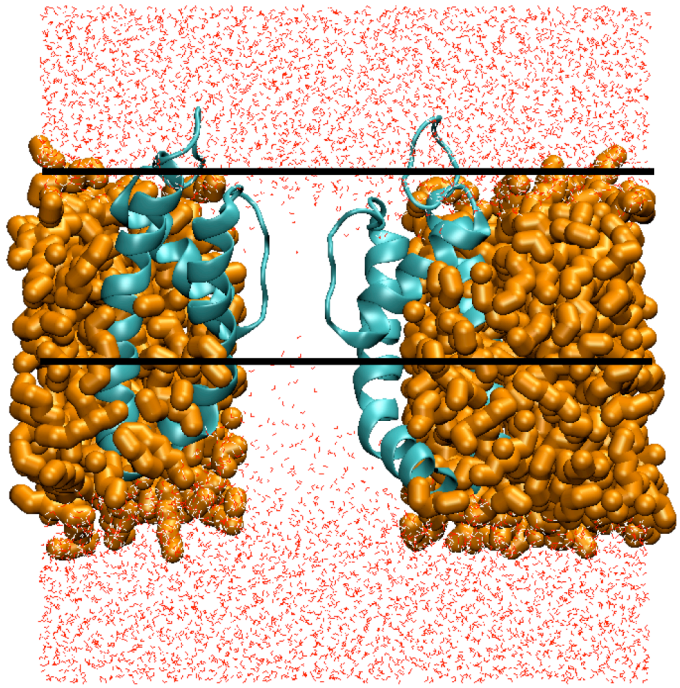

Figure 6-1 Simulated molecular system.
A longitudinal slice of the simulated molecular system is shown, using a licorice representation for the octane molecules, the cartoon modality for the two subunits of the KcsA channel, and lines for the water molecule. The black horizontal lines edge the region where the forces used to mimic a pressure gradient are not applied.

MD simulations with pressure gradient were performed with NAMD2.6 (Kale, 1999) in the NVT ensemble. Four different MD were simulated (Table 6-1) In PRS_U and PRS_R the atomic system was defined using the last step of MD_NU and MD_NR respectively. The atomic system of PRS_UC was defined as in MD_GU, thus using a POPC lipid membrane and the closed structure for the KcsA channel. A POPC lipid membrane was used also in PRS_UR, but combined with the open model of the KcsA channel. The additional force, f, was applied to all the water molecules above z = +10 Å or below z = -9 Å (Figure 6-1). Since the geometrical center of the SF was in z = 0 Å, and the filter extended from z = -6 Å to z = +6 Å, the dynamic of water molecules in the filter was not biased by the

additional forces. The value of the applied forces was assigned in order to simulate a pressure gradient of 200 MPa. Harmonic potentials (force constant 0.04 Kcal*mol^{-1}* Å $^{-2}$) were applied to the α-carbon atoms of the protein (with the exception of segment Thr74 to Leu81) and to the carbon atoms of the membrane (octane or POPC molecules) to avoid the translation of the membrane in the simulation-box. In the simulations PRS_U, PRS_UC and PRS_UP, the SF was not restrained, while in the simulation PRS_R, the backbone atoms of the SF were restrained by harmonic potentials (force constant 2 Kcal*mol^{-1}Å $^{-2}$) to the X-Ray structure in high-K^+ concentration. The length of the MD simulations with pressure gradient was 7.5ns; the last 7ns were used for the water flux analysis.

6.3 Results

6.3.1 Unrestrained Selectivity Filter

In the simulation denoted MD_GU (closed channel model, in POPC bilayer, with unrestrained SF), the SF adopted a new stable structure after 2 ns (Figure 6-2). A cluster analysis was performed on the last 13 ns of the simulation using the algorithm described in (Daura, 1999). Structures where the root mean square distance (RMSD) of the SF backbone atoms was less than 1 Å were included in the same cluster. More than 90% of the MD snapshots belonged to a single cluster. The average structure of the SF in this cluster is shown in Figure 6-3. The potassium depleted SF is far from being symmetric, and the four SF monomers are no longer aligned along the axis. As a consequence, carbonyl oxygens belonging to analogous residues on different monomers do not face each other. Two subunits come closer than in the high-K^+ structure of the channel (Figure 6-3). These subunits adopt an hourglass shape, with the carbonyl oxygen of the aminoacids Val76 pointing outward. The other two subunits of the filter adopt a geometrical structure

more similar to that of the X-Ray structure in high-K^+ concentration (Figure 6-3). The structure of the SF observed in MD_GU is almost closed between Val76 and Gly77. No water molecule moved across the SF in 15 ns, which it is translated in low diffusion permeability, and according to Equation 6-2, low osmotic permeability.

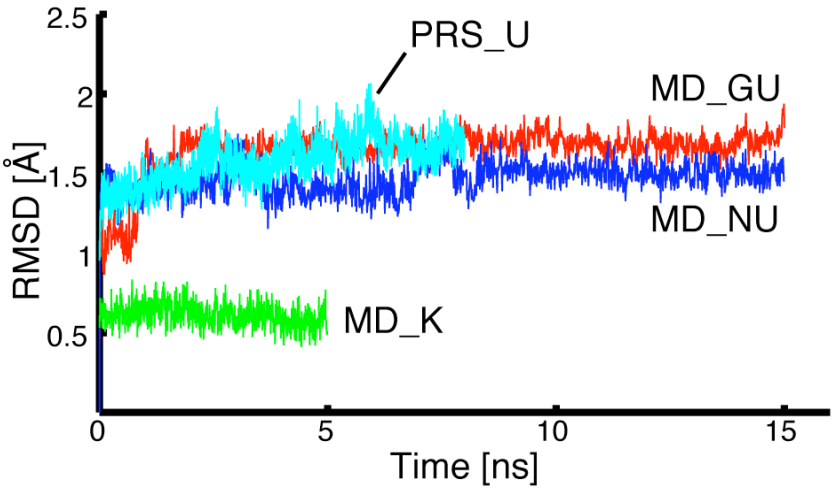

Figure 6-2 Root mean square deviation of the backbone atoms of the selectivity filter in several of the classical molecular dynamics simulations.
The root mean square deviation refers to the crystal structure of the SF in high-K^+ (Zhou, 2001).

Liquid-vapor oscillations were suggested as a possible mechanism explaining the high osmotic permeability of KcsA (Saparov, 2004). In order to test this hypothesis the water density was monitored. The number of water molecules closer than 3 Å to any backbone atoms of the SF was 8±2, and this distribution did not show any sharp fluctuation, which excludes the transition of liquid water to the vapor state, at least on the simulated time-scale.

The MD_GU simulation failed to produce any appreciable water flux, in contrast to what it should be expected from the experimental results.

Therefore, in order to analyze the underlying free energy landscape of water permeation through the channel, the PMF for water in the potassium-free KcsA filter was computed (Figure 6-4). The most favorable position for a water molecule along the filter axis was at the intracellular side of the aminoacids Val76. Actually, a water molecule is confined in this position in the 15 ns of MD_GU (mean square displacement below 1 $Å^2$). The low water mobility together with the high energetic barrier (6.7±0.7Kcal/mol for outward movement between the aminoacids Val76 and Gly77) suggests that water fluxes through this structure of the SF are unlikely.

The MD simulation denoted MD_NU (open channel model, in octane slab, with unrestrained filter) provided equilibrium water fluxes similar to MD_GU. Only two water molecules moved across the SF in the 15 ns of MD_NU. As in MD_GU, the SF shortly stabilizes (~500ps) into a new structure (Figure 6-2), where the four-fold symmetry was lost (Figure 6-3). A cluster analysis was performed on the last 13 ns of the trajectory by the same algorithm used for MD_GU. Most of the SF structures in this period of time (95%) were in the same cluster. The average structure of the SF in MD_NU was ~2 Å far from the average structure of the SF in MD_GU (RMSD of the backbone atoms). The extracellular side of the SF is wider in MD_NU, and consequently the number of water molecules close to the SF is higher (13±2 in MD_NU, versus 8±2 in MD_GU). In spite of these differences, several structural characteristics of the SF are conserved. Both in MD_NU and MD_GU, two subunits of the SF approach each other forming an hourglass shape, while the other two subunits stay apart. The SF is almost closed between the aminoacids Val76 and Gly77, and water molecules cannot move through this narrowing of the filter. Moreover, the number of water molecules close to the SF did not show any sharp fluctuation in MD_NU, as in MD_GU.

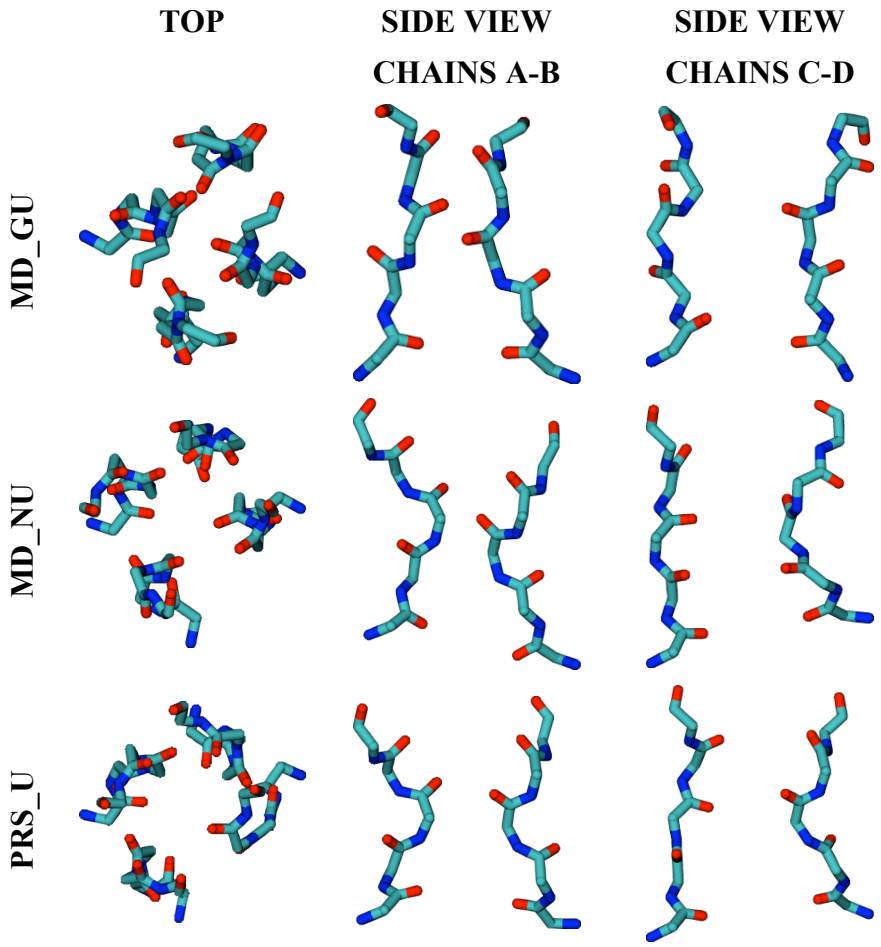

Figure 6-3 Structure of the selectivity filter depleted from K^+ ionsAverage backbone structures from three molecular dynamics simulation runs (MD_GU. MD_NU, PRS_U) shown in licorice representation: top view from the extracellular side, and two side views where the two sidechains orthogonal to the figure plane are not shown.

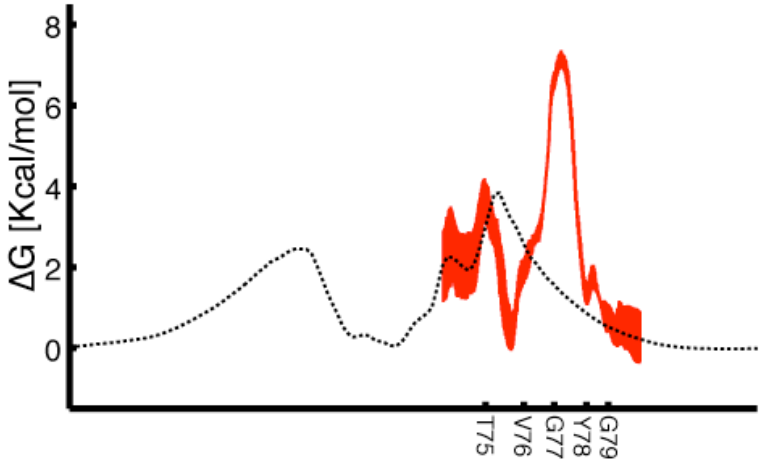

Figure 6-4. PMF of a water molecule along the channel axis, with no restrains on the selectivity filter.
Dotted line is used for the PMF defined according to the water density (Equation 6-3), continuous line is used for the PMF computed by umbrella sampling. The width of the line shows the standard deviation on the PMF (see Methods section). Ticks on the x-axis refer to the position of the carbonyl oxygen rings of each amino acid in the TVGYG motif, the x-axis goes from the intracellular to the extracellular compartment.

These characteristics of the potassium depleted SF were conserved also in the MD simulations denoted MD_NUP and MD_NUC. MD_NUP differs from MD_NU only in the membrane, which was made of POPC molecules in MD_NUP and octane molecules in MD_NUC. While MD_NUC and MD_NU differ only for the adopted channel model: closed in MD_NUC and open in MD_NU (Table 6-1). The average structure of the SF in MD_NUP was analogous to the average structure in MD_NU (RMSD of the backbone atoms below 1 Å), which suggests a marginal role of the membrane compositions on the SF structure. A higher difference emerged between the average structure of the SF in MD_NUC and MD_NU (RMSD of the backbone = 1.4 Å), but again the overall structure (two subunits with hourglass shape; closure between Val76 and Gly77) was preserved. The number of water molecules close to the SF did not show any sharp fluctuations in MD_NUP and MD_NUC, and no water fluxes through the SF

were observed in both the MD simulations (only one water molecule crossed the SF in MD_NUC).

Although no appreciable water flux across the SF was observed in the equilibrium MD simulations, they gave some insights into a possible mechanism for water transport. A few water molecules crossed the filter in equilibrium MD simulations (2 in MD_NU; 1 in MD_NUC). These water molecules did not move along the channel axis, but their trajectories protruded between two adjacent subunits of the SF. The PMF showed in Figure 6-4 refers to water movements along the channel axis. In the umbrella sampling calculations, water molecules are free to explore the plane perpendicular to the pore axis. However, alternative pathways situated behind the SF may be difficult to explore. If water molecules do not actually move along the actual pore, the PMF could exhibit artificially high energetic barriers. The existence of additional permeation pathways implies that the PMFs, do not fully describe water permeation through the filter region.

In order to simulate the water transport without previous assumptions on the water trajectories, the PRS_U simulation was run. Here, a pressure gradient across the SF is simulated, using the method proposed by Zhu et al. (Zhu, 2002) (see Methods section).

The stability of the SF was not affected by the applied pressure gradient (Figure 6-2). The average structure of the SF was close to the average structure revealed in MD_NU, but somewhat wider (Figure 6-3). The RMSD of the filter backbone atoms, between the MD_NU and the PRS_U average structures was ~1 Å. The number of water molecules within 3 Å of the filter backbone atoms increased from 13±2 in the equilibrium simulation (MD_NU) to 19±3 when the pressure gradient was applied. An increase in the number of water molecules in the channel as a result of the applied pressure gradient was previously observe in MD simulations of the Aqp1 channel (Zhu, 2002). The additional water molecules in PRS_U were located between adjacent subunits, and were crucial for water movements. As in

equilibrium MD simulations, the number of water molecules close to the SF did not show sharp fluctuations.

In the last 7 ns of the PRS_U simulation, 77 water molecules moved across the SF towards the extracellular side. A net flux of 77 water molecules in 7 ns with a 200 MPa pressure gradient corresponds to an osmotic permeability of 2.3×10^{-13} cm^3/s. This osmotic permeability is an order of magnitude higher than the one computed for the aquaporin channel Aqp1 by the same computational technique (7.1×10^{-14} cm^3/s) (Zhu, 2004), and it is still an order of magnitude smaller than the experimental value measured in KcsA (4.8×10^{-12} cm^3/s) (Saparov, 2004). Figure 6-5 shows the position of a water molecule that crosses the SF; all the snapshots of the PRS_U simulation are superimposed. As already revealed in equilibrium MD simulations, the water movement is not confined to the filter axis. While crossing the pore region, water molecules can squeeze between two adjacent subunits (Figure 6-6).

The simulation denoted PRS_UP (open channel model, in POPC bilayer, with unrestrained filter) gave similar results, both regarding the filter structure and the water fluxes. The average structure of the SF in PRS_UP has a RMSD for the backbone atoms of 1.2Å, both from the PRS_U and the MD_NU average structures of the SF. A net flux through the SF of 13 water molecules per nanosecond was observed, which corresponds to an osmotic permeability of $2.7 \times 10^{-13} cm^3/s$. In contrast, no water flux was observed in PRS_UC. In agreement with experimental data, the closed structure of the KcsA channel proved to be non-permeable by water. The average structure of the SF in PRS_UC was 1.4 Å far from the average structure in MD_NU. Again, this structure showed a narrowing of the SF pore between the aminoacids Val76 and Gly77, and the number of water molecules in its proximity did not show sharp fluctuations.

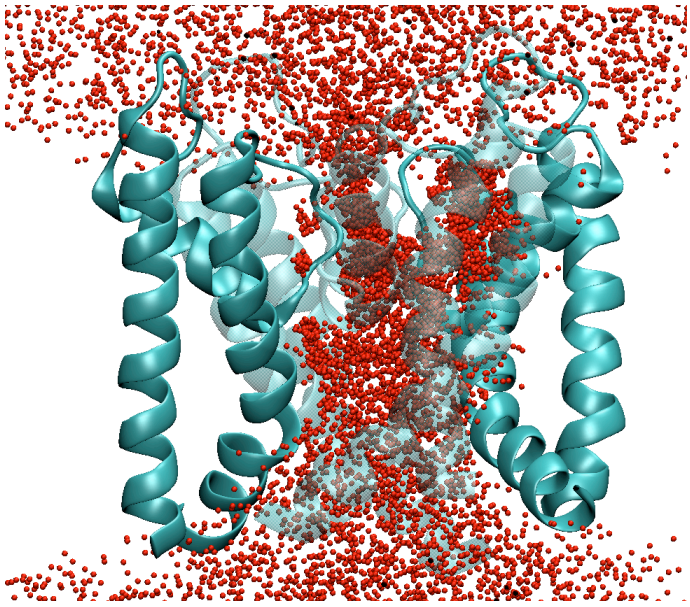

Figure 6-5. Trajectories of water molecules in the molecular dynamics simulation where a pressure gradient was applied and the selectivity filter was unrestrained (PRS_U).
Positions of the oxygen atoms of the water molecules crossing the SF are represented as spheres. All the snapshots are superimposed. The KcsA channel is shown in the cartoon modality the last snapshot is shown for simplicity. Using the last snapshot is justified as no appreciable changes occurred in the 8ns of simulation.

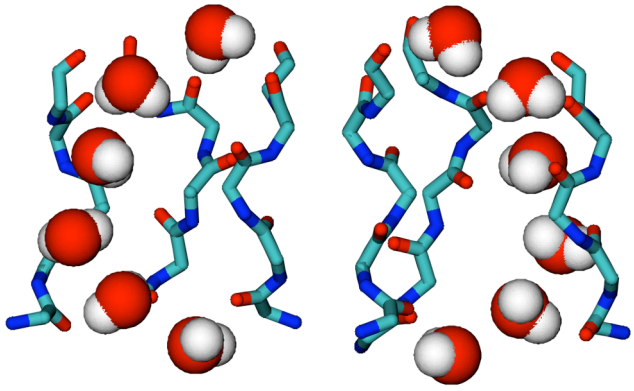

Figure 6-6. Trajectory of a water molecule crossing the selectivity filter.
Stereo-view of the trajectory of a water molecule traveling through the SF. For the sake of clarity only one snapshot of the protein is shown and the subunit in foreground is absence.

6.3.2 Restrained Selectivity Filter

As the "collapsed" SF failed to reproduce the experimental permeation coefficient of water, we also performed a set of simulations where the SF was artificially restrained to the X-Ray structure in high-K^+ concentration (Zhou, 2001). No water flux was observed at equilibrium regardless of the force field and water model adopted. In MD_GR (closed model, in POPC bilayer, with restrained filter) three water molecules were confined at S0, S1 and S2 binding sites; water molecules in S3 and S4 showing some transitions to S2 and S3. Water molecules also occupied the binding sites S3 and S4, but at these binding sites the water molecules frequently exchanged with the extracellular compartment. In MD_NR only the water molecule in S2 is confined to the binding site, while water molecules in S0/S1 and S3/S4 frequently exchanged with the intracellular and extracellular compartment respectively.

To further investigate the behaviour of water in the high-K^+ configuration of the SF, the PMF along the filter axis was computed (Figure 6-7). No significant energy barrier hampers the movement of water in the interior of the SF. The highest energy barrier is located at the intracellular entrance of the SF pore, both for the outward and the inward movements (7.8±0.4Kcal/mol and 5.0±0.5Kcal/mol respectively). The low water permeability of the SF in the high-K^+ configuration was also confirmed by the PRS_R simulation (open channel model, in octane slab, with restrained filter), where a pressure gradient of 200 MPa was applied across the filter. Despite this large pressure gradient, water movements through the filter were not observed in the 7ns MD. Three water molecules were confined at the binding sites S1, S2 and S3 for the whole trajectory. The artificial restraints on the SF prevent the transition to a collapsed state, which could open up a secondary permeation pathway behind the filter.

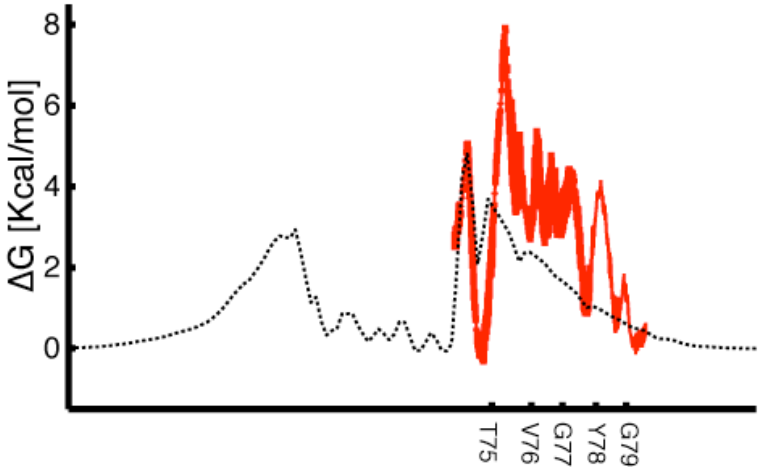

Figure 6-7. PMF of a water molecule along the axis of the closed KcsA channel, with the selectivity filter restrained to the potassium conductive configuration.
The dotted line shows the PMF calculated from the water density (Equation 6-3) and the continuous line denotes the PMF computed by umbrella sampling. The width of the line shows the standard deviation of the PMF (see Methods section). Ticks on the x-axis show the position along the channel axis of the carbonyl oxygens of the SF residues.

6.4 Discussion

Potassium channels evolved to transport potassium ions across the cell membrane. Thus, it is surprising the high osmotic permeability of the KcsA potassium channel. Indeed, according to experimental data by Saparov and Pohl (Saparov, 2004), water molecules move through KcsA 1,000 times faster than potassium ions. Transitions to vapor state were suggested as a possible mechanism responsible for the high osmotic permeability. MD simulations have already been used to describe liquid-vapor oscillations in nanopores (Beckstein, 2003), or more generally to analyze water transport in biological channels (de Groot, 2005). Here, MD simulations have been used to investigate water movements through the KcsA K^+ channel, in order to reveal the molecular basis of the high osmotic permeability. The major

conclusions are: i) the SF of the KcsA channel undergoes conformational changes in the absence of K^+ ions; ii) water molecules can flow at a high rate through KcsA, however, instead of doing it through the SF, they travel through paths behind it; iii) transitions to vapor state were not observed.

The relation between the filter structure and the concentration of potassium ions is a well established phenomenon (Zhou, 2001), which is confirmed by our simulations. Depletion of potassium ions caused severe structural rearrangements of the filter in all the MD simulations performed. The structure of the potassium depleted SF was sensible to the simulation set-up. However, the main characteristics of the potassium-free SF are conserved throughout the MD simulations. The filter is almost closed between the aminoacids Val76 and Gly76, and water molecules cannot move along the channel axis. All the results of the equilibrium MD simulations concur to define low water permeability along the SF axis, also confirmed by umbrella sampling calculations.

The unlikelihood of water translocation along the pore axis was the reason for performing the simulations in the presence of a pressure gradient. By means of this simulation technique, an unexpected pathway for high-rate water permeation in KcsA was identified. At a glance, the high water fluxes induced by the simulation of a pressure gradient seem inconsistent with the absence of any water flux in equilibrium MD simulations. This apparent contradiction is solved if the osmotic pressure acts as a stimulus, switching the filter from a non-permeable to a permeable state. Certainly, in the presence of a pressure gradient the SF structure widens slightly, and the number of water molecules around the filter increases. These structural changes are critical to allow permeation of water at high-rate trough the KcsA SF.

The computed osmotic permeability of KcsA, although larger than the permeability of some protein channels specialized in water transport, is still an order of magnitude lower than the experimental value proposed for KcsA.

Part of the discrepancy with the experimental data could be related to the degree of uncertainty of the experimental value. This uncertainty is mainly caused by difficulties in estimating precisely the number of ion channels per unit area. As an example, the osmotic permeabilities of the Aqp1 channel are in the range 1 to 16 × 10^{-14} cm^3/s (Heymann, 1999), which embrace the distance between our numerical result and the experimental data. Another reason for the discrepancies with the experimental data could be related to the limited time-scale of the MD simulations. On longer time scales, the SF may evolve towards a different structure, with higher osmotic permeability. Besides, in the MD simulations with the SF unrestrained and under a pressure gradient, water flow just between two adjacent subunits of the SF. KcsA is a tetrameric structure with axial symmetry, which suggests that an identical permeation pathway could exist between the other two subunits. The presence of various permeation pathways would obviously increase water fluxes through KcsA. This might be achieved if longer simulation time scales were accessible, which allows water to explore alternative pathways.

The length of the present simulations amounts over 100 ns, and throughout all the simulated time no fluctuation in the water density inside the SF has been observed. Even if the presence of liquid-vapor oscillations on a longer time scale cannot be ruled out, we are prone to exclude this phenomenon as the mechanism explaining the high osmotic permeability of KcsA. According to our results, transitions to vapor state in the SF of KcsA are rare events. It is unlikely for these rare events to sustain a high osmotic permeability.

The MD simulations presented here provide a detailed atomic description of water transport in KcsA. According to our results, structural rearrangements of the SF of KcsA take place in the absence of K^+ ions. Recent experimental data has revealed that the SF of potassium channels adjusts depending upon its functional states (Cordero-Morales, 2007; Zhou, 2001). Studying the KcsA channel in the absence of potassium ions could improve our

understanding on the structures accessible to the SF, and on their functional role in potassium channels.

Chapter 7

Oligomerization State of the α-Hemolysin Channel

In recent years α-Hemolysin has received great attention, mainly due to its possible usage as sensing element. In this chapter a study on the α-Hemolysin oligomerization state is presented. We measured the ion-currents through single α-Hemolysin channels, and confirmed the presence of two conductance levels, of (465 ± 30)pS and (280 ± 30)pS respectively. Different oligomerization state could be responsible for these two conductances. Actually, a heptameric structure of the channel was revealed by X-Ray crystallography, while atomic force microscopy (AFM) revealed a hexameric structure. Due to the low resolution of AFM, the atomic details of the hexameric structure are still unknown, and are here predicted by computational methods. A set of hypothetic atomic structures of the hexameric state were defined, and simulated by molecular dynamics. The conductances of these channel models were computed, by a numerical method based on the Poisson-Nernst-Planck electrodiffusion theory, and compared to experimental data. In this way, a model of the α-Hemolysin hexameric state with conductance characteristics consistent with the experimental data was identified. Since the oligomerization state of the channel may affect its behaviour as a molecular sensor, knowing the atomic structure of the hexameric state may be useful for the bio-technological applications of α-Hemolysin.

7.1 Introduction

α-Hemolysin is a pore forming toxin, which is secreted by the bacterium *Staphylococcus Aureus*, and is a major determinant of the bacterial pathogenicity (Bhakdi, 1991). In spite of the wide knowledge about the functioning and the structure of α-Hemolysin, the oligomerization state of the protein is still under debate. A heptameric structure was revealed by X-Ray crystallography (Song, 1996), while a hexameric structure was suggested according to Atomic Force Microscopy (AFM) data (Czajkowsky, 1998). Due to the low resolution of AFM, the atomic details of the hexameric structure are still unknown, and are here predicted by numerical simulations.

The interest in the atomic structure of the hexameric state is justified by the technological relevance of the α-Hemolysin channel. Several characteristics make α-Hemolysin an ideal candidate as sensing element in bio-technological applications. α-Hemolysin may bind directly to the molecules of a lipid membrane (i.e. phosphatidylcholine and cholesterol) (Ferreras, 1998; Meunier, 1997), and the binding does not require any auxiliary molecule, or special experimental conditions. Once bound to the lipid bilayer α-Hemolysin spontaneously oligomerizes to form a transmembrane channel (Valeva, 1997), and the open state of the channel is stable and highly conductive (Menestrina, 1986). The possible usage of α-Hemolysin as sensing element has already been demonstrated in various fields, including: i) sensing of divalent metal ions (Braha, 2000); ii) sensing of organic molecules (Gu, 1999); iii) analysis of single stranded RNA or DNA molecules (Kasianowicz, 1996); iv) detection of specific DNA or RNA sequences (Howorka, 2001). The oligomerization state may affect the affinity of the channel for blocking molecules, and consequently its function as a molecular sensor. In this context the knowledge of the atomic structure of the different oligomerization states will be useful.

The presence of two oligomerization states is supported by electrophysiological measurements. Current measurements in planar lipid bilayer reveled two distinct conductances for the α-Hemolysin channel (Belmonte, 1987), with a 1:1.5 ratio between the high and the low conductance value. The two conductances were associated to different oligomerization state of the channel protein.

Thanks to X-Ray crystallography a heptameric structure of the channel is known at atomic resolution (Song, 1996). In the crystallographic structure seven identical monomers are symmetrically arranged around the channel axis (Figure 7-1). The transmembrane domain of the channel has a β-barrel structure; each monomer contributing to the β-barrel by two anti-parallel β-sheets. The β-barrel pore is connected to the extracellular compartment, by a wide opening (CAP). Since the crystallographic structure of the α-Hemolysin channel was solved, this heptameric structure was associated to the high-conductance state of the channel. Numerical simulations by different approaches (Aksimentiev, 2005; Noskov, 2004b) confirmed this hypothesis. The association between the heptameric structure and the high-conductance state suggests the association between the low-conductance state and a hexameric structure. Actually, a hexameric state of α-Hemolysin was experimentally revealed by atomic force microscopy (AFM) in lipid bilayer (Czajkowsky, 1998).

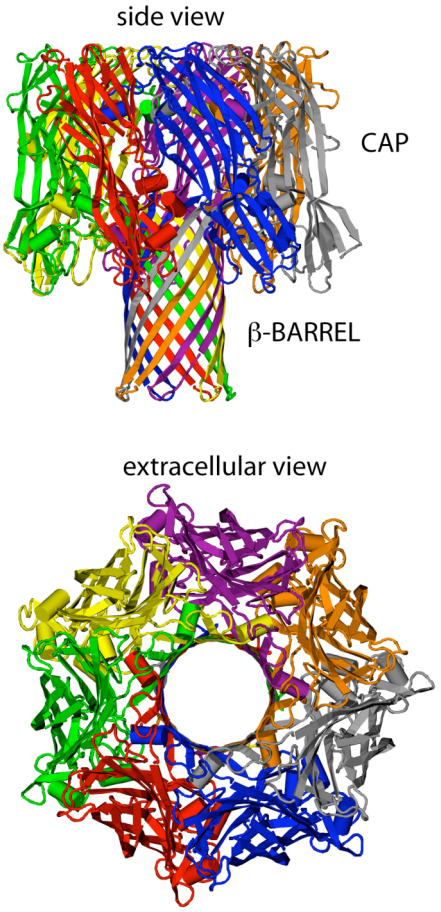

Figure 7-1 Heptameric structure of the αH channel
Side and top (extracellular) view of the αH channel in the heptameric state, in *cartoon* representation. Different colors are used for the seven monomers. The figure was generated with the molecular viewer software CHIMERA (Pettersen, 2004).

In order to identify the atomic structure of the α-Hemolysin channel in the hexameric state, we took advantage of the experimental data about the heptameric state (Song, 1996). We supposed that the overall structure of the channel is analogous in the heptameric and in the hexameric form. The symmetrical structure revealed by AFM supports this hypothesis. By analogy with the heptameric structure, the transmembrane pore of the hexameric channel would include 12 β-sheets, with each monomer providing a couple of anti-parallel sheets to the β-barrel. It is known that the hydrogen bond network and the packing of the sidechains restrict the admissible atomic structures in a β-barrel channel (Murzin, 1994a; Murzin, 1994b). According to these restrictions, we defined a set of atomic models for the

transmembrane pore of the hexameric α-Hemolysin channel. The conductances of these hypothetic structures were computed by an approach based on the Poisson-Nernst-Planck theory (Furini, 2006), and compared to experimental data. The analysis allowed identifying a model of the hexameric α-Hemolysin channel with conductance characteristics consistent with the experimental data.

7.2 Methods

7.2.1 Heptameric Channels

Atomic coordinates of the heptameric α-Hemolysin channel were taken from the crystallographic structure at 1.89Å resolution by Song et. al. (Protein Data Bank entry 7AHL) (Song, 1996). Residues with missing atoms in the X-Ray structure were built using the software *psfgen* of NAMD2 (Kale, 1999). The default protonation state was used for all the aminoacids. Histidines were protonated at the delta position. N and C terminals were respectively acetylated and amidated. The 818 water molecules of the crystallographic structure were included in the model.

The channel was embedded in a pre-equilibrated lipid bilayer, made up of 512 dimyristoylphosphatidylcholine (DMPC) molecules. Membrane was oriented in the x-y plane, and the α-Hemolysin pore was oriented along the z-axis. The hydrophobic belt of the α-Hemolysin β-barrel (aminoacids Tyr118-Gly126 and Ile132-Ile142) was centered in the lipid bilayer. DMPC molecules closer than 0.12nm to protein atoms were removed, together with crystallographic waters closer than 0.2nm to DMPC molecules. The system was solvate by 19395 water molecules. Potassium and Chloride ions were added to the water solution to reach a 150mM concentration, yielding a neutral system. The heptameric channel model based on the crystallographic

structure of α-Hemolysin will be refereed as HEPTA-CAP. The total system size was 142840 atoms.

A simplified model of heptameric α-Hemolysin was also defined (HEPTA-BARREL). This simplified model included only the β-barrel domain of the channel. The structure of the aminoacids Thr109-Val149 was modeled as in the HEPTA-CAP model, using analogous termini. The same procedure of the HEPTA-CAP model was used to insert the channel in the membrane, and to add water molecules and ions. The HEPTA-BARREL model included 12276 water molecules, 17 potassium ions, 17 chloride ions, and 118 DMPC molecules. The total system size was 54700 atoms.

7.2.2 Hexameric Channels

The β-sheet is one of the most common structural domains found in protein. In protein channels with a β-barrels structure, each β-sheet is bounded both to the previous and the next β-sheet in the sequence, by hydrogen bonds. The main geometrical features of a β-barrel are function of two parameters: the number of β-sheets (N) and the shear number (S). The shear number is defined as follow. Starting from the residue k in the first β-sheet, move perpendicularly to the strand around the barrel (H-bonds direction) until the first β-sheet is crossed again. If l is the residue at the intersection, the shear number is $|l-k|$ (Figure 7-2). Contiguous residues along a β-sheet have opposite orientation, while contiguous residues along the H-bond direction have the same orientation. As a consequence S is an even number.

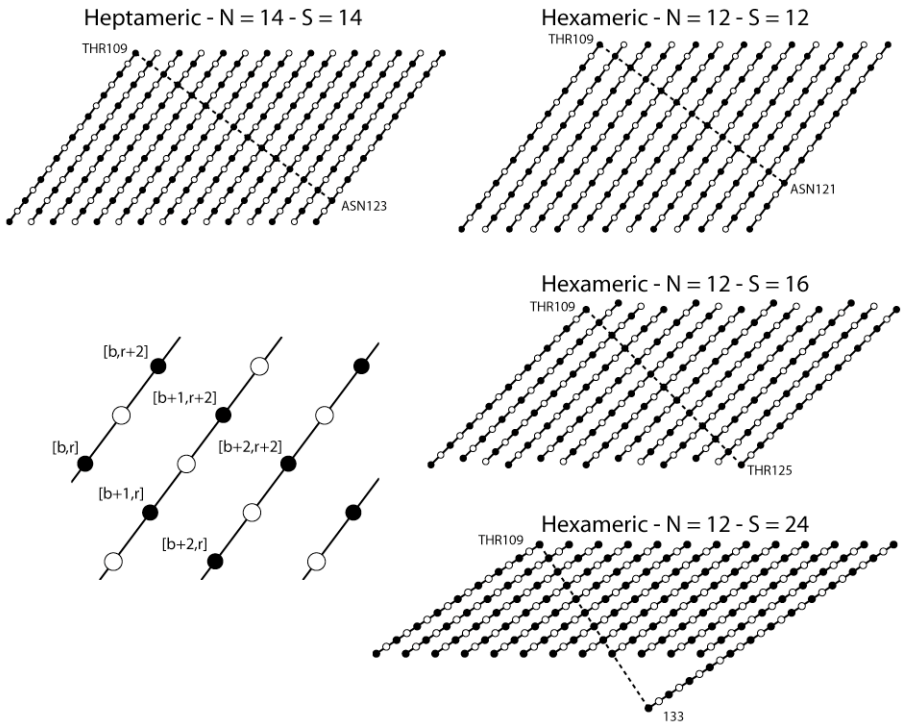

Figure 7-2 Unrolled β-barrel structures.
β-sheet arrangements in β-barrels are schematically shown, unrolling the β-barrel surface on a plane. Continuous lines show the β-sheet directions, empty circles are used for aminoacids pointing outward, and filled circles for aminoacids pointing towards the pore lumen. Dashed lines run orthogonal to the β-sheets on the β-barrel surface, and are used to define the sheer numbers (S). In the bottom-left picture the aminoacid nomenclature used in the text is defined.

The relation between the number of β-sheets and the shear number defines the packing of the aminoacids in the β-barrel. If b is defined as the β-sheet index and r as the residue index in the β-sheet, the residues closer to the residue $[b,r]$ are: $[b,r+2]$, $[b+1,r]$, $[b+1,r+2]$, $[b+2,r+2]$ (Figure 7-2). The distances among these residues are affected by N and S. In β-barrels with $S > 2N$ the sidechain of $[b,r]$ approaches the sidechain of $[b+2,r+2]$, due to high tilt angle of the β-sheets. Because of the short distance between residues $[b,r]$ and $[b+2,r+2]$, these structures are unlikely to be found. A

similar argument applies to β-barrel with $S < N$, where the low tilt angle brings the sidechains of residues $[b,r]$ and $[b+1,r]$ close together. Consequently, the β-barrel structures are usually characterized by $N \le S \le 2N$ (Murzin, 1994b). Simple geometrical criteria identify the $S = N + 4$ relation as the optimal one, with twist and coil angles of the β-sheets closest to optimal values (Murzin, 1994a).

The β-barrel of the hexameric α-Hemolysin channel has 6 couples of anti-parallel β-sheets, one couple from each subunit ($N = 12$). Four different starting structures were generated with $S = 12$, $S = 16$, $S = 20$ and $S = 24$ respectively. The alpha-carbons (C^{α}) were placed on a cylindrical surface with radius (R) defined by:

$$R = \frac{d_H}{2\sin\left(\frac{\pi}{N}\right)\cos(\alpha)}$$

$$\alpha = \tan^{-1}\left(\frac{Sd_C}{Nd_H}\right)$$

Equation 7-1

ere d_H is the distance between consecutive, set to 0.44nm; d_C is the C^{α}- C^{α} distance along the β-sheet, set to 0.33nm; and α is the β-sheet tilt angle with respect to the channel axis. Each strand included 17 C^{α} atoms. Residues in odd β-sheets were numbered from 109 to 126; residues in even β-sheets were numbered from 132 to 149 in the opposite direction. Each number identifies the α-Hemolysin residues to be modeled. C^{β} atoms were added to each residue, excluding glycines. The direction of C^{β} atoms interchanged along the β-sheets, with consecutive residues having C^{β} atoms alternating inwards and outwards (residues Thr109 and Ile132 pointed respectively inward and outward, as in the heptameric structure of α-Hemolysin). The remaining backbone heavy-atoms were added to each residue on a plane

tangent to the β-barrel surface. The heptameric structure of α-Hemolysin was exploited to model the atomic structure in the hexameric oligomerization state. The *i-th* residue of the heptameric structure was moved to the analogous residues in the hexameric structure, using the C^{β} atom and the backbone atoms for the fitting. The new atom positions were used to define residue *i* in the hexameric structure. The procedure was repeated for all the monomers in the hexameric structure. Then, Residues Asp127-Lys131 of the heptameric structure where moved, using residue Gly126 and Ile132 for the fitting, to define the intracellular loops between β-sheets.

Each hexameric model was embedded in a DMPC lipid bilayer and solvated using the same procedure described before. Labels HEXA-S12, HEXA-S16, HEXA-S20 and HEXA-S24 will be used for the various hexameric models with sheer number, respectively 12, 16, 20 and 24.

7.2.3 Molecular Dynamics

The same protocol was used for the molecular dynamics (MD) simulation of all the molecular models (HEPTA-CAP; HEPTA-BARREL; HEXA-S12; HEXA- S16; HEXA-S20; HEXA-S24). Energy was first minimized by a steepest descent procedure (10000 steps), followed by an equilibration period (500ps) where harmonic potentials were applied to the backbone atoms of the protein (force constant set to $4 Mcalmol^{-1}nm^{-2}$). Harmonic restraints on protein atoms were then removed, and unrestrained MD was run for 4ns in the NPT ensemble.

The MD simulations were performed using the NAMD2 software (Kale, 1999). The CHARMM27 force field (MacKerell, 1998) was used for protein and lipids, together with the TIP3 model for water molecules (Jorgensen, 1983). Periodic boundary conditions were adopted and the long-range electrostatic interactions were treated by the Particle Mesh Ewald algorithm (Essmann, 1995). A 1.2nm smoothed cutoff was used for the Van der Waals

interactions. Hydrogen bonds lengths were fixed by the SHAKE algorithm (Ryckaert, 1977), in order to use a 2fs time step. The temperature was controlled by the Langevin algorithm at 300K, with a damping coefficient of $5ps^{-1}$. Pressure was kept at 1atm by the Nose-Hoover Langevin piston pressure control (Feller, 1995), with a piston period of 200fs, and a damping time constant of 100fs.

7.2.4 Poisson-Nernst-Planck Parameters

PNP equations were solved on a cylindrical grid, having the z-axis along the channel axis. The grid length was 13nm in the axial direction, and 6nm in the radial direction. The number of grid points was 130 in the axial direction, 120 in the radial direction, and 72 in the angular direction. Partial atomic charges were from the CHARMM27 force field. Atomic radii were defined according to the value proposed by Nina et al. (Nina, 1997). Relative dielectric constant was set to 2 for the protein, and 80 for the solution. A waterproof slice was placed around the channel, orthogonally to the pore. This slice was introduced to mimic the lipid bilayer; its relative dielectric constant was set to 2 and its width to 2.9nm. The center of the slice was set to the center of the hydrophobic belt of α-Hemolysin (aminoacids Tyr118-Gly126 and Ile132-Ile142).

Outside the channel the diffusion coefficients were set to the experimental values for diffusion in free solution ($D_{K^+} = 1.96 \times 10^{-9}$ m^2/s and $D_{Cl^-} = 2.03 \times 10^{-9}$ m^2/s (Lide, 2004)). Diffusion coefficients were reduced inside the channel, to take into account the confinement effects due to the pore finite size. The analytical expression proposed by Noskov et al. (Noskov, 2004b) was used to define the diffusion coefficients on each slice of the cylindrical grid inside the channel:

$$D = \frac{D_{bulk}}{6.43*10^{-1} + 4.40*10^{-4} e^{\frac{R_{ion}}{0.069R_{pore}}} + 3.56*10^{-1} e^{\frac{R_{ion}}{0.19R_{pore}}}}$$ **Equation 7-2**

Where R_{pore} is the radius of the pore; R_{ion} is the radius of the diffusing ion; D_{bulk} is the diffusion coefficient in free solution; and the numerical values were obtained fitting the diffusion coefficients of spherical particles in cylindrical pores by Paine and Scherr (Paine, 1975).

PNP equations were solved by an iterative algorithm (see section 2.4), with a tolerance of 10^{-10}mV for the Poisson equations, and 10^{-10}mM for the Nernst-Planck equation. In order to take into account the movements of the protein, PNP calculations were repeated on several snapshots of the molecular dynamic trajectories. The selected structures were from the last 3ns of the MD trajectories, sampling the trajectory every 0.5ns.

7.2.5 Experimental Measurements

The planar lipid bilayer workstation from Warner Instrument was used for single channel recording. The bilayer apparatus consists of two chambers (1ml each), connected by a 150μm orifice through a Delrin® cap. Lipid bilayers of α-phosphatidylcholine were formed by the painting method, using a diluted phosphatidylcholine solution in decane (15mg/ml). Ag/AgCl electrodes connected the bathing solutions to the recording systems. The electrode in the *cis* chamber - where α-Hemolysin was added - was connected to the virtual ground. A positive potential indicates a higher potential in the *trans* chamber, and positive currents flew from *trans* (intracellular side of the channel) to *cis* (extracellular side of the channel). Bathing solutions contained 0.5M KCl, 10mM EGTA, 10mM HEPES (pH 7.5 with KOH). Signals were recorded with an Axopatch 200B amplifier, and data were analyzed by pCLAMP 9 (Axon Instruments Inc, Union City, CA, USA). Signals were sampled at 10KHz and filtered at 5 kHz, by a 4-

pole low-pass Bessel filter. Experiments were conducted at a room temperature of 20 ± 2ºC. All the reagents were from Sigma, Milan, Italy.

7.3 Results

7.3.1 Molecular Dynamic Simulations

Both the heptameric channel models (HEPTA-CAP and HEPTA-BARREL) proved to be stable for the 4ns MD trajectories (Figure 7-3). Removing the extracellular cap did not affect the structural stability of the β-barrel domain. The higher root mean square deviation (RMSD) of the backbone atoms showed by the HEPTA-BARREL model is mostly due to atomic movements at the extracellular side, where N and C terminal aminoacids gain mobility as a consequence of the extracellular cap removal.

The moment of inertia tensor of the β-barrel domain was used to evaluate the geometrical features of the pore, namely the tilting of the pore respect to the lipid membrane and the eccentricity of the β-barrel cross-section. As a consequence of the cylindrical structure of the β-barrel, a principal axis of inertia is directed along the pore axis. The angle between this principal axis and the z-axis measures the tilting of the channel with respect to the lipid membrane. The pore axis was aligned to the z-axis in the starting structure, and no drift in the tilt angle was observed in the 4ns trajectories. The maximum tilt was below 5 degrees, in both of the heptameric models. To estimate the cross-section eccentricity, the inertia moments along the principal axes orthogonal to the pore were used. The ratio between the minor and the major of these two inertia moments is 1 in a β-barrel with circular cross-section, while it decreases in a β-barrel with elliptical cross-section. The mean ratio was 0.97 in both the heptameric channel models, which points out an almost circular cross-section. A cross-section more asymmetrical, but again close to circular, was observed by Aksimentiev et al.

in a 50ns MD simulation of α-Hemolysin (Aksimentiev, 2005) (ratio between inertia moments around 0.9). The longer simulation and the different method used to estimate the cross-section asymmetry may explain the difference.

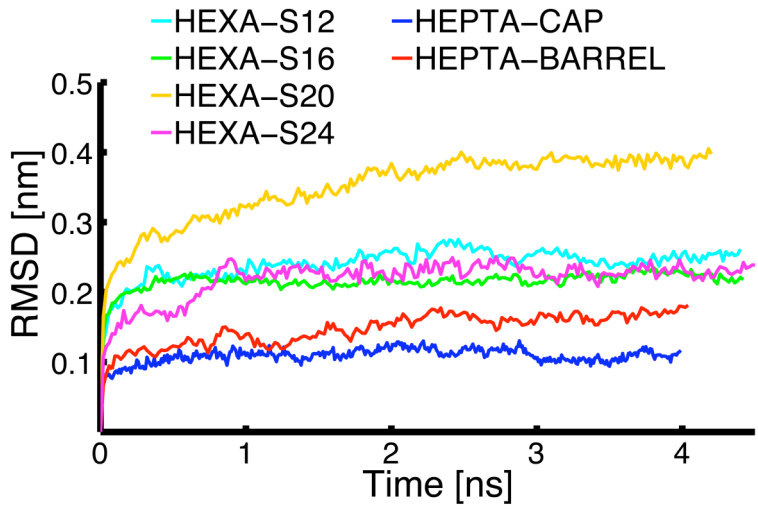

Figure 7-3 Root Mean Square Deviation of β-barrel domain
Root mean square deviation was computed on the backbone atoms of residues from Thr109 to Val149.

The number of hydrogen bonds in the β-barrel backbone was compared between the two heptameric models. Donor and acceptor atoms were counted as involved in a hydrogen bond when their distance was below 0.4nm and the angle donor-hydrogen-acceptor between 160 degrees and 200 degrees (Mills, 1996). The mean number of hydrogen bonds was 180 and 172 in the HEPTA-CAP and HEPTA-BARREL models respectively. The greater mobility on the extracellular side causes the reduction in the number of hydrogen bonds in the HEPTA-BARREL model.

The four hexameric models (HEXA-S12, HEXA-S16, HEXA-S20 and HEXA-S24) were stable for the 4ns MD simulations (Figure 7-3). The tilting of the pore with respect to the membrane and the asymmetry of cross-section were analyzed as described for the heptameric models. The pore axis was

orthogonal to the lipid membrane in the channel models HEXA-S12 and HEXA-S16, with maximum deviations below 3 degrees. A higher deviation was observed both in the HEXA-S20 model (around 14 degrees), and in the HEXA-S24 model (around 10 degrees). The cross-section was almost circular in the HEXA-S12 and HEXA-S16 models (ratio between the inertia moments equals to 0.98 in both the models). The cross-section asymmetry was more pronounced in the HEXA-S20 and HEXA-S24 models (ratio equals to 0.88 and 0.85 respectively). The mean number of hydrogen bonds was 120 in the HEXA-S20 model, and close 140 in HEXA-S12, HEXA-S16 and HEXA-S24. This number of hydrogen bonds corresponds to a 57% of oxygen backbone atoms involved in hydrogen bonds. The same percentage of backbone oxygen atoms is involved in hydrogen bonds in the HEPTA-BARREL model.

7.3.2 Channel Conductances

Experimental measurements in 0.5M KCl revealed two different current-voltage relations for the α-Hemolysin channel. Data were associated to the high or low conductance state according to the conductance at 40mV, using a value of 400pS as threshold level. The high and low conductances at 40mV were (465 ± 30)pS and (280 ± 30)pS (Figure 7-4). The current-voltage relations of α-Hemolysin are slightly asymmetric, with higher conductance at positive membrane potential. The ratio between the channel conductances at +40mV and -40mV is 1.2, both for the high and the low conductance state.

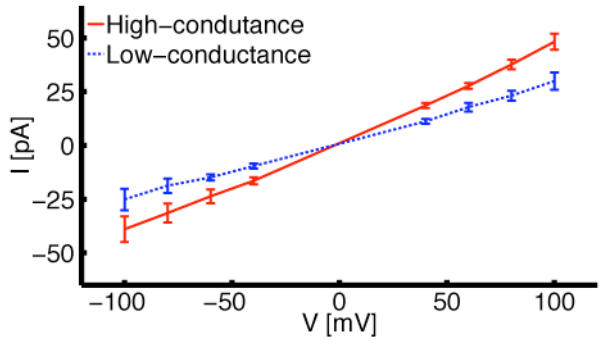

Figure 7-4 Experimental α-Hemolysin currents in 0.5M KCl symmetric solutions
Single channel currents in the high (continuous red line) and low (dotted blue line) conductance state of the α-Hemolysin channel. Mean values and standard deviations were defined using 10 independent measurements.

The PNP approach provided a channel conductance of (680±25)pS for the HEPTA-CAP model (membrane potential set to 40mV), which overestimated the high-conductance value by 1.5 fold (Figure 7-5). The mean value and the standard deviation were computed repeating the PNP calculations on different snapshots of the MD simulation. The low standard deviation proves that the specific snapshot does not affect the results, which justifies the usage of the PNP steady-state model.

The asymmetry in the current-voltage relation was well reproduced by the PNP approach. The ratio between the computed channel conductances at +40mV and -40mV is 1.2, in agreement with the experimental data. Moreover, the computation method properly reproduced the selectivity of the α-Hemolysin channel. The HEPTA-CAP model was slightly selective to anions, having a ratio between cationic and anionic fluxes equal to (0.77±0.18). In order to better estimate the selectivity, channel currents were computed in presence of concentration gradients, and the reversal potentials were then estimated. The reversal potential is related to the channel selectivity by the Goldman-Hodgkin-Katz equation:

$$V_{rev} = \frac{kT}{e} \ln\left[\frac{P_K[C]_e + P_{Cl}[C]_i}{P_K[C]_i + P_{Cl}[C]_o}\right] \qquad \textbf{Equation 7-3}$$

Where P_K and P_{Cl} are the permabilities to potassium and chloride ions; and $[C]_e$ and $[C]_i$ are the ionic concentrations in the extracellular and intracellular compartments. The reversal potential was -3.4mV with $[C]_e = 1\text{M}$ and $[C]_i = 0.2\text{M}$ ($P_K / P_{Cl} = 0.8$); and +5.6mV with $[C]_e = 0.2\text{M}$ and $[C]_i = 1\text{M}$ ($P_K / P_{Cl} = 0.7$). Under the same conditions, Gu et al. experimentally measured a reversal potential of -3.7mV and +9.1mV respectively.

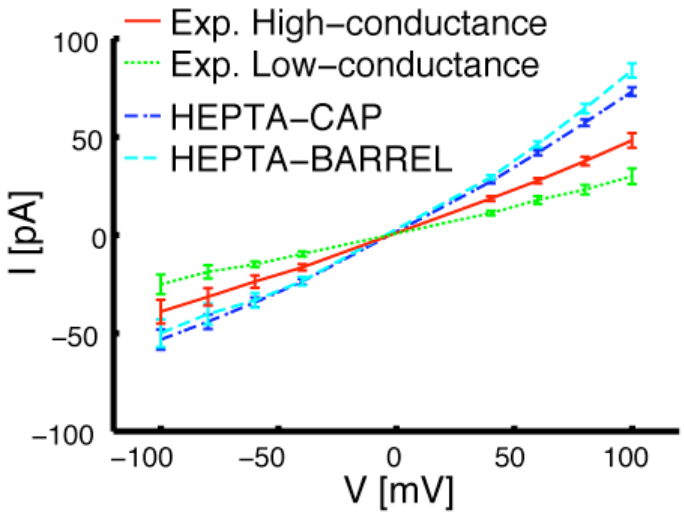

Figure 7-5 Current-Voltage relations in the high-conductance state
The figure shows the experimental currents of the high-conductance state (continuous red line), and the computed currents in the HEPTA-CAP model (dotted blue line), and in the HEPTA-BARREL model (dashed green line). Mean values and standard deviations of the computed currents were defined using 6 different snapshots of the MD simulations. Potassium and chloride concentrations in the intracellular and extracellular compartments were 0.5M, both for the experimental and the numerical data.

The analysis of the HEPTA-BARREL model provided analogous results. Minor changes were observed in the channel conductance, current-voltage relation and in the channel selectivity (Figure 7-5;
Table 7-1). Since removing the extracellular domain did not strongly affect the computed currents, the theoretical conductance of the hexameric models, lacking the extracellular cap, can be compared to the experimental data on the low-conductance state.

The hexameric models (HEXA-S12, HEXA-S16, HEXA-S20, and HEXA-S24) showed very different conductivity (Figure 7-6). The ionic currents through the HEXA-S20 and HEXA-S24 models overestimate the experimental data, respectively by 3 and 7 folds; while the HEXA-S12 model underestimates the experimental data. The HEXA-S16 model shows good agreement with the experimental low-conductance value. The predicted conductance at 40mV was (370 ± 25)pS, which overestimates the low-conductance experimental value by 1.3 folds. It is noteworthy that the HEPTA-BARREL model overestimates the experimental high-conductance by a similar amount (1.5 folds).

	HEPTA-CAP	**HEPTA-BARREL**	**HEXA-S16**
G_{+40} [pS]	680 ± 25	730 ± 30	370 ± 25
G_{+40}/G_{-40}	1.2 ± 0.1	1.3 ± 0.1	1.1 ± 0.1
J_+/J_-	0.77 ± 0.18	0.79 ± 0.10	0.63 ± 0.14

Table 7-1 Conduction characteristics
G_{+40} and G_{-40} are the channel conductance with a membrane potential of +40mV and -40mV respectively. J_+ and J_- are the cationic and anionic currents.

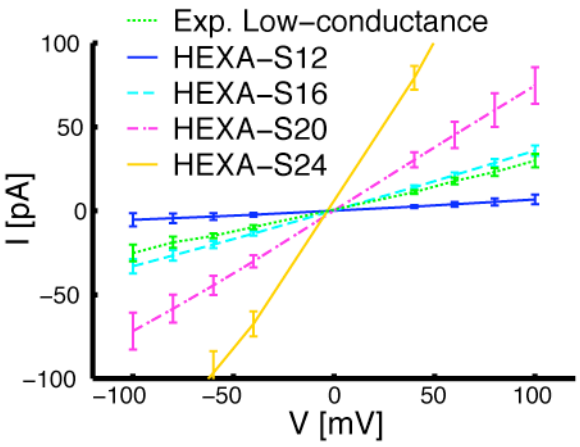

Figure 7-6 Current-Voltage relations in the low-conductance state
The figure shows the experimental currents of the low-conductance state (continuous red line), and the computed currents in the HEXA-S12 model (dotted blue line), HEXA-S16 model (dashed green line), HEXA-S20 model (dot-dashed light blue line), and HEXA-S24 model (continuous yellow line). Mean values and standard deviations of the computed currents were defined using 6 different snapshots of the MD simulations. Potassium and chloride concentrations in the intracellular and extracellular compartments were 0.5M, both for the experimental and the numerical data.

The current-voltage relation of the HEXA-S16 model is slightly asymmetric, in agreement with the experimental results, and the anionic selectivity is somewhat higher than in the heptameric models (
Table 7-1). The reversal potential was -9.1mV with $[C]_e = 1\text{M}$ and $[C]_i = 0.2\text{M}$ ($P_K / P_{Cl} = 0.6$); and +7.9mV with $[C]_e = 0.2\text{M}$ and $[C]_i = 1\text{M}$ ($P_K / P_{Cl} = 0.6$). The tighter packing of the charged residues in the HEXA-S16 model, compared to the heptameric models, justifies the higher anionic selectivity.

The electrostatic potential and the ion distributions inside the channel were analyzed, in order to compare the HEPTA-CAP, the HEPTA-BARREL and the HEXA-S16 models (Figure 7-7). In all the channel models, the change in the electrostatic potential is confined to the extracellular and the intracellular entrances of the β-barrel domain. Far from these regions, the electrostatic

potential is almost constant. In the heptameric models the most noticeable characteristic in the ion distribution is the potassium depletion, and the chloride enrichment, at the extracellular entrance of the β-barrel domain. This characteristic is preserved both in the HEPTA-CAP and in the HEPTA-BARREL model. The strong similarity in electrostatic potential and ion distributions between the heptameric models supports the hypothesis that the β-barrel domain is the major determinant of the conduction characteristics, while the extracellular cap plays a minor role.

The HEXA-S16 differs from the heptameric models in the electrostatic potential and ion distributions inside the channel (Figure 7-7). The chloride concentration is higher in HEXA-S16, both at the extracellular and at the intracellular entrances of the β-barrel, and the potassium depletion from these regions is stronger. These characteristic correlates with the higher anionic selectivity of the HEXA-S16 model. The different electrostatic potential and ion distributions inside the channel may affect the interaction with blocking molecules.

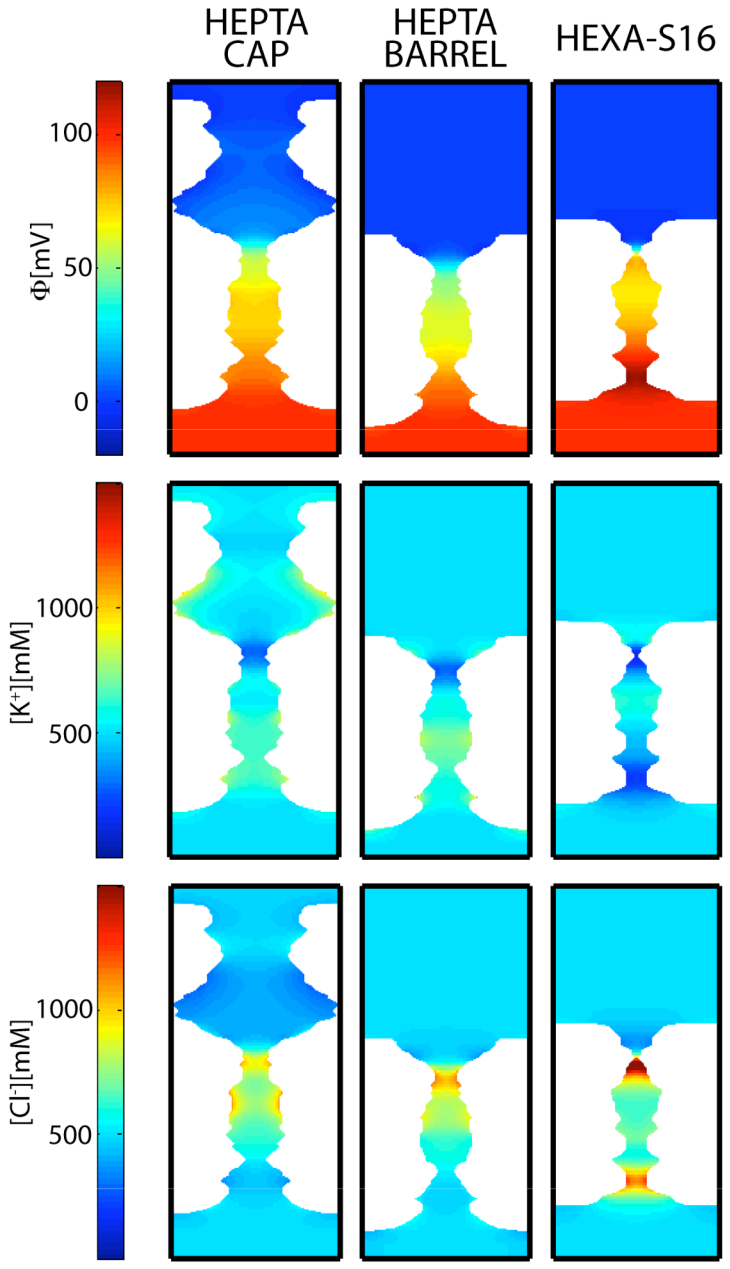

Figure 7-7 Electrostatic potential and ion distributions.
The electrostatic potential on a longitudinal section of the channel is shown. Membrane potential is set to +100mV; extracellular and intracellular ion concentrations to 500mM.

7.4 Discussion

The α-Hemolysin channel may exist in different oligomerization states, namely heptameric and hexameric. While the atomic structure of the heptameric state was solved by X-Ray crystallography, the hexameric structure is known only at low resolution. Thanks to the β-barrel architecture of the transmembrane domain, a set of possible atomic structure of the hexameric channel was defined. The conduction characteristics of these hypothetic structures were determined by computational methods, and compared to experimental data. The experimental conductance was well reproduced by the hexameric model with sheer number equal to 16, which we propose as the atomic structure of the α-Hemolysin channel in the hexameric state.

To compute the channel conductance a simplified approach based on the PNP theory, was preferred to more accurate methodologies, like MD simulations. In MD no arbitrary parameter – except the adopted force field - is used, and the atomistic motions involved in the conduction process are fully described. The experimental conductance of the α-Hemolysin channel has been estimated by Aksimentiev et al. through MD simulations, and the atomistic details of the conduction process were revealed (Aksimentiev, 2005). The counter-price of this atomistic detail is the high computational load. The problem is particularly severe in the present case, where the conduction characteristics of several channel models need to be compared. The usage of a computational method based on the PNP equations widely decreases the computational load, allowing a comparison between different channel models at different boundary conditions (membrane potential and ion concentrations).

Nevertheless, the PNP approach suffers from two main shortcomings: i) ions are described by a continuum distribution, ignoring their discrete nature; and ii) the atomic motions in the channel protein are neglected. In order to value

the role of atomic motions on the channel conductance, the PNP calculations were repeated on several snapshots of the MD trajectories. The methodology used to compute the channel conductance was first tested in the hexameric α-Hemolysin channel. In both the heptameric models, with and without the extracellular cap, the PNP approach overestimates the experimental high-conductance value by 1.5 folds, in agreement with previous results by Noskov et al. (Noskov, 2004b). However, it is important to remark that: i) no parameter was used to fit the experimental data; and ii) the linearization of the current-voltage relation and the channel selectivity are well reproduced. Besides, the purpose of the present study was to identify the hexameric structure of the α-Hemolysin channel, not to validate the PNP approach. In this context, the overestimation of the experimental conductance is partially irrelevant. Once the overestimation is known, the same overestimation will be expected in the hexameric models. The low-sensitivity of the PNP results to the specific MD snapshots, together with the agreement with the selectivity and linearization experimental data, suggest that the PNP approach provides a reliable description of conduction in the α-Hemolysin channel, and that can be used to analyze the hexameric models.

The analysis of the hexameric structures was focused on the β-barrel domain, since the conduction characteristics of the α-Hemolysin channel are mainly governed by this domain, as proved both by experimental data (Gu, 2001; Gu, 2000), previous computational analyses (Misakian, 2003; Noskov, 2004b), and our results on the HEPTA-CAP and the HEPTA-BARREL models. The β-barrel domain is not only crucial for the conduction proprieties; it also plays an important role in the channel interaction with several compounds, i.e. cyclodextrin. The pivotal role of the β-barrel domain justifies the restriction of the modeling to this region.

The hexameric models proved to be stable in a 4ns MD simulation. The temporal scale of the MD simulation does not allow a comparison on the energetic stability of the different channel structures. According to MD data,

all the hexameric models are equally stable. The calculation of the channel conductances allowed discrimination among the hexameric models. The hexameric model with sheer number equal to 16 was the one in better agreement with the experimental data. Noteworthy is the fact that the overestimation of the low-conductance value by the HEXA-S16 model is similar to the overestimation of the high-conductance value by the heptameric channel models, which strengthens the identification of the HEXA-S16 model as the proper structure of the hexameric α-Hemolysin channel.

A different structure of the hexameric α-Hemolysin channel, with sheer number equal to 12, was proposed by Smart et al.(Smart, 1998), according to experimental data by Korchev et al.(Korchev, 1995). In (Korchev, 1995) a 1:10 ratio between the low and the high conductance value is suggested. On the contrary, our experimental data show a 1:1.5 ratio, in accordance with previous results by Menestrina (Menestrina, 1986). The high and low conductances revealed in our measurements refereed to different channels. Once a channel enters in the lipid membrane, it showed a specific conductance (high or low) and no transitions to a different value were observed. This behavior is consistent with the idea that the channel may enter in the membrane in different oligomerization states, characterized by different conductances. A different protocol was used by Korchev et al. (Korchev, 1995). They measured the current through a single ion channel, and they revealed changes in the channel conductance. Since the high and low conductance values refer to the same ion channel, it is unlikely they are related to different oligomerization states. A change in the oligomerization state requires breaking and recreating a high number of hydrogen bonds, which is unlikely to occur once the channel is inserted in the lipid membrane. The high and low conductance values showed in (Korchev, 1995) are more likely related to different functional states of the channel, not to different oligomerization states.

The PNP approach allowed analyzing the current-voltage relation and the selectivity of the hexameric channels. As expected, these were very similar to the analogous properties of the heptameric channel. A slight increase in the channel selectivity was revealed. This increment is too small to be experimentally tested, but it suggests a different behaviour of hexameric and heptameric channels, which could also play a role in the affinity of the channel to blocking molecules. Studying these differences could help to further characterize the hexameric state, and may be useful for the usage of α-Hemolysin as sensing element in bio-technological application.

APPENDIX A: PSEUDO-CODE OF THE POISSON-NERNST-PLANCK NUMERICAL SOLVER

A.1. Partial Differential Equation Solver

A,b,x	Matrix and arrays of the linear system Ax=b
x_0	First trial solution
TOL	Required tolerance for the linear system solution
MAX_IT	Maximum number of iterations

^{T} is used for the transpose, and || for the norm

int **Solve**(A,b,x_0,x) {
    r_0=b-Ax_0;
    for (i=1; i<MAX_IT; i++)
        rho_{i-1}=$r_0^T r_{i-1}$;
        if rho_{i-1} == 0 return 1; /*ERROR*/
        if (i == 1)
            p_i=r_{i-1};
        else
            $beta_{i-1}$=(rho_{i-1}/rho_{i-2})($alpha_{i-1}$/w_{i-1});
            p_i=r_{i-1}+$beta_{i-1}$(p_{i-1}-$w_{i-1}v_{i-1}$);
        end if
        v_i=Ap_i;
        $alpha_i$=rho_{i-1}/($r_0^T v_i$);
        s=r_{i-1}-$alpha_i v_i$;
        if (|s|<TOL)
            x_i=x_{i-1}+$alpha_i p_i$;
            return 0; /*SOLUTION REACHED*/
        end if
        t=As;
        w_i=($t^T s$)/($t^T t$);
        x_i=x_{i-1}+$alpha_i p_i$+w_is;
        r_i=s-w_it;
        if (|r_i| < TOL) return 0; /*SOLUTION REACHED*/
    end for
}

A.2. Iterative Algorithm

A_P, b_P	Matrix and arrays of the linear system ($A_P x_P = b_P$) associated with the Poisson equation
A_K, b_K, K_{NP}	Matrix and arrays of the linear system ($A_K K_{NP} = b_K$) associated with the Nernst-Planck equation for potassium ions
A_C, b_C, C_{NP}	Matrix and arrays of the linear system ($A_C C_{NP} = b_C$) associated with the Nernst-Planck equation for chloride ions
ϕ_i, K_i, C_i	Electrostatic potential, potassium concentrations and chloride concentration and the i-th iteration step
w_P, w_{NP}	Updating-weight of the Poisson and Nernt-Planck equations

$\phi_0 = K_0 = C_0 = 0$;
for(i=1; i<MAX_IT; i++)

/*Updating of the Poisson linear system*/
UpdatePoisson(K_{i-1}, C_{i-1}, b_P);
/*Solution of the Poisson equation*/
Solve($A_P, b_P, \phi_{i-1}, \phi_P$);
/*Updating electrostatic potential*/
$\phi_i = (1-w_P)\ \phi_{i-1} + w_P \phi_P$;

/*Updating Nernst-Planck linear system*/
UpdateNernst($\phi_i, A_K, b_K, A_{Cl}, b_{Cl}$);
/*Solution of the Nernst-Planck equations*/
Solve($A_K, b_K, K_{i-1}, K_{NP}$);
Solve($A_{Cl}, b_{Cl}, C_{i-1}, C_{NP}$);
/*Updating potassium and chloride concentrations*/
$K_i = (1-w_{NP})\ K_{i-1} + w_{NP} K_{NP}$;
$C_i = (1-w_{NP})\ C_{i-1} + w_P C_{NP}$;

/*Convergence test*/
If (($|\phi_i - \phi_{i-1}| < TOL$) and ($|K_i - K_{i-1}| < TOL$)
and ($|C_i - c_{i-1}| < TOL$))
return 0; /*SOLUTION REACHED*/
end

References

Aiay, A.; Murcko, M.A. Computational methods to predict binding free energy in ligand-receptor complexes Journal of Medical Chemistry **1995**, 38, 4953-4967.

Aksimentiev, A.; Schulten, K. Imaging {alpha}-Hemolysin with Molecular Dynamics: Ionic Conductance, Osmotic Permeability, and the Electrostatic Potential Map Biophysical Journal **2005**, 88, 3745-3761.

Alberts, B. *Molecular biology of the cell*, 5th ed.; Garland Science: New York, 2008.

Alcayaga, C.; Cecchi, X.; Alvarez, O.; Latorre, R. Streaming potential measurements in Ca2+-activated K+ channels from skeletal and smooth muscle. Coupling of ion and water fluxes Biophys. J. **1989**, 55, 367-371.

Allen, T.W.; Andersen, O.S.; Roux, B. On the Importance of Atomic Fluctuations, Protein Flexibility, and Solvent in Ion Permeation The Journal of General Physiology **2004**, 124, 679-690.

Allen, T.W.; Kuyucak, S.; Chung, S.H. Molecular Dynamics Study of the KcsA Potassium Channel Biophysical Journal **1999**, 77, 2502-2516.

Allen, T.W.; Kuyucak, S.; Chung, S.H. Molecular dynamics estimates of ion diffusion in model hydrophobic and KcsA potassium channels Biophysical Chemistry **2000**, 86, 1-14.

Aqvist, J.; Luzhkov, V. Ion permeation mechanism of the potassium channel Nature **2000**, 404, 881-884.

Barrett, R.; Berry, M.; Chan, T.F.; Demmel, J.; Donato, J.; Dongarra, J.; Eijkhout, V.; Pozo, R.; Romine, C.; Van der Vorst, H. *Templates for the Solution of Linear Systems: Building Blocks for Iterative Methods*, 2nd ed.; SIAM: Philadelphia, PA, 1994.

Baukrowitz, T.; Yellen, G. Modulation of K+ current by frequency and external [K+]: A tale of two inactivation mechanisms Neuron **1995**, 15, 951-960.

Beckstein, O.; Sansom, M.S.P. Liquid-vapor oscillations of water in hydrophobic nanopores Proceedings of the National Academy of Sciences **2003**, 100, 7063-7068.

Belmonte, G.; Cescatti, L.; Ferrari, B.; Nicolussi, T.; Ropele, M.; Menestrina, G. Pore formation by Staphylococcus aureus alpha-toxin in lipid bilayers. Dependence upon temperature and toxin concentration. Eur Biophys J. **1987**, 14, 9.

Berendsen, H.J.C.; Postma, J.P.M.; van Gunsteren, W.F.; DiNola, A.; Haak, J.R. Molecular dynamics with coupling to an external bath The Journal of Chemical Physics **1984**, 81, 3684-3690.

Berneche, S.; Roux, B. Molecular Dynamics of the KcsA K+ Channel in a Bilayer Membrane Biophysical Journal **2000**, 78, 2900-2917.

Berneche, S.; Roux, B. Energetics of ion conduction through the K+ channel Nature **2001**, 414, 73-77.

Berneche, S.; Roux, B. The Ionization State and the Conformation of Glu-71 in the KcsA K+ Channel Biophysical Journal **2002**, 82, 772-780.

Berneche, S.; Roux, B. A microscopic view of ion conduction through the K+ channel Proceedings of the National Academy of Sciences **2003**, 100, 8644-8648.

Bhakdi, S.; Tranum-Jensen, J. Alpha-toxin of Staphylococcus aureus Microbiol. Mol. Biol. Rev. **1991**, 55, 733-751.

Boda, D.; Nonner, W.; Valisko, M.; Henderson, D.; Eisenberg, B.; Gillespie, D. Steric Selectivity in Na Channels Arising from Protein Polarization and Mobile Side Chains Biophysical Journal **2007**, 93, 1960-1980.

Bostick, D.L.; Brooks, C.L., III Selectivity in K+ channels is due to topological control of the permeant ion's coordinated state Proceedings of the National Academy of Sciences **2007**, 104, 9260-9265.

Braha, O.; Gu, L.-Q.; Zhou, L.; Lu, X.; Cheley, S.; Bayley, H. Simultaneous stochastic sensing of divalent metal ions Nature Biotechnology **2000**, 18, 1005-1007.

Brelidze, T.I.; Magleby, K.L. Probing the Geometry of the Inner Vestibule of BK Channels with Sugars The Journal of General Physiology **2005**, 126, 105-121.

Brelidze, T.I.; Niu, X.; Magleby, K.L. A ring of eight conserved negatively charged amino acids doubles the conductance of BK channels and prevents inward rectification Proceedings of the National Academy of Sciences **2003**, 100, 9017-9022.

Cardenas, A.E.; Coalson, R.D.; Kurnikova, M.G. Three-Dimensional Poisson-Nernst-Planck Theory Studies: Influence of Membrane Electrostatics on Gramicidin A Channel Conductance Biophysical Journal **2000**, 79, 80-93.

Carmeliet, E. Voltage- and time-dependent block of the delayed K+ current in cardiac myocytes by dofetilide J Pharmacol Exp Ther **1992**, 262, 809-17.

Case, D.A.; Darden, T.A.; Cheatham, T.E.; Simmerling, C.L.; Wang, J.; Duke, R.E.; Luo, R.; Merz, K.M.; Wang, B.; Pearlman, D.A.;

Crowley, M.; Brozell, S.; Tsui, V.; Gohlke, H.; Mongan, J.; Hornak, V.; Cui, G.; Beroza, P.; Shafmeister, C.; Caldwell, J.W.; Ross, W.S.; Kolmann, P.A., *AMBER 8*. 2004, University of California: San Francisco.

Chandler, D. *Introduction to modern statistical mechanics*; Oxford University Press: New York, 1987.

Chatelain, F.C.; Alagem, N.; Xu, Q.; Pancaroglu, R.; Reuveny, E.; Minor, Jr. The Pore Helix Dipole Has a Minor Role in Inward Rectifier Channel Function Neuron **2005**, 47, 833-843.

Chen, J.; Seebohm, G.; Sanguinetti, M.C. Position of aromatic residues in the S6 domain, not inactivation, dictates cisapride sensitivity of HERG and eag potassium channels Proc Natl Acad Sci U S A **2002**, 99, 12461-6.

Chen, M.F.; Chen, T.Y. Side-chain Charge Effects and Conductance Determinants in the Pore of ClC-0 Chloride Channels The Journal of General Physiology **2003**, 122, 133-145.

Chipot, C.; Pohorille, A. *Free energy calculations : theory and applications in chemistry and biology*; Springer: Berlin ; New York, 2007.

Chung, S.H.; Allen, T.W.; Kuyucak, S. Conducting-State Properties of the KcsA Potassium Channel from Molecular and Brownian Dynamics Simulations Biophysical Journal **2002a**, 82, 628-645.

Chung, S.H.; Kuyucak, S. Ion channels: recent progress and prospects European Biophysics Journal **2002b**, 31, 283-293.

Compoint, M.; Carloni, P.; Ramseyer, C.; Girardet, C. Molecular dynamics study of the KcsA channel at 2.0-A resolution: stability and concerted motions within the pore Biochimica et Biophysica Acta (BBA) - Biomembranes **2004**, 1661, 26-39.

Cordero-Morales, J.F.; Cuello, L.G.; Zhao, Y.; Jogini, V.; Cortes, D.M.; Roux, B.; Perozo, E. Molecular determinants of gating at the potassium-channel selectivity filter Nat Struct Mol Biol **2006**, 13, 311-318.

Cordero-Morales, J.F.; Jogini, V.; Lewis, A.; Vasquez, V.; Cortes, D.M.; Roux, B.; Perozo, E. Molecular driving forces determining potassium channel slow inactivation Nat Struct Mol Biol **2007**, 14, 1062-1069.

Corry, B.; Kuyucak, S.; Chung, S.H. Test of Poisson-Nernst-Planck Theory in Ion Channels The Journal of General Physiology **1999**, 114, 597-600.

Corry, B.; Kuyucak, S.; Chung, S.H. Tests of Continuum Theories as Models of Ion Channels. II. Poisson-Nernst-Planck Theory versus Brownian Dynamics Biophysical Journal **2000**, 78, 2364-2381.

Corry, B.; Kuyucak, S.; Chung, S.H. Dielectric Self-Energy in Poisson-Boltzmann and Poisson-Nernst-Planck Models of Ion Channels Biophysical Journal **2003**, 84, 3594-3606.

Czajkowsky, D.M.; Sheng, S.; Shao, Z. Staphylococcal α-hemolysin can form hexamers in phospholipid bilayers Journal of Molecular Biology **1998**, 276, 325-330.

Daura, X.; Gademann, K.; Jaun, B.; Seebach, D.; van Gunsteren, W.F.; Mark, A.E. Peptide folding: When simulation meets experiment. Angewandte Chemie International Edition **1999**, 38, 236-240.

de Groot, B.L.; Grubmuller, H. The dynamics and energetics of water permeation and proton exclusion in aquaporins Current Opinion in Structural Biology **2005**, 15, 176-183.

de Groot, B.L.; Tieleman, D.P.; Pohl, P.; Grubmuller, H. Water Permeation through Gramicidin A: Desformylation and the Double Helix: A Molecular Dynamics Study Biophys. J. **2002**, 82, 2934-2942.

Decher, N.; Pirard, B.; Bundis, F.; Peukert, S.; Baringhaus, K.H.; Busch, A.E.; Steinmeyer, K.; Sanguinetti, M.C. Molecular basis for Kv1.5 channel block: conservation of drug binding sites among voltage-gated K+ channels J Biol Chem **2004**, 279, 394-400.

del Camino, D.; Holmgren, M.; Liu, Y.; Yellen, G. Blocker protection in the pore of a voltage-gated K+ channel and its structural implications Nature **2000**, 403, 321-5.

Domene, C.; Grottesi, A.; Sansom, M.S.P. Filter Flexibility and Distortion in a Bacterial Inward Rectifier K+ Channel: Simulation Studies of KirBac1.1 Biophysical Journal **2004**, 87, 256-267.

Domene, C.; Sansom, M.S.P. Potassium Channel, Ions, and Water: Simulation Studies Based on the High Resolution X-Ray Structure of KcsA Biophysical Journal **2003**, 85, 2787-2800.

Doyle, D.A.; Cabral, J.; Pfuetzner, R.A.; Kuo, A.; Gulbis, J.M.; Cohen, S.L.; Chait, B.T.; MacKinnon, R. The Structure of the Potassium Channel: Molecular Basis of K+ Conduction and Selectivity Science **1998**, 280, 69-77.

Essmann, U.; Perera, L.; Berkowitz, M.L.; Darden, T.; Lee, H.; Pedersen, L.G. A smooth particle mesh Ewald method The Journal of Chemical Physics **1995**, 103, 8577-8593.

Feller, S.E.; Zhang, Y.; Pastor, R.W.; Brooks, B.R. Constant pressure molecular dynamics simulation: The Langevin piston method The Journal of Chemical Physics **1995**, 103, 4613-4621.

Fernandez, D.; Ghanta, A.; Kauffman, G.W.; Sanguinetti, M.C. Physicochemical features of the HERG channel drug binding site J Biol Chem **2004**, 279, 10120-7.

Ferreras, M.; Höper, F.; Dalla Serra, M.; Colin, D.A.; Prévost, G.; Menestrina, G. The interaction of Staphylococcus aureus bi-component gamma-hemolysins and leucocidins with cells and lipid membranes. Biochim Biophys Acta **1998**, 18.

Ficker, E.; Jarolimek, W.; Brown, A.M. Molecular determinants of inactivation and dofetilide block in ether a-go-go (EAG) channels and EAG-related K(+) channels Mol Pharmacol **2001**, 60, 1343-8.

Ficker, E.; Jarolimek, W.; Kiehn, J.; Baumann, A.; Brown, A.M. Molecular determinants of dofetilide block of HERG K+ channels Circ Res **1998**, 82, 386-95.

Ficker, E.; Obejero-Paz, C.A.; Zhao, S.; Brown, A.M. The binding site for channel blockers that rescue misprocessed human long QT syndrome type 2 ether-a-gogo-related gene (HERG) mutations J Biol Chem **2002**, 277, 4989-98.

Friedlander, M.; Mueckler, M. *Molecular Biology of Receptors and Transporters: Pumps, Transporters and Channels*; Academic Press, 1993; Vol. 137C.

Fujiwara, Y.; Kubo, Y. Functional Roles of Charged Amino Acid Residues on the Wall of the Cytoplasmic Pore of Kir2.1 The Journal of General Physiology **2006**, 127, 401-419.

Furini, S.; Zerbetto, F.; Cavalcanti, S. Application of the Poisson-Nernst-Planck Theory with Space-Dependent Diffusion Coefficients to KcsA Biophysical Journal **2006**, 91, 3162-3169.

Garcia, A.E., *Molecular Dynamics Simulations of Protein Folding*, in *Protein Structure Prediction, Second Edition*, M. Zaki and C. Bystroff, Editors. 2007, Humana Press: Totowa,NJ, USA. p. 315-330.

Garcia-Ferreiro, R.E.; Kerschensteiner, D.; Major, F.; Monje, F.; Stuhmer, W.; Pardo, L.A. Mechanism of block of hEag1 K+ channels by imipramine and astemizole J Gen Physiol **2004**, 124, 301-17.

Garofoli, S.; Jordan, P.C. Modeling Permeation Energetics in the KcsA Potassium Channel Biophysical Journal **2003**, 84, 2814-2830.

Garret, M.; Goodsell, D.; Halliday, R.; Huey, R.; Hart, W.; Belew, R.; Olson, A. Automated docking using a Lamarckian genetic algorithm and an empirical binding free energy function Journal of Computational Chemistry **1998**, 19, 1639-62.

Gavrilova-Ruch, O.; Schonherr, K.; Gessner, G.; Schonherr, R.; Klapperstuck, T.; Wohlrab, W.; Heinemann, S.H. Effects of imipramine on ion channels and proliferation of IGR1 melanoma cells J Membr Biol **2002**, 188, 137-49.

Ginalski, K. Comparative modeling for protein structure prediction Current Opinion in Structural Biology **2006**, 16, 172-177.

Glynn, I.M., *The Na+-K+ transporting adenosine triphosphatase*, in *The Enzymes of biological membranes*, A.N. Martonosi, Editor. 1985, Plenum Press: New York.

Grabe, M.; Bichet, D.; Qian, X.; Jan, Y.N.; Jan, L.Y. K+ channel selectivity depends on kinetic as well as thermodynamic factors Proceedings of the National Academy of Sciences **2006**, 103, 14361-14366.

Graf, P.; Kurnikova, M.G.; Coalson, R.D.; Nitzan, A. Comparison of dynamic lattice Monte Carlo simulations and the dielectric self-energy Poisson-Nernst-Planck continuum theory for model ion channel Journal of Physical Chemistry B **2004**, 108, 2006-2015.

Gu, L.-Q.; Braha, O.; Conlan, S.; Cheley, S.; Bayley, H. Stochastic sensing of organic analytes by a pore-forming protein containing a molecular adapter Nature **1999**, 398, 686-690.

Gu, L.-Q.; Cheley, S.; Bayley, H. Prolonged Residence Time of a Noncovalent Molecular Adapter, β-Cyclodextrin, within the Lumen of Mutant α-Hemolysin Pores Journal of General Physiology **2001**, 118, 481-494.

Gu, L.-Q.; Dalla Serra, M.; Vincent, J.B.; Vigh, G.; Cheley, S.; Braha, O.; Bayley, H. Reversal of charge selectivity in transmembrane protein pores by using noncovalent molecular adapters Proceedings of the National Academy of Sciences **2000**, 97, 3959-3964.

Guex, N.; Peitsch, M.C. SWISS-MODEL and the Swiss-PdbViewer: An environment for comparative protein modeling. Electrophoresis **1997**, 18, 2714-2723.

Hamill, O.P.; Marty, A.; Neher, E.; Sakmann, B.; Sigworth, F.J. Improved patch-clamp techniques for high-resolution current recording from cells and cell-free membrane patches. Pflugers Archiv. **1981**, 391, 85-100.

Hermans, J.; Berendsen, H.J.C.; van Gunsteren, W.F.; Postma, J.P.M. A Consistent Empirical Potential for Water-Protein Interactions Biopolymers **1994**, 23, 1513-1518.

Herzberg, I.M.; Trudeau, M.C.; Robertson, G.A. Transfer of rapid inactivation and sensitivity to the class III antiarrhythmic drug E-4031 from HERG to M-eag channels J Physiol **1998**, 511 (Pt 1), 3-14.

Hess, B.; Bekker, H.; Berendsen, H.J.C.; Fraaije, J.G.E.M. LINCS: A linear constraint solver for molecular simulations Journal of Computational Chemistry **1997**, 18, 1463-1472.

Hetenyi, C.; van der Spoel, D. Efficient docking of peptides to proteins without prior knowledge of the binding site Protein Sci **2002**, 11, 1729-37.

Heymann, J.B.; Engel, A. Aquaporins: Phylogeny, Structure, and Physiology of Water Channels News Physiol Sci **1999**, 14, 187-193.

Hille, B. *Ionic channels of excitable membranes*; Sinauer Associates: Sunderland, MA, 2001.

Hockney, R.W. The potentail calculations and some applications Methods in Computational Physics **1970**, 9, 136-211.

Hodgkin, A.; Huxley, A. A quantitative description of ion currents and its applications to conduction and excitation in nerve membranes J.Physiol.(Lond.) **1952**, 117, 500-544.

Howorka, S.; Cheley, S.; Bayley, H. Sequence-specific detection of individual DNA strands using engineered nanopores Nature Biotechnology **2001**, 19, 636-639.

Humphrey, W.; Dalke, A.; Schulten, K. VMD: visual molecular dynamics Journal of Molecular Graphics **1996**, 14, 33-38.

Hunter, C.A.; Singh, J.; Thornton, J.M. Pi-pi interactions: the geometry and energetics of phenylalanine-phenylalanine interactions in proteins J Mol Biol **1991**, 218, 837-46.

Imoto, K.; Busch, C.; Sakmann, B.; Mishina, M.; Konno, T.; Nakai, J.; Bujo, H.; Mori, Y.; Fukuda, K.; Numa, S. Rings of negatively charged amino acids determine the acetylcholine receptor channel conductance Nature **1988**, 335, 645-648.

Jiang, Y.; Lee, A.; Chen, J.; Cadene, M.; Chait, B.T.; MacKinnon, R. Crystal structure and mechanism of a calcium-gated potassium channel Nature **2002a**, 417, 515-522.

Jiang, Y.; Lee, A.; Chen, J.; Cadene, M.; Chait, B.T.; MacKinnon, R. The open pore conformation of potassium channels Nature **2002b**, 417, 523-526.

Jiang, Y.; Lee, A.; Chen, J.; Ruta, V.; Cadene, M.; Chait, B.T.; MacKinnon, R. X-ray structure of a voltage-dependent K+ channel Nature **2003**, 423, 33-41.

Jogini, V.; Roux, B. Electrostatics of the Intracellular Vestibule of K+ Channels Journal of Molecular Biology **2005**, 354, 272-288.

Jorgensen, W.L.; Chandrasekhar, J.; Madura, J.D.; Impey, R.W.; Klein, M.L. Comparison of simple potential functions for simulating liquid water The Journal of Chemical Physics **1983**, 79, 926-935.

Kale, L.; Skeel, R.; Bhandarkar, M.; Brunner, R.; Gursoy, A.; Krawetz, N.; Phillips, J.; Shinozaki, A.; Varadarajan, K.; Schulten, K. NAMD2 :

Greater scalability for parallel molecular dynamics Journal of Computational Physics **1999**, 151, 283-312.

Kamiya, K.; Mitcheson, J.S.; Yasui, K.; Kodama, I.; Sanguinetti, M.C. Open channel block of HERG K(+) channels by vesnarinone Mol Pharmacol **2001**, 60, 244-53.

Kang, X.f.; Cheley, S.; Rice-Ficht, A.C.; Bayley, H. A Storable Encapsulated Bilayer Chip Containing a Single Protein Nanopore Journal of the American Chemical Society **2007**, 129, 4701-4705.

Kasianowicz, J.J.; Brandin, E.; Branton, D.; Deamer, D.W. Characterization of individual polynucleotide molecules using a membrane channel Proceedings of the National Academy of Sciences **1996**, 93, 13770-13773.

Korchev, Y.E.; Bashford, C.L.; Alder, G.M.; Kasianowicz, J.J.; Pasternak, C.A. Low conductance states of a single ion channel are not 'closed' The Journal of Membrane Biology **1995**, 147, 233-9.

Kumar, S.; Rosenberg, J.M.; Bouzida, D.; Swendsen, R.H.; Kollman, P.A. THE weighted histogram analysis method for free-energy calculations on biomolecules. I. The method Journal of Computational Chemistry **1992**, 13, 1011-1021.

Kuntz, I.D.; Blaney, J.M.; Oatley, S.J.; Langridge, R.; Ferrin, T.E. A geometric approach to macromolecule-ligand interactions Journal of Molecular Biology **1982**, 161, 269-288.

Kuo, A.; Gulbis, J.M.; Antcliff, J.F.; Rahman, T.; Lowe, E.D.; Zimmer, J.; Cuthbertson, J.; Ashcroft, F.M.; Ezaki, T.; Doyle, D.A. Crystal Structure of the Potassium Channel KirBac1.1 in the Closed State Science **2003**, 300, 1922-1926.

Kurnikova, M.G.; Coalson, R.D.; Graf, P.; Nitzan, A. A Lattice Relaxation Algorithm for Three-Dimensional Poisson-Nernst-Planck Theory with Application to Ion Transport through the Gramicidin A Channel Biophysical Journal **1999**, 76, 642-656.

Latorre, R.; Oberhauser, A.; Labarca, P.; Alvarez, O. Varieties of Calcium-Activated Potassium Channels Annual Review of Physiology **1989**, 51, 385-399.

Leach, A.R. Ligand docking to proteins with discrete side-chain flexibility Journal of Molecular Biology **1994**, 235, 345-356.

Leach, A.R.; Shoichet, B.K.; Peishoff, C.E. Prediction of Protein-Ligand Interactions. Docking and Scoring: Successes and Gaps J. Med. Chem. **2006**, 49, 5851-5855.

Lees-Miller, J.P.; Duan, Y.; Teng, G.Q.; Duff, H.J. Molecular determinant of high-affinity dofetilide binding to HERG1 expressed in Xenopus oocytes: involvement of S6 sites Mol Pharmacol **2000**, 57, 367-74.

LeMasurier, M.; Heginbotham, L.; Miller, C. KcsA: It's a Potassium Channel The Journal of General Physiology **2001**, 118, 303-314.

Li, R.A.; Velez, P.; Chiamvimonvat, N.; Tomaselli, G.F.; Marban, E. Charged Residues between the Selectivity Filter and S6 Segments Contribute to the Permeation Phenotype of the Sodium Channel The Journal of General Physiology **1999**, 115, 81-92.

Lide, D.R. *CRC handbook of chemistry and physics, 2004*; CRC Press: Boca Raton, 2004.

Long, S.B.; Campbell, E.B.; Mackinnon, R. Crystal structure of a mammalian voltage-dependent Shaker family K+ channel Science **2005**, 309, 897-903.

Ludwig, J.; Terlau, H.; Wunder, F.; Bruggemann, A.; Pardo, L.A.; Marquardt, A.; Stuhmer, W.; Pongs, O. Functional expression of a rat homologue of the voltage gated either a go-go potassium channel reveals differences in selectivity and activation kinetics between the Drosophila channel and its mammalian counterpart Embo J **1994**, 13, 4451-8.

MacKerell, A.D.; Bashford, D.; Bellott, M.; Dunbrack, R.L.; Evanseck, J.D.; Field, M.J.; Fischer, S.; Gao, J.; Guo, H.; Ha, S.; Joseph-McCarthy, D.; Kuchnir, L.; Kuczera, K.; Lau, F.T.K.; Mattos, C.; Michnick, S.; Ngo, T.; Nguyen, D.T.; Prodhom, B.; Reiher, W.E.; Roux, B.; Schlenkrich, M.; Smith, J.C.; Stote, R.; Straub, J.; Watanabe, M.; Wiorkiewicz-Kuczera, J.; Yin, D.; Karplus, M. All-Atom Empirical Potential for Molecular Modeling and Dynamics Studies of Proteins Journal of Physical Chemistry B **1998**, 102, 3586-3616.

MacKinnon, R.; Cohen, S.L.; Kuo, A.; Lee, A.; Chait, B.T. Structural Conservation in Prokaryotic and Eukaryotic Potassium Channels Science **1998**, 280, 106-109.

Mafe, S.; Pellicer, J.; Cervera, J. Kinetic modeling of ion conduction in KcsA potassium channel The Journal of Chemical Physics **2005**, 122, 204712-8.

Mamonov, A.B.; Kurnikova, M.G.; Coalson, R.D. Diffusion constant of K+ inside Gramicidin A: A comparative study of four computational methods Biophysical Chemistry **2006**, 124, 268-278.

Martyna, G.J.; Tobias, D.J.; Klein, M.L. Constant pressure molecular dynamics algorithms The Journal of Chemical Physics **1994**, 101, 4177-4189.

McGaughey, G.B.; Gagne, M.; Rappe, A.K. pi-Stacking interactions. Alive and well in proteins J Biol Chem **1998**, 273, 15458-63.

McGeoch, J.E.; McGeoch, M.W.; Carter, D.J.; Shuman, R.F.; Guidotti, G. Biological-to-electronic interface with pores of ATP synthase subunit

C in silicon nitride barrier Medical and Biological Engineering and Computing **2000**, 38, 11-119.

Menestrina, G. Ionic channel formed by staphylococcus aureus alpha-toxin: voltage dependent inhibition by divalent and trivalent cations Journal of Membrane Biology **1986**, 90, 170-190.

Meunier, O.; Ferreras, M.; Supersac, G.; Hoeper, F.; Baba-Moussa, L.; Monteil, H.; Colin, D.A.; Menestrina, G.; Prevost, G. A predicted [beta]-sheet from class S components of staphylococcal [gamma]-hemolysin is essential for the secondary interaction of the class F component Biochimica et Biophysica Acta (BBA) - Biomembranes **1997**, 1326, 275-286.

Mills, J.E.J.; Dean, P.M. Three-dimensional hydrogen-bond geometry and probability information from a crystal survey Journal of Computer-Aided Molecular Design **1996**, 10, 607-622.

Misakian, M.; Kasianowicz, J.J. Electrostatic Influence on Ion Transport through the aHL Channel Journal of Membrane Biology **2003**, 195, 137-146.

Mitcheson, J.S.; Chen, J.; Lin, M.; Culberson, C.; Sanguinetti, M.C. A structural basis for drug-induced long QT syndrome Proceedings of the National Academy of Sciences **2000a**, 97, 12329-12333.

Mitcheson, J.S.; Chen, J.; Sanguinetti, M.C. Trapping of a methanesulfonanilide by closure of the HERG potassium channel activation gate J Gen Physiol **2000b**, 115, 229-40.

Morais-Cabral, J.H.; Zhou, Y.; MacKinnon, R. Energetic optimization of ion conduction rate by the K+ selectivity filter Nature **2001**, 414, 37-42.

Morera, F.J.; Vargas, G.; González, C.; Rosenmann, E.; Latorre, R., *Ion-channel reconstitution*, in *Methods in Molecular Biology*, A. Dopico, Editor. 2007, Humana Press: Totowa. p. 571-586.

Morris, G.M.; Goodsell, D.S.; Halliday, R.S.; Huey, R.; Hart, W.E.; Belew, R.K.; Olson, A.J. Automated Docking using a Lamarckian genetic algorithm and an empirical binding free energy function Journal of Computational Chemistry **1998**, 19, 1639-1662.

Mueller, P.; Rudin, D.O.; Tien, H.T.; Wescott, W.C. Reconstitution of cell membrane structure in vitro and its transformation into an excitable system Nature **1962**, 194, 979-980.

Murzin, A.G.; Lesk, A.M.; Chothia, C. Principles determining the structure of β-sheet barrels in proteins I. A theoretical analysis Journal of Molecular Biology **1994a**, 236, 1369-1381.

Murzin, A.G.; Lesk, A.M.; Chothia, C. Principles determining the structure of β-sheet barrels in proteins II. The observed structures Journal of Molecular Biology **1994b**, 236, 1382-1400.

Nimigean, C.M.; Chappie, J.S.; Miller, C. Electrostatic Tuning of Ion Conductance in Potassium Channels Biochemistry **2003**, 42, 9263-9268.

Nina, M.; Beglov, D.; Roux, B. Atomic Radii for Continuum Electrostatics Calculations Based on Molecular Dynamics Free Energy Simulations Journal of Physical Chemistry B **1997**, 101, 5239-5248.

Nonner, W.; Chen, D.P.; Eisenberg, B. Progress and Prospects in Permeation The Journal of General Physiology **1999**, 113, 773-782.

Noskov, S.Y.; Berneche, S.; Roux, B. Control of ion selectivity in potassium channels by electrostatic and dynamic properties of carbonyl ligands Nature **2004a**, 431, 830-834.

Noskov, S.Y.; Im, W.; Roux, B. Ion Permeation through the alpha-Hemolysin Channel: Theoretical Studies Based on Brownian Dynamics and Poisson-Nernst-Plank Electrodiffusion Theory Biophysical Journal **2004b**, 87, 2299-2309.

Notredame, C.; Higgins, D.; Heringa, J. T-Coffee: A novel method for multiple sequence alignments Journal of Molecular Biology **2000**, 302, 205-217.

Ouadid-Ahidouch, H.; Le Bourhis, X.; Roudbaraki, M.; Toillon, R.A.; Delcourt, P.; Prevarskaya, N. Changes in the K+ current-density of MCF-7 cells during progression through the cell cycle: possible involvement of a h-ether.a-gogo K+ channel Receptors Channels **2001**, 7, 345-56.

Paine, P.L.; Scherr, P. Drag coefficients for the movement of rigid spheres through liquid-filled cylindrical pores Biophys. J. **1975**, 15, 1087-1091.

Pardo, L.A.; del Camino, D.; Sanchez, A.; Alves, F.; Bruggemann, A.; Beckh, S.; Stuhmer, W. Oncogenic potential of EAG K(+) channels EMBO Journal **1999**, 18, 5540-5547.

Perozo, E.; Marien, D.; Cortes; Cuello, L.G. Structural Rearrangements Underlying K+-Channel Activation Gating Science **1999**, 285, 73-78.

Pettersen, E.F.; Goddard, T.D.; Huang, C.C.; Couch, G.S.; Greenblatt, D.M.; Meng, E.C.; Ferrin, T.E. UCSF Chimera - A Visualization System for Exploratory Research and Analysis Journal of Computational Chemistry **2004**, 25, 1605-1612.

Ranatunga, K.M.; Shrivastava, I.H.; Smith, G.R.; Sansom, M.S.P. Side-Chain Ionization States in a Potassium Channel Biophys. J. **2001**, 80, 1210-1219.

Rocchia, W.; Sridharan, S.; Nicholls, A.; Alexov, E.; Chiabrera, A.; Honig, B. Rapid grid-based construction of the molecular surface and the use of induced surface charge to calculate reaction field energies:

Applications to the molecular systems and geometric objects Journal of Computational Chemistry **2002**, 23, 128-137.

Romano, T.K. Structure-Based Drug Design: Docking and Scoring Current Protein and Peptide Science **2007**, 8, 312-328.

Roux, B.; MacKinnon, R. The cavity and pore helices in the KcsA K+ channel: stabilization of monovalent cations Science **1999**, 285, 59-61.

Ryckaert, J.P.; Ciccotti, G.; Berendsen, H.J.C. Numerical integration of the cartesian equations of motion of a system with constraints: Molecular dynamics of n-alkanes Journal of Computational Physics **1977**, 23, 327-341.

Sackmann, E.; Tanaka, M. Supported membranes on soft polymer cushions: fabrication, characterization and applications Trends in Biotechnology **2000**, 18, 58-64.

Sakmann, B.; Neher, E. *Single channel recording*; Springer, 1995.

Sanchez-Chapula, J.A.; Navarro-Polanco, R.A.; Culberson, C.; Chen, J.; Sanguinetti, M.C. Molecular determinants of voltage-dependent human ether-a-go-go related gene (HERG) K+ channel block J Biol Chem **2002**, 277, 23587-95.

Sanguinetti, M.C.; Jiang, C.; Curran, M.E.; Keating, M.T. A mechanistic link between an inherited and an acquired cardiac arrhythmia: HERG encodes the IKr potassium channel Cell **1995**, 81, 299-307.

Saparov, S.M.; Pohl, P. Beyond the diffusion limit: Water flow through the empty bacterial potassium channel Proceedings of the National Academy of Sciences **2004**, 101, 4805-4809.

Schwede, T.; Kopp, J.; Guex, N.; Peitsch, M.C. SWISS-MODEL: An automated protein homology-modeling server Nucleic Acids Res **2003**, 31, 3381-5.

Shatsky, M.; Nussinov, R.; Wolfson, H.J., *Algorithms for Multiple Protein Structure Alignment and Structure-Derived Multiple Sequence Alignment*, in *Structure Prediction, Second Edition*, M. Zaki and C. Bystroff, Editors. 2007, Humana Press: Totowa,NJ, USA. p. 125-146.

Shaw, R.S.; Packard, N.; Schroter, M.; Swinney, H.L. Geometry-induced asymmetric diffusion Proceedings of the National Academy of Sciences **2007**, 104, 9580-9584.

Shealy, R.T.; Murphy, A.D.; Ramarathnam, R.; Jakobsson, E.; Subramaniam, S. Sequence-Function Analysis of the K+-Selective Family of Ion Channels Using a Comprehensive Alignment and the KcsA Channel Structure Biophysical Journal **2003**, 84, 2929-2942.

Shrivastava, I.H.; Sansom, M.S.P. Simulations of Ion Permeation Through a Potassium Channel: Molecular Dynamics of KcsA in a Phospholipid Bilayer Biophysical Journal **2000**, 78, 557-570.

Smart, O.S.; Coates, G.M.P.; Sansom, M.S.P.; Alder, G.M.; Bashford, L.C. Structure-based prediction of the conductance properties of ion channels Faraday Discussion **1998**, 111, 185-99.

Smith, S.S.; Liu, X.; Zhang, Z.R.; Sun, F.; Kriewall, T.E.; McCarty, N.A.; Dawson, D.C. CFTR: Covalent and Noncovalent Modification Suggests a Role for Fixed Charges in Anion Conduction The Journal of General Physiology **2001**, 118, 407-432.

Snyders, D.J.; Chaudhary, A. High affinity open channel block by dofetilide of HERG expressed in a human cell line Mol Pharmacol **1996**, 49, 949-55.

Song, L.; Hobaugh, M.R.; Shustak, C.; Cheley, S.; Bayley, H.; Gouaux, J.E. Structure of Staphylococcal α-Hemolysin, a Heptameric Transmembrane Pore Science **1996**, 274, 1859-1866.

Stuhmer, W. Electrophysiological recording from Xenopus oocytes Methods Enzymology **1992**, 207, 319-339.

Suessbrich, H.; Waldegger, S.; Lang, F.; Busch, A.E. Blockade of HERG channels expressed in Xenopus oocytes by the histamine receptor antagonists terfenadine and astemizole FEBS Lett **1996**, 385, 77-80.

Teschemacher, A.G.; Seward, E.P.; Hancox, J.C.; Witchel, H.J. Inhibition of the current of heterologously expressed HERG potassium channels by imipramine and amitriptyline Br J Pharmacol **1999**, 128, 479-85.

Torrie, G.M.; Valleau, J.P. Monte Carlo free energy estimates using non-Boltzmann sampling: Application to the sub-critical Lennard-Jones fluid Chemical Physics Letters **1974**, 28, 578-581.

Valeva, A.; Palmer, M.; Bhakdi, S. Staphylococcal α-Toxin: Formation of the Heptameric Pore Is Partially Cooperative and Proceeds through Multiple Intermediate Stages Biochemistry **1997**, 36, 13298-13304.

Van der Spoel, D.; Lindahl, E.; Hess, B.; Groenhof, G.; Mark, A.E.; Berendsen, H.J.C. GROMACS: Fast, flexible, and free Journal of Computational Chemistry **2005**, 26, 1701-1718.

van Gunsteren, W.F.; Kruger, P.; Billeter, S.R.; Mark, A.E.; Eising, A.A.; Scott, W.R.P.; Huneberger, P.H.; Tiron, I.G. *Biomolecular Simulation: The GROMOS96 Manual and User Guide.*; Biomos & Hochschulverlag AG an der ETH Zurich: Groningen and Zurich., 1996.

Verlet, L. Computer "Experiments" on Classical Fluids. I. Thermodynamical Properties of Lennard-Jones Molecules Physical Review **1967**, 159, 98.

Volkov, A.G.; Paula, S.; Deamer, D.W. Two mechanisms of permeation of small neutral molecules and hydrated ions across phospholipid bilayers Bioelectrochemistry and Bioenergetics **1997**, 42, 153-160.

Vorst, H.A.v.d. BI-CGSTAB: a fast and smoothly converging variant of BI-CG for the solution of nonsymmetric linear systems SIAM J. Sci. Stat. Comput. **1992**, 13, 631-644.

Wang, S.; Morales, M.J.; Liu, S.; Strauss, H.C.; Rasmusson, R.L. Modulation of HERG affinity for E-4031 by [K+]o and C-type inactivation FEBS Lett **1997**, 417, 43-7.

White, S. *http://blanco.biomol.uci.edu/Membrane_Proteins_xtal.html*.

Witchel, H.J.; Dempsey, C.E.; Sessions, R.B.; Perry, M.; Milnes, J.T.; Hancox, J.C.; Mitcheson, J.S. The low-potency, voltage-dependent HERG blocker propafenone--molecular determinants and drug trapping Mol Pharmacol **2004**, 66, 1201-12.

Wu, X.; Brooks, B.R. {beta}-Hairpin Folding Mechanism of a Nine-Residue Peptide Revealed from Molecular Dynamics Simulations in Explicit Water Biophys. J. **2004**, 86, 1946-1958.

Xu, L.; Wang, Y.; Gillespie, D.; Meissner, G. Two Rings of Negative Charges in the Cytosolic Vestibule of Type-1 Ryanodine Receptor Modulate Ion Fluxes Biophysical Journal **2006**, 90, 443-453.

Yang, B.; Verkman, A.S. Water and Glycerol Permeabilities of Aquaporins 1-5 and MIP Determined Quantitatively by Expression of Epitope-tagged Constructs in Xenopus Oocytes J. Biol. Chem. **1997**, 272, 16140-16146.

Young, D.M. *Iterative solution of large linear systems*; Academic press: New York and London, 1971.

Zhou, Y.; MacKinnon, R. The Occupancy of Ions in the K+ Selectivity Filter: Charge Balance and Coupling of Ion Binding to a Protein Conformational Change Underlie High Conduction Rates Journal of Molecular Biology **2003**, 333, 965-975.

Zhou, Y.; Morais-Cabral, J.H.; Kaufman, A.; MacKinnon, R. Chemistry of ion coordination and hydration revealed by a K+ channel-Fab complex at 2.0 A resolution Nature **2001**, 414, 43-48.

Zhou, Z.; Vorperian, V.R.; Gong, Q.; Zhang, S.; January, C.T. Block of HERG potassium channels by the antihistamine astemizole and its metabolites desmethylastemizole and norastemizole J Cardiovasc Electrophysiol **1999**, 10, 836-43.

Zhu, F.; Tajkhorshid, E.; Schulten, K. Pressure-Induced Water Transport in Membrane Channels Studied by Molecular Dynamics Biophys. J. **2002**, 83, 154-160.
Zhu, F.; Tajkhorshid, E.; Schulten, K. Theory and Simulation of Water Permeation in Aquaporin-1 Biophys. J. **2004**, 86, 50-57.